Optical Characterization of Defect levels in AlGaN-based Light Emitting Materials

(AlGaN 系発光材料の欠陥準位の光学的評価)

A dissertation submitted to the Graduate School of Science and Engineering of the Saitama University in partial fulfillment of the requirements for the degree of Doctor of Philosophy

By

Md. Ismail Hossain

(17DS054)

Written under the supervision of

Professor Norihiko Kamata

Saitama University, Japan

September 2020

This Thesis Is Dedicated

To

My Loving Parents

ABSTRACT

Although the efficiency of AlGaN-based optoelectronic devices has improved in recent years, the realization of high external quantum efficiency (EQE) ultraviolet (UV) light emitting diodes (LEDs) with wavelengths below 360 nm is still challenging. In spite of the development of growth techniques, the lack of native lattice-matched, cost-effective, and suitable substrates produces high densities of threading dislocations and point defects which act as nonradiative recombination (NRR) centers or trap centers in the crystal. The defect mediated NRR centers reduces the carrier lifetime and are responsible for the low efficiency of the devices. To resolve these problems, it is indispensable not only to understand the basic mechanism of grown-in defects and imperfections in these materials, but also to find out the correlations of these defects with the performance and reliability limiting problems and impute them to their physical origin. Thus, the study of NRR centers is likely to remain an important and active research thrust for the realization of high efficiency AlGaN UV light emitting devices.

In this study, different AlGaN-based multiple quantum wells (MQWs) samples have been investigated by photoluminescence (PL) and two-wavelength excited photoluminescence (TWEPL) methods. In the TWEPL, an intermittent below-gap excitation (BGE) light whose photon energy is lower than the bandgap energy of the material ($h\nu_{BGE} < E_g$), is superposed on a constant above-gap excitation (AGE) light ($h\nu_{AGE} > E_g$) at the same point of the sample surface. The intensity change in photoluminescence (PL) due to the addition of a BGE light on an AGE light implies the presence of NRR levels in the energy position corresponding to the photon energy of the BGE source.

The NRR centers in two UV-C (deep UV) AlGaN MQW samples, grown at two different growth temperatures 1140 °C and 1180 °C, on c-plane sapphire substrate by metal-organic chemical vapor deposition (MOCVD) technique, have been studied by TWEPL at about 25 K. The PL intensity decreased by the superposition of BGE light of photon energies between 0.93 eV and 1.46 eV over an AGE light of energy 4.66 eV. This is explained by a two-level recombination model based on Shockley–Read–Hall (SRH) statistics. The model indicates the presence of a pair of NRR centers in both samples,

which are activated by the BGE. The degree of PL quenching for the sample grown at 1140 ^{o}C is higher than that of the sample grown at 1180 ^{o}C for BGE energies 0.93 eV, 1.17 eV, and 1.27 eV. The defect density ratio of 1.5, for the BGE energy of 1.27 eV, was obtained from a qualitative simulation. This result implies that a slight difference in growth conditions changes defect densities.

Superlattice (SL) period (SLP) dependence on NRR centers of UV-B AlGaN MQW samples, grown on c-plane sapphire substrate at 1150^{o}C by MOCVD technique, have been studied by TWEPL. The SLP affects the lattice relaxation of SL and *n*-AlGaN layer. The NRR centers in *n*-AlGaN and QW layers of these samples have been detected by adding BGE light of energies 0.93 eV, 1.17 eV, 1.27 eV, and 1.46 eV over an AGE light of energy 4.66 eV at 30 K. By the superposition of these BGE light on AGE, the PL intensity decreased and the degree of PL quenching from both the layers of the sample with SLP 100 is lower than those of other samples with SLP 50, 150, and 200. By a qualitative simulation with the dominant BGE of photon energy 1.27 eV, the density-ratio of NRR centers in *n*-AlGaN layers of 50:100:150:200 SLP samples is obtained as 1.7:1.0:6.5:3.4. This result implies that the number of SLP changes lattice relaxation and determine density of NRR centers in *n*-AlGaN layer and as a whole in QW layer which affects the performance of LEDs.

NRR processes through defect states and their temperature dependence in UV-B AlGaN MQW sample on sapphire substrate grown by MOCVD technique have been studied by photoluminescence (PL) spectroscopy. We detected NRR centers by adding a below-gap excitation light with photon energies from 0.93 eV to 1.46 eV on an above-gap excitation light of 4.66 eV. All the BGE energies decreased PL intensity at 25 K, and the most-distinct quenching is observed by 1.27 eV BGE at the same BGE photon number density. The temperature-dependent PL intensity for the BGE energy of 1.27 eV is interpreted by three NRR centers. The one-level model dominates over that of two-level model in the temperature range 58 K < T < 88 K. The two-level model prevails in other region of temperature. The combination of one-level and two-level models is consistent with the spectral peak-energy shift as a function of temperature.

ACKNOWLEDGEMENTS

At first, I express my gratefulness to Almighty Allah (the creator of the universe in my belief) for successful completion of the research work.

I would like to express my profound thanks and heartfelt gratitude to my esteemed supervisor Professor Norihiko KAMATA for his scholastic guidance, continuous inspiration, amicable disposition and painstaking help during the course of my research work. His guidance helped me in all the time of research and writing of this thesis. I am very much fortunate and indebted to him for allowing me as a PhD student under his kind supervision.

I would also like to express my sincere gratitude to other committee members; Professor Hiroyuki YAGUCHI, Professor Masamichi SAKAI, and Professor Shuhei YAGI for their valuable suggestions and guidance during my candidature.

I would like to convey my special gratitude to Professor Hideki Hirayama, RIKEN, Wako for providing different samples for the measurement and his valuable discussion during my course study.

I consider myself to be very lucky for getting help from Professor A. Z. M. Touhidul Islam, Dr. Julkernain and Dr. Dulal Haque. I am very much grateful to them for their guidance, fruitful discussion and inspiration during my study. Without their cordial cooperation and kind direction, this work would have been difficult to complete.

I also grateful to all of my esteemed teachers whose inspiration and guidance helped me to travel all the way from the very beginning of my life to reach my present position. I acknowledge their support with great honour.

I would like to convey my special gratitude to all of my teachers and colleagues of the department of Physics, University of Rajshahi, for their valuable suggestions, inspiration and supports during my study. The advice from Professor Emeritus Arun Kumar Basak, Professor M. Alfaz Uddin and Professor A. K. Fazlul Haque is thankfully acknowledged.

I would like to offer my special thanks to all of my lab members and departments administrators, for their support to learn and familiar with the experimental systems as well as technical supports and all the fun we have had in past three years.

Special thank goes to the Ministry of Education, Culture, Sports, Science, and Technology (MEXT) Japan for providing the scholarship.

I consider myself to be fortunate enough having a group of friends, from different countries, who helped me keep calm during times of stress and also helped me take a break from the regular research life.

I also thankfully acknowledge the prayers of many relatives, friends, and well-wishers.

The last but not the least, I am deeply indebted to my beloved parents including all of my family members specially my beloved wife Dr. Naima Sultana Shompa and my only daughter Najifa Yasmin who have sacrificed a lot in the last three years. Their unconditional love, patience, prayers and support over the years have helped me to succeed in my endeavours. They all have made my life more meaningful and joyful.

Md. Ismail Hossain

Saitama University, September 2020

LIST OF PUBLICTIONS

Journal Papers

1. **M. Ismail Hossain,** Yuri Itokazu, Shunsuke Kuwaba, Norihiko Kamata, and Hideki Hirayama, *"Temperature dependence of nonradiative recombination processes in UV-B AlGaN quantum well revealed by below-gap excitation light"*, Optical Materials **105**, 109878 (2020); https://doi.org/10.1016/j.optmat.2020.109878

2. **M. Ismail Hossain**, Yuri Itokazu, Shunsuke Kuwaba, Norihiko Kamata, Noritoshi Maeda, and Hideki Hirayama, "*Superlattice period dependence on nonradiative recombination centers in the n-AlGaN layer of UV-B region revealed by below-gap excitation light*" AIP Advances **10**, 035224 (2020); https://doi.org/10.1063/1.5134698

3. **M. Ismail Hossain**, Yuri Itokazu, Shunsuke Kuwaba, Norihiko Kamata, Noritoshi Maeda, and Hideki Hirayama, "*Nonradiative recombination centers in deep UV-wavelength AlGaN quantum wells detected by below-gap excitation light*", Japanese Journal of Applied Physics **58**, SCCB37 (2019); https://doi.org/10.7567/1347-4065/ab1069

Conference Presentations

1. **M. Ismail Hossain,** Yuri Itokazu, Shunsuke Kuwaba, Norihiko Kamata, Noritoshi Maeda, and Hideki Hirayama, "*Nonradiative Recombination Centers in UVB AlGaN Quantum Well and their Temperature Dependence Revealed by Below-Gap Excitation Light*", The 9th Asia-Pacific Workshop on Widegap Semiconductors (APWS), November 10–15, 2019, Okinawa, Japan.

2. **M. Ismail Hossain,** Yuri Itokazu, Shunsuke Kuwaba, Norihiko Kamata, Noritoshi Maeda, and Hideki Hirayama, "*Nonradiative Recombination Centers in AlGaN Deep UV-LEDs Detected by Below-Gap Excitation Light*", International Workshop on Nitride Semiconductors (IWN), November 11–16, 2018, Kanazawa, Japan.

3. Norihiko Kamata, **M. Ismail Hossain,** Yushi Itokazu, Noritoshi Maeda, and Hideki Hirayama, "*Nonradiative recombination centers in AlGaN MQW for deep UV-LED reveled by below-gap excitation light and its energy dependence",* The 16th International Symposium on the Science and Technology of Lighting (LS16), June 17-22, 2018, Sheffield, UK.

VITA

1983	Born, Rajshahi, Bangladesh
2005	B. Sc. (Honours) in Physics, Faculty of Science, University of Rajshahi, Rajshahi-6205, Bangladesh
2006	M. Sc. (Thesis) in Physics, Faculty of Science, University of Rajshahi, Rajshahi-6205, Bangladesh
2009 - 2010	Lecturer of Physics (Part Time), Agrani School and College, RUET Campus, Rajshahi-6204, Bangladesh
2010 - 2011	Lecturer of Physics, Rajshahi Shikkha Board Govt. Model School and College, Rajshahi-6203, Bangladesh
2011 - 2014	Lecturer, Department of Physics, University of Rajshahi, Rajshahi-6205, Bangladesh
2014 ~Present	Assistant Professor, Department of Physics, University of Rajshahi, Rajshahi-6205, Bangladesh
2017 - 2020	Doctoral Candidate, Graduate School of Science and Engineering, Saitama University, Saitama 338-8570, Japan

CONTENTS

LIST OF TABLES

LIST OF FIGURES

LIST OF ABBREVIATIONS

AGE	Above-Gap Excitation
BGE	Below-Gap Excitation
BSF	Basal-Plane Stacking Fault
DAP	Donor Acceptor Pair
DL	Deep Level
DLOS	Deep Level Optical Spectroscopy
DLTS	Deep Level Transient Spectroscopy
DUV-LED	Deep Ultraviolet Light Emitting Diode
EQE	External Quantum Efficiency
IQE	Internal Quantum Efficiency
LD	Laser Diode
LED	Light Emitting Diode
MOCVD	Metal Organic Chemical Vapor Deposition
MQW	Multiple Quantum Well
NBE	Near Band Edge
Nd:YAG	Neodymium-doped Yttrium Aluminium Garnet
NRR	Nonradiative Recombination
PL	Photoluminescence
PLE	Photoluminescence Excitation
QCSE	Quantum Confined Stark Effect
QW	Quantum Well
SL	Superlattice
SLP	Superlattice Period

SRH	Shockley-Read-Hall
UV-DPSS	Ultraviolet Diode Pump Solid State
VBM	Valence Band Maximum
VRBE	Vacuum Referred Binding Energy

CHAPTER 01

INTRODUCTION

1.1 Motivation

Group-III nitrides such as aluminium nitride (AlN) gallium nitride (GaN), indium nitride (InN), and their alloys are the key materials for efficient optoelectronic devices in ultraviolet (UV), blue and green spectral range [1]. In addition, large bandgap and break-down electric field of AlN and GaN make them an attractive choice for power electronics [2]. The bandgap energies of these materials can be varied from 0.7 eV for InN, 3.4 eV for GaN up to 6.2 eV for AlN by alloying InN or AlN with GaN to suit the desired application in the range of infrared to deep ultraviolet [2,3]. The research story of nitrides began in the late 1960's [4] but became popularities after the development of controlled growth and doping techniques by Akasaki and Amano in the late 1980's [5,6]. In the middle of 1990's, Nakamura et al. [7,8] developed and commercialized InGaN blue light-emitting diode (LED), and the performance of this LED was beyond the expectation irrespective of the number and degree of structural imperfections compared with the other III-V optoelectronic devices [9].

Research into AlGaN-based UV LEDs for wavelengths shorter than 360 nm was initiated by several research groups between 1996 and 1999 [10–13]. The efficiency of these devices has improved in recent years and the highest reported EQE is 14.3% ever for DUV-LED [14]. Recently, the demand of cheap, environmentally friendly and smart AlGaN UV LEDs and LDs with wavelengths below 360 nm has arisen because of its legionary potential applications, such as those in immunotherapy (310 nm), for vulgaris treatment (310 nm), gravitational sensors, plant lighting (310 nm), water sterilization, assisting in the transportation of foods, the manufacture of bank notes, the production of vitamin D3 in the human body (294–304 nm), the detection of biochemical agents, fluorescence detection, and the identification of proteins, DNA, and bacteria [3,10,15–

20]. Research leading to improve the efficiency of AlGaN UV devices is essential especially in the range of 220 nm to 350 nm for the fulfilment of the aforesaid and other applications [10].

Although the efficiency of the AlGaN-based devices has improved in recent years, but the realization of high-EQE UV LEDs with wavelengths below 360nm is still challenging [10]. In spite of the development of growth techniques, the lack of lattice-matched, cost-effective, and suitable substrates produces high densities of threading dislocations and point defects which act as nonradiative recombination (NRR) centers or trap centers in the crystal [3,21–25]. One of the main concerns for crystal growers is to minimize such below-gap states which act as NRR centers. To improve the internal quantum efficiency (IQE) and overall EQE of light emitting materials, it is indispensable to reduce the densities of NRR centers. Besides, it is essential an in-depth understanding of the basic mechanism of grown-in defects and imperfections in these materials for the improvement in efficiency and the reliability of AlGaN UV light emitting devices by mitigating the NRR centers. Such advancement requires a way to identify NRR levels in AlGaN materials conclusively, evaluate their influence on relevant material properties, and ascribe them to their physical sources. Thus, the study of NRR centers is likely to remain an important and active research thrust for the realization of high efficiency AlGaN UV light emitting devices.

Several methods have been used to study the defect levels in GaN-based materials including deep-level transient spectroscopy (DLTS) [26–29], deep level optical spectroscopy (DLOS) [22,30], capacitance-voltage method [31,32], and photo-capacitance method [33]. However, all these methods are confined due to the necessity of preparing suitable samples for the measurement with Schottky contacts or an appropriate *p–n* junction. On the other hand, two-wavelength excited photoluminescence (TWEPL) is a versatile, non-contacting, non-destructive and purely optical characterizing scheme; there is no need for any special kind of sample preparation to investigate the deep levels (NRR centers) in the semiconductors.

1.2 Objectives

Crystal imperfections and various defect levels in AlGaN materials that act as nonradiative recombination (NRR) centers in the crystal are the main reason for the

reduction of efficiency, lifetime as well as reliability of the devices. It is indispensable to reduce or eliminate such NRR centers to improve the efficiency of AlGaN materials and overall the performance of AlGaN-based devices. In addition, understanding the basic physical properties of these materials is essential to control the defect formation in the crystal during the growth and also the device processing situation. The main objective of this research is to characterize the defect states acting as NRR centers in the various types of promising and high efficiency AlGaN-based light emitting semiconductor materials by TWEPL technique. To investigate the distribution of NRR centers within the forbidden energy gap of the materials by adding below-gap excitation (BGE) light with different photon energies using TWEPL technique is also an aim of this study. The second goal of this research is to propose carrier recombination model between the valence band (VB) and conduction band (CB) via NRR centers for the interpretation of experimental results and finally quantitative detection of NRR parameters by rate equation analysis.

1.3 Organization of the thesis

The motivation and objectives of this research are introduced in Chapter 1. The layout of this dissertation also presented here.

Chapter 2 deals with the background of this work. The basic properties of AlGaN-based materials and common defects present in these semiconductors are discussed. Fundamental of heterojunctions specially quantum well and multi-quantum well structures and Shockley-Read-Hall (SRH) recombination theory are briefly described there. A survey of prospects and application of two-wavelength excited photoluminescence is also presented in this chapter.

In chapter 3, detail experimental setup of conventional photoluminescence and two-wavelength excited photoluminescence (TWEPL) is demonstrated.

Chapter 4 describes the result of UV-C (deep ultraviolet) AlGaN MQW samples grown at different temperatures on sapphire substrate by metal-organic chemical vapor deposition (MOCVD) technique. A recombination model is proposed based on the experimental evidence. The effect of the growth temperature of samples on the formation of NRR centers has been explained. Defect related parameters have been estimated by model calculation and fitting the result with experiment.

Chapter 5 deals with the effect of the number of superlattice periods (SLPs) on NRR centers in *n*-AlGaN and quantum well (QW) layers of UV-B AlGaN MQW samples grown on c-plane sapphire substrates by MOCVD technique. A recombination model is proposed based on the experimental results. The rate equation analyses have been performed to justify the phenomenological recombination model.

In chapter 6, the temperature dependence of NRR processes in UV-B AlGaN QW by below gap-excitation light is described. A recombination model is proposed based on the experimental results to explain the temperature dependent TWEPL. The defect related parameters have been estimated by rate equation analyses from the recombination model.

Finally, the summary of this work and guideline for future research is presented in chapter 7.

CHAPTER 02

BACKGROUND

2.1 Basic properties of AlGaN materials

Aluminum gallium nitride (AlGaN) is an alloy of aluminum nitride and gallium nitride with useful semiconductor properties. It is a member of group III-nitride semiconductors and the most studied semiconductor for GaN microelectronics. There are basically two types of crystalline structures in group III-nitride semiconductors: the wurtzite (WZ) and zinc blende (ZB). There also be a laboratory form of crystalline structure 'rock salt' which only possible under very high pressure. The wurtzite (WZ) structure is thermodynamically and chemically stable under ambient conditions for bulk AlN, GaN, InN, and its alloys specially AlGaN [2]. The zinc blende structure for GaN and InN has been stabilized by epitaxial growth of thin films on (0 1 1) crystal planes of cubic substrates only.

The $Al_xGa_{1-x}N$ semiconductors cover a wide range of band-gap energies, depending on the value of Al composition (x), tailored from 3.4 eV (x = 0) to 6.2 eV (x = 1) [3,34]. The direct bandgap nature of these semiconductors makes them promising candidates for light emitting materials. The material is free from As, Hg, Pb, P (i.e. environmentally friendly) and its thermal conductivity is relatively high 1.3-2.1 W/cm.K. The material is hard which is suitable for long-lifetime device. These semiconductors also possess relatively high electron mobility, and high break-down filed. The high mobility and high breakdown field open great opportunities of fabricating high-power and high-frequency devices like photodetector, transistors, and switches. The Bandgap energies and emission wavelength of the wurtzite (WZ) InAlGaN material system and other III–V and II–VI compound semiconductor materials as a function of their lattice constant is shown in Fig. 2.1. However, InGaN and AlInN alloys with a high In content are still unfeasible due to the large mismatch between the lattice parameters which limiting the structural quality.

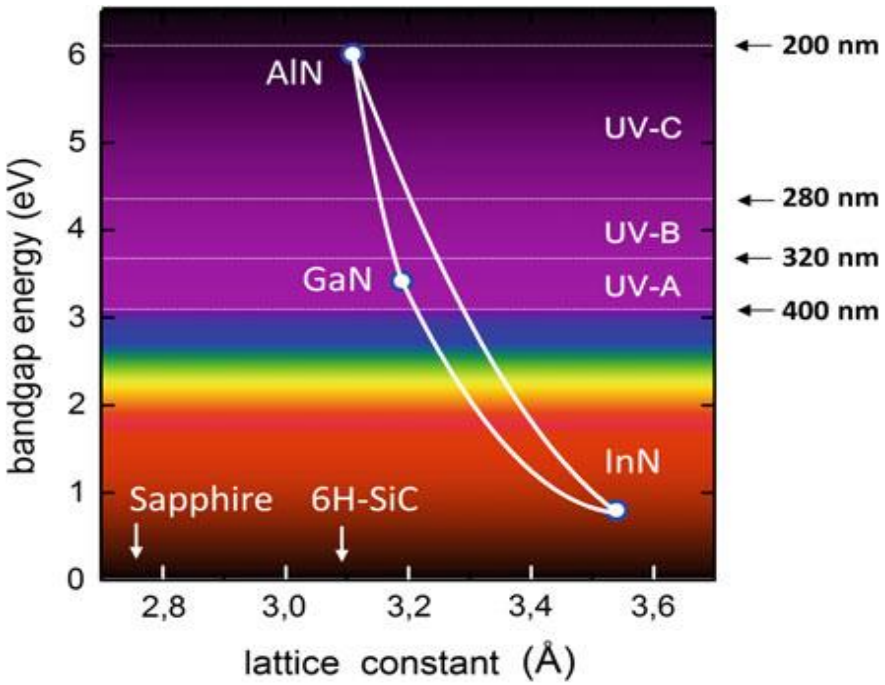

Fig. 2. 1 Bandgap energies and emission wavelength of InAlGaN material system and other III–V and II–VI compound semiconductor materials (adapted from Ref. [3]).

The dependencies of the energy bandgap of a ternary alloy $A_xB_{1-x}N$ on alloy composition x is assumed to fit a simple quardatic formula [35–37].

$$E_g(x) = xE_{g.A} + (1\text{-}x)E_{g.B} - bx(1-x) \qquad (2.1)$$

where $E_g(x)$ is the unstrained bandgap energy of the alloy, $E_{g.A}$ ($E_{g.B}$) is the bandgap of AN (BN) binary alloy, and b is the bowing parameter. The bowing parameter represents the second order correction to the linear dependence. A very good fitting is observed for the $Al_xGa_{1-x}N$ alloy when the value of b = 1 [35,36].

For comparison of the $In_xGa_{1-x}N$ alloys, a rather complex situation observed to estimate the bowing parameter b. In this case, it is quite difficult to describe the $E_g(x)$ curve with a single bowing parameter. The value of b depends on the In composition (x) and expressed by $b(x) = \alpha/(1+\beta x)$, where α and β are the fitting parameters. Recent few reported values of band bowing parameter b for the $Al_xGa_{1-x}N$ and $In_xGa_{1-x}N$ alloys are shown in Table 2.1.

Table 2. 1 Band bowing parameter b for $Al_xGa_{1-x}N$ and $In_xGa_{1-x}N$ alloys.

Alloys	Composition (*x*)	Bowing parameter (b) [eV]	References
$Al_xGa_{1-x}N$	$0 \le x \le 0.45$	0.69 ± 0.49	[38]
	$0 \le x \le 1$	1	[35,36]
$In_xGa_{1-x}N$	$0 \le x \le 0.12$	3.5	[39]
	$0 \le x \le 0.5$	1.4	[40]
	$0 \le x \le 1$	3.5 - 0.9	[36]

2.2 Defects in $Al_xGa_{1-x}N$ materials

Defect levels always exists in all crystals even though the development of high technology fabrication process. Common defects present in AlGaN crystal are shown in the following diagram (Fig. 2.2).

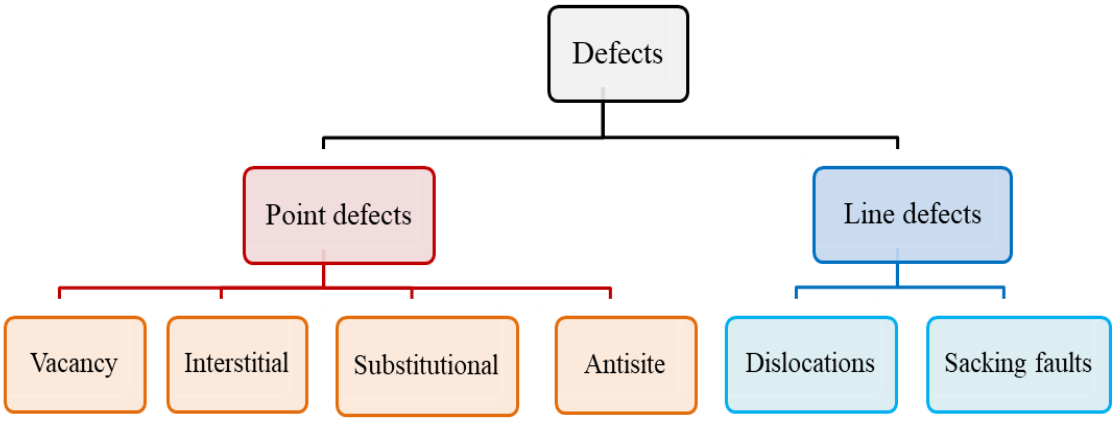

Fig. 2. 2 Common defects presents in $Al_xGa_{1-x}N$ crystal.

The point defects associated with a single atomic site and zero-dimensional defects. Point defects are where an atom is missing or is in an irregular place in the lattice structure. Point defects include vacancies, interstitial atoms, substitutional atoms and antisites. Vacancies are empty spaces where an atom should be but is missing. They are common, especially at high temperatures when atoms are frequently and randomly change their positions leaving behind empty lattice sites. For AlGaN semiconductors, vacancies can either be cation (V_{Al} and/or V_{Ga}) or anion (V_N) vacancies. If an atom is occupied in between regular atoms in spite of regular crystal site, it is called an interstitial impurity atom. When an impurity atom substitutes an atom of the host crystal, it is referred to as a substitutional impurity. Common examples of substitutional defects in AlGaN are Oxygen on N site (O_N), Carbon on N site (C_N), and Si on Al and/or Ga site

(Si_{Al} and/or Si_{Ga}). If the substitution occurs between the host atoms of the crystal, then it is called antisite defects, i.e., N on Ga site (N_{Ga}). Point defects can either be intrinsic or extrinsic depending on the involvement of atoms. Vacancies, self-interstitials, and antisites are intrinsic since they come from crystal itself. However, extrinsic point defects comprise of substitutional impurities and interstitial impurities due to the involvement of foreign atoms.

The line defects are one-dimensional defects which associated with a direction. Line defects include dislocations and stacking faults. Dislocations are defined as an abrupt change in the regular ordering of atoms along a dislocation line in the solid. Dislocation usually originates from the lattice and thermal coefficient mismatch between the substrate and succeeding layer. On the other hand, the partial displacements of the lattice ordering sequence which upset the regular sequence in the stacking of lattice planes is referred to stacking faults.

Aforementioned defects can be formed during AlGaN crystal growing, device processing, and by the working environment. To improve the performance of the devices, it is indispensable to understand the properties and the origin of the defects. A lot of effort has already been made to know the nature of defects in GaN materials. Depending on the earlier reports, a summary of the defect states present in the GaN is listed in Table 2.2.

Table 2. 2 Defect properties in GaN

Defects	Transition levels (E_T) [eV]	Charge states	References
O_N	Near E_C		[41,42]
Si_{Ga}	Near E_C		[42]
V_N-H	Near E_C		[42]
C_{Ga}	E_C - 0.11 E_C - 0.18		[43] [41,44]
I_C	E_C - (1.28 - 1.35)		[43]
V_{Ga}	E_V + 2.06 E_V + 1.1 (E_C - 2.3) E_V + 0.8	3-/2- 3-/2- 2-/-	[45,46] [42,43,47] [42]
V_{Ga}-O_N	E_V + 1.85 E_V + 1.76 E_V + 1.1 E_V + 0.7	0/- 2-/- 2-/- -/0	[45] [45] [42,47] [42]
V_{Ga}-Si_{Ga}	E_V + 1.74 E_V + 2.13	0/- 2-/-	[45] [45]
C_N-O_N	E_V + 0.75 E_V + 0.14	0/+ +/2+	[41] [41]
C_N	E_C - 3.28 E_V + (0.43 - 0.48) E_V + 0.9 E_V + (1.06 - 1.09)	 0/+ -/0 -/0	[43] [41,45] [48] [41,45]
Mg_{Ga}	E_C - 3.22		[43,49]

The defects present in GaN also propagate to $Al_xGa_{1-x}N$ alloys just changing their transition energies with the incorporation of Al content in GaN. Besides these, new defects also incorporated to the $Al_xGa_{1-x}N$ alloys due to the lattice mismatch between the substrate and $Al_xGa_{1-x}N$.

2.3 Quantum well and multi-quantum wells

A quantum well (QW) is a particular kind of heterostructure in which one thin "well" layer is surrounded by two "barrier" layers. In another words, a QW is a special kind of heterostructure formed by two heterojunctions or three layers of materials such that the middle layer has the lowest energy for electrons or the highest energy for holes. The electrons and holes are both confined in this thin layer, and it is so thin (typically about 100 Å, or about 40 atomic layers) that we cannot neglect the fact that the electron and hole are both waves. In fact, the allowed states in this structure correspond to standing waves in the direction perpendicular to the layers. Because only particular waves are standing waves, the system is quantized, hence the name "quantum well".

A quantum well confines carriers (electrons or holes) in a two-dimensional (2-D) system. In a bulk semiconductor, electron can be moved in all directions (3D) and their energy above the conduction band edge is continuous and can be expressed by [50]

$$E - E_C = \frac{\hbar}{2m_e^*}(k_x^2 + k_y^2 + k_z^2) \qquad (2.2)$$

where m_e^* is the associated effective mass of electrons. The carriers are confined in one direction (say *x*-direction, k_x=0) inside the QW, thus, the energy is no longer continuous on the *x*-direction but becomes quantized in sub-bands.

The quantization of carriers inside the well depends on two important parameters: well width, L_x, and well height, ϕ_b. Solution of the Schrödinger equation inside the well is

$$\Psi(x) = sin\left(\frac{i\pi x}{L_x}\right) \qquad (2.3)$$

and $\Psi(x)$ will be zero in the boundaries if and only if ϕ_b is infinite. The pinning of nodes at the well boundaries leads to the quantization of sub-bands with an energy of

$$E_i = \frac{\hbar^2\pi^2 i^2}{2m^* L_x^2} \qquad (2.4)$$

The minimum requirement to be a quantum well is that the quantized energy is much larger than *kT,* and L_x is smaller than the mean free path and the de-Broglie wavelength [50]. If the quantum wells are separated from one another by thick barrier layers and there is no communication between them, then the system is called multiple quantum wells (MQWs). Multiple quantum wells are a key feature of modern high-efficiency optical devices.

2.4 Shockley-Read-Hall (SRH) recombination theory

One of the major important factors for light emitting diodes (LEDs) and laser diodes (LDs) is the carrier recombination. For the understanding of light emitting mechanism, it is essential to know the recombination physics. Defects inside the semiconductor crystal can introduce energy levels within the bandgap, usually known as trap levels or non-radiative recombination (NRR) centers. Recombination of electrons and holes at NRR centers is the most important mechanism that influences the carrier lifetime.

The electron and hole emission and capture mechanism at NRR centers were firstly explained and formulated comprehensively by William Shockley and W. T. Read, Jr. [51] and by R. N. Hall [52] in 1952. These are known as the Shockley-Read-Hall (SRH) recombination statistics. The four possible transitions mechanism of an electron or hole within the bandgap between a trap and the conduction band (CB) or the valence band (VB) are depicted in Fig. 2.3

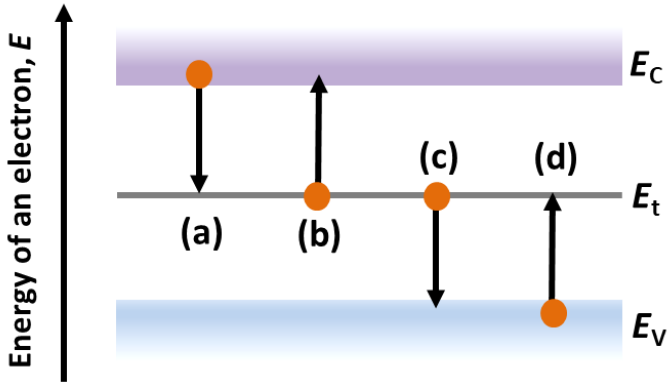

Fig. 2. 3 Basic processes involved in Shockley-Read-Hall recombination by trapping; (a) electron capture, (b) electron emission, (c) hole capture, and (d) hole emission.

Here, E_t represents the energy level of the trap. E_v and E_c denotes the VB and CB energies, respectively.

The four processes are:

(a) Electron capture process: An electron is captured by an empty center or unoccupied electron trap from the conduction band,

(b) Electron emission process: This is just the reverse process of electron capture. In this case, a trapped electron is released or emitted to the conduction band.

(c) Hole capture process: A hole is captured by a trapped electron from the valence band. This can be indicated by a transition of a trapped electron to an unoccupied electron state in the valence band.

(d) Hole emission process: This is the reverse process of hole capture. In this case, a hole is released or emitted from the unoccupied electron trap. It can be explained by capture of an electron from the valence band.

The electron occupation function of the trap (f) is expressed by Fermi-Dirac statistics and it depends on the energy level of the trap (E_t) and the Fermi level (E_F):

$$f = \frac{1}{1 + exp[(E_t - E_F)/kT]} \quad (2.5)$$

where, T is the temperature, and k is the Boltzmann constant. Thus, the probability of that state become empty or occupied by the hole is (1- f).

$$f_p = 1 - f = f exp[(E_t - E_F)/kT] \quad (2.6)$$

The rate of electron capture (r_a) is proportional to the concentration of free electrons n and the concentration of traps not occupied by electrons. Thus,

$$r_a = v_{th}\sigma_n n N_t(1 - f) \quad (2.7)$$

where v_{th} is the speed of an electron, σ_n is the capture cross-section for electrons, n is the electron concentration, N_t is the trap density, and f is the probability of occupation of a center by an electron. The average probability of an electron be captured per unit time by an empty trap is called as the electron capture coefficient and expressed by

$$C_n = v_{th}\sigma_n \quad (2.8)$$

where, C_n [cm^3s^{-1}] is the electron capture coefficient.

The rate of electron emission (r_b) is proportional to the concentration of traps which are occupied by electrons. Thus,

$$r_b = e_n N_t f \quad (2.9)$$

where e_n is the electron emission coefficient from the trap.

The hole capture rate, by analogy to process (a), is given by

$$r_c = v_{th}\sigma_p p N_t f = C_p p N_t f \quad (2.10)$$

where, C_p is the hole capture coefficient, and p is the hole concentration.

Finally, the rate of hole emission, process (d), is

$$r_d = e_p N_t(1 - f) \quad (2.11)$$

where, e_p is the hole emission coefficient from the trap.

Now at thermal equilibrium condition the rate of capture and rate of emission must be equal, i.e.:

$$r_a - r_b = r_c - r_d = 0 \quad (2.12)$$

and the Fermi level (E_F) must be replaced by intrinsic Fermi level (E_i).

The free carrier densities can be calculated by using the Boltzmann statistics;

$$n = n_i exp[(E_F - E_i)/kT], \quad \text{and } p = n_i exp[(E_i - E_F)/kT] \tag{2.13}$$

Then the electron emission coefficient is

$$e_n = v_{th}\sigma_n n_i exp[(E_t - E_i)/kT] \tag{2.14}$$

and the hole emission coefficient is

$$e_p = v_{th}\sigma_n n_i exp[(E_i - E_t)/kT] \tag{2.15}$$

On the other hand, in the non-equilibrium, but in steady state condition

$$r_a - r_b = r_c - r_d \neq 0 \tag{2.16}$$

Let us consider that, Eq. (2.14) and (2.15) continue to be valid in the out of equilibrium. From Eq. (2.7), (2.9) - (2.11), and (2.16) the electron occupation function can be evaluated as:

$$f = \frac{\sigma_n n + \sigma_p n_i exp[(E_i - E_t)/kT]}{\sigma_n\left[n + n_i exp[(E_t - E_i)/kT]\right] + \sigma_p\left[p + n_i exp[(E_i - E_t)/kT]\right]} \tag{2.17}$$

Substituting Eq. (2.17) in Eq. (2.7) and (2.9) and assuming that the capture cross-section of holes and electrons are equal ($\sigma_p = \sigma_p = \sigma$), the net recombination rate of electrons and holes can be obtained by

$$r_a - r_b = r_c - r_d = \sigma v_{th} N_t \frac{pn - n_i^2}{p + n + 2n_i cosh[(E_i - E_t)/kT]} \tag{2.18}$$

2.5 Two-wavelength Excitation PL (TWEPL): a powerful tool for defect characterization

The two-wavelength excited photoluminescence (TWEPL) is a purely optical, non-contacting, and non-destructive technique for optical characterization of semiconductor materials. Previously, Grimmeiss and Monemar in 1973 used TWEPL method for characterizing Cu-doped GaN who are known as the pioneer of this technique [53]. Afterwards, Monemar and Samuelson in 1978 analyzed the bulk GaP by utilizing both the PL excitation (PLE) and the twofold excitation method [54]. In early 1980's, Tajima investigated the deep level defects in bulk GaAs by utilizing the twofold excitation modulated PL technique and succeeded in the detection of a high concentration

of NRR centers in his measuring samples [55]. Kamata et al. in 1993, characterized the NRR centers in GaAs/AlGaAs MQWs by TWEPL [56]. They estimated trap parameters of the NRR centers by combined analysis of time-resolved PL (TRPL) and TWEPL results by considering multi-level traps in GaAs/AlGaAs MQWs structures. Recently, Dagnelund et al. given a clear insight of this technique by reporting detection and characterization of hole traps in Ga(In)NP [57]. As a results of this success of quantitative detection of NRR parameters by TWEPL method, a lot of research has already been done for GaAs/AlGaAs quantum wells [58–66], GaN/InGaN QWs [66,67], GaN [68–70], AlGaN QWs [71–74], GaPN [75], and $Ba_3Si_6O_{12}N_2:Eu^{2+}$ phosphors [76,77].

It is essential to determine the spatial and energy distribution of NRR centers for classifying each defect state and to locate its microscopic origin. By using different BGE sources with suitable photon energies, it is possible to know such energy distribution of NRR centers. The detail experimental layout and the measurement procedure by TWEPL system has been discussed in next chapter.

CHAPTER 03

EXPERIMENTAL DETAILS

3.1 Photoluminescence

Photoluminescence (often referred to as PL) is a powerful and widely used measurement technique for probing the electronic structure and in the analysis of the optical properties of materials. It is a versatile, non-contacting and non-destructive scheme to obtain information on the internal optical processes and the optical quality of the material. The material (in an equilibrium state) is excited by a light whose photon-energy is higher than the bandgap of the material. The light is absorbed and imparts excess energy into the material in a process called photo-excitation. Electron-hole pairs are generated inside the material and the electrons are excited from the valence band (VB) of the material to its conduction band (CB). The excited photo-carriers return to the equilibrium state through radiative and/or non-radiative recombination process. One of the ways to release such excess energy from the material is by the emission of light. This is called luminescence. As the photoexcitation occurs by the optical radiation hence the name photoluminescence (PL). The PL intensity for the radiative recombination process is recorded as a function of wavelength to get a spectral plot. The spectral plot provides various information such as the bandgap of the material, mid-states and defect levels, the optical quality of the material etc. The peak wavelength (λ_p) in the PL spectra is directly related to the bandgap energy (E_g) of the material through the following equation:

$$E_g = \frac{hc}{\lambda_p} \qquad (3.1)$$

where, h (6.62607015×10^{-34} J.s.) is the Planck constant and c (2.99792458×10^{8} m.s^{-1}) is the speed of light.

3.2 Two-wavelength Excited Photoluminescence (TWEPL)

The two-wavelength excited photoluminescence (TWEPL) is a purely optical, non-contacting, and non-destructive technique for optical characterization of semiconductors. In conventional PL, the sample is excited by a light source whose excitation energy is higher than the bandgap energy of the material ($h\nu_{BGE} > E_g$). Hereafter, this source is indicated to as above-gap excitation (AGE) source. In the TWEPL, an intermittent below-gap excitation (BGE) light whose photon energy is lower than the bandgap energy of the material ($h\nu_{BGE} < E_g$) is superposed on the constant AGE light in PL measurement as shown in Fig. 3.1. The PL intensities with and without the BGE light is recorded as $I_{(AGE+BGE)}$ and $I_{(AGE)}$, respectively. The normalized PL intensity (I_N) is calculated by

$$I_N = \frac{I_{(AGE+BGE)}}{I_{(AGE)}} \tag{3.2}$$

The deviation of I_N value from unity indicates the presence of nonradiative recombination (NRR) centers in between the energy bandgap of the material.

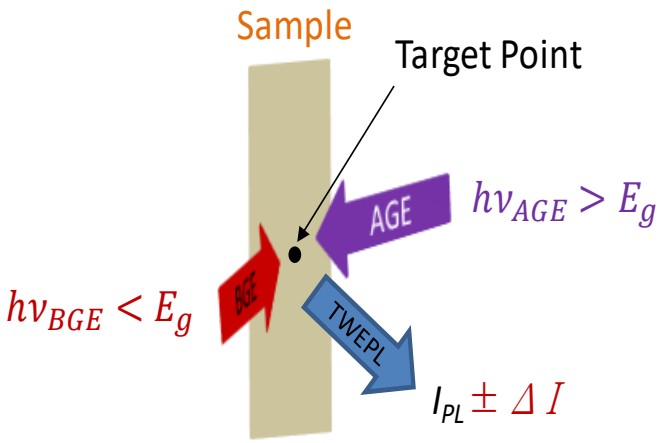

Fig. 3. 1 Schematic diagram of the TWEPL measurement.

After irradiation of a BGE light on a fixed AGE light, three cases may happen:

(i) No change in PL intensity: It reflects that there is no NRR centers exist in the bandgap region of the material corresponding to the energy of the BGE.

(ii) Enhancement of PL intensity: It can be interpreted by one-level recombination model as shown in Fig. 3.2(a). The BGE excites the electrons from the VB to an NRR level or from an NRR level to the CB. As a consequence, an increase of either hole (Δp) or electron (Δn) concentration in the VB or CB, respectively and

the PL intensity increases due to its direct proportional relationship with the product of *n* times *p*.

(iii) Diminution of PL intensity: It can be explained by a two-level recombination model schematically depicted in Fig. 3.2(b). When the BGE energy matches the energy difference between two coexisting below-gap NRR levels, level-1 and level-2, electrons in NRR level-1 are excited to NRR level-2, from which they recombine nonradiatively with holes in the VB of the material. Consequently, a number of electron deficiencies occur in NRR level-1, which allows for an increase in NRR from the CB. The combination of both effects reduces the number of electron-hole pairs available for radiative recombination and results in the PL intensity quenching.

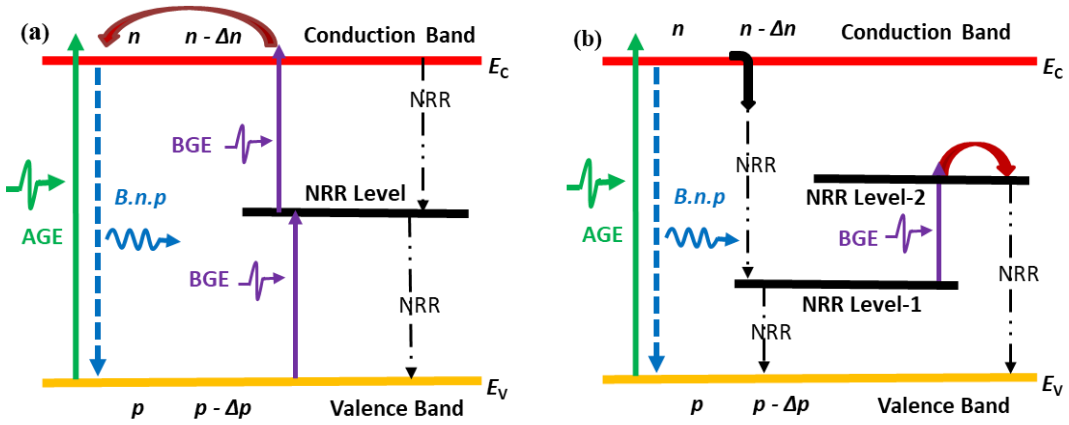

Fig. 3. 2 (a) One-level model which explains the enhancement of the PL intensity, (b) Two-level model used for the illustration of the PL intensity quenching.

The typical experimental layout of the TWEPL is shown in Fig. 3.3. The sample was mounted on a Cu holder with the sapphire side up inside a temperature-controlled cryostat with three optical windows. A closed loop He cycles was used for the cooling of the sample and temperature can be varied from 20 K to 300 K. Before cooling of the sample, the cryostat was evacuated at a pressure of around 10^{-4} Pa. A continuous wave (CW) diode pumped solid state laser (Model: SDL-266-005T) of wavelength 266 nm ($h\nu_{AGE}$ = 4.66 eV) have been used as the AGE source for the excitation of different samples. Four different BGE light sources with energies 0.93 eV (1340 nm wavelength), 1.17 eV (1064 nm), 1.27 eV (980 nm), and 1.46 eV (850 nm) have been used in the experiment of TWEPL measurement.

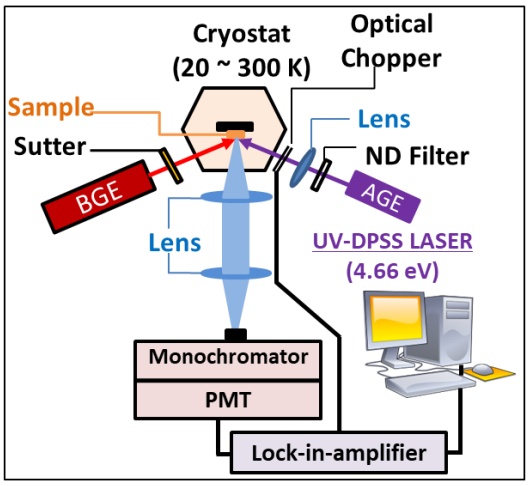

Fig. 3. 3 Typical experimental setup for the TWEPL measurements.

The output power of the AGE LD source was kept constant and different neutral density (ND) filters were used for changing the excitation density. The long pass (LP) filter was used to stop the shorter wavelength component from the BGE source. Two optical shutters were placed in front of the AGE and BGE sources to control them. The emitted PL signal from the sample was guided by collimating lens to enter into a monochromator with range 200 nm - 1800 nm and then detected by near infrared photomultiplier for the conversion into electrical signal. Finally, the signal was recorded by a computer. Here an optical chopper was used with the digital lock-in-amplifier for improving the S/N ratio of the PL signal. The slit width of the monochromator was 0.5 mm. In front of the monochromator slit, a LP 275 nm filter was used to cut the unwanted AGE source (266 nm) emission and to record only from the sample's emission.

The measurement technique of the PL intensities $I_{(AGE)}$ and $I_{(AGE+BGE)}$ for the calculation of the normalized PL intensity (I_N) in both the cases when the PL intensity increases (one-level model) and PL intensity decreases (two-level model) with the addition of BGE light on the AGE light in the TWEPL measurement is shown in Fig. 3.4.

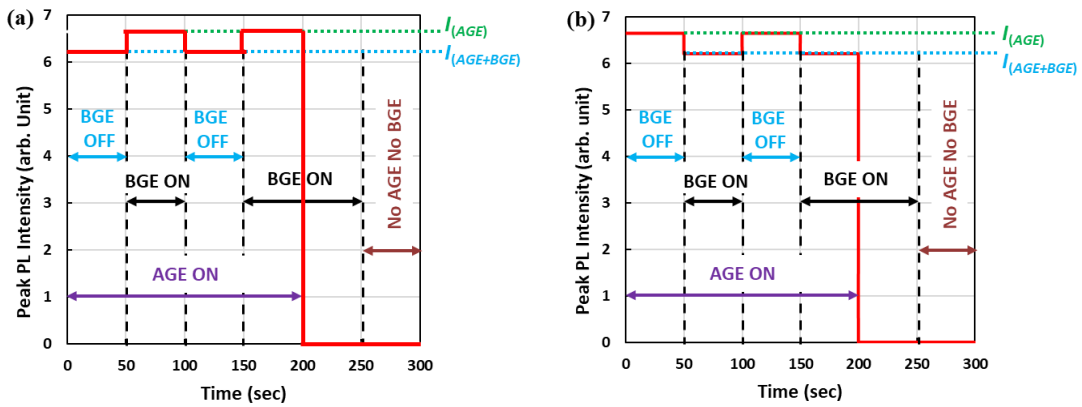

Fig. 3. 4 Measurement technique of $I_{(AGE)}$ and $I_{(AGE+BGE)}$ for the calculation of I_N when (a) the PL intensity increases (one-level model) and (b) PL intensity decreases (two-level model) with the addition of BGE on the AGE in the TWEPL measurement.

At first the conventional PL spectra was measured only by the AGE light and the PL peak position was recorded. Then the time variation of the PL peak intensity was recorded (using a software) by turning ON and OFF of the optical shutters placed in front of the AGE and BGE light sources (Fig. 3.3) as shown in Fig. 3.4. After averaging all $I_{(AGE)}$ and $I_{(AGE+BGE)}$ values individually, the normalized PL intensity I_N was calculated by using Eq. 3.2. During the measurement, it was confirmed that both the AGE and BGE light sources superposed on the same point of the sample surface and spot size of the BGE light was higher than that of the AGE light on the target point of sample surface.

CHAPTER 04

EFFECT OF GROWTH TEMPERATURE ON NONRADIATIVE RECOMBINATION CENTERS IN UV-C AlGaN QW

4.1 Introduction

High-quality AlGaN materials are the key element in obtaining the high efficiency of the deep ultraviolet light emitting diode (DUV-LED), which are used in varieties of potential applications like sterilization, optical and biological sensing, skin curing, etc. etc [10,78–80]. The wavelength range between 260 nm to 280 nm is most important for applications involving sterilization or water purification with direct UV light treatment [10,81–87]. The external quantum efficiency has improved in recent years, but it is still crucial to find the optimum growth conditions of AlGaN-based DUV LEDs [10,74,79,80]. However lack of lattice-matched and cost-effective substrates brings difficulties in reducing the density of defect states, which act as nonradiative recombination (NRR) centers in multiple quantum wells (MQWs) [3,23–25]. In order to improve the efficiency of light-emitting materials, it is essential to reduce such NRR centers. Photoluminescence (PL) and cathodoluminescence spectroscopy have been used by other groups to investigate below-gap states in AlGaN, showing only characteristic luminescence peaks and giving relative information about NRR centers [88,89]. To investigate deep-level defects in AlGaN films, deep-level transient spectroscopy and deep-level optical spectroscopy have been used, but their applications are restricted due to the necessity of preparing suitable samples for the measurement with Schottky contacts or an appropriate *p–n* junction [90–92]. We have been studying such NRR centers optically since the first quantitative determination of their NRR parameters by our scheme of two-wavelength excited PL (TWEPL) [58,64]. It is a versatile non-contacting and non-destructive scheme;

there is no need for any special kind of sample preparation. In this work, the TWEPL method is used for the detection and characterization of NRR centers in AlGaN MQW samples grown on sapphire substrates. The variation of peak PL intensity due to the addition of the below-gap excitation (BGE) light over that of the above-gap excitation (AGE) is observed as functions of AGE photon number density, BGE photon number density, and BGE energy. The NRR parameters are also evaluated by systematically solving the rate equations and fitting the results with experimental data.

4.2 Experimental methods

4.2.1 Sample structure

Our MQW samples comprise a 4 μm thick multi-layer AlN buffer, a 1.5 μm thick Si-doped *n*-AlGaN layer, three periods of MQWs with 5 nm thick wells and 8 nm thick barriers, a multi-quantum barrier (MQB), and finally a 55 nm thick Mg doped p-AlGaN contact layer. This sample structure is depicted in the inset of Fig. 4.1. Samples were grown on (0001) sapphire substrates by metal–organic chemical vapor deposition (MOCVD) technique. The growth conditions of the two samples was identical except for the growth temperature: the growth temperature of sample A was 1140 °C while that for sample B was 1180 °C. Due to the difference in their growth temperature, the Al content in each layer and the layer thickness are different. The Al composition (x) in the $Al_xGa_{1-x}N$ of sample A in the barrier, well, and final barrier layers were 0.57, 0.44, and 0.65, respectively; these values for sample B were, respectively, 0.55, 0.42, and 0.63.

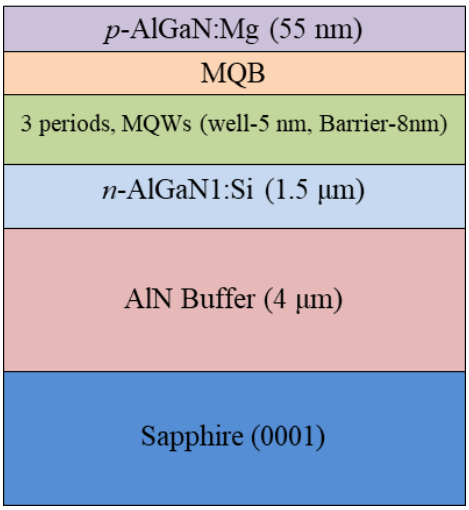

Fig. 4. 1 Sample structure.

4.2.2 Measurement

The experimental setup of the TWEPL method for characterizing the AlGaN MQW samples is shown in Fig. 4.2. To obtain the PL signal, the sample was mounted on a Cu holder with the sapphire side up inside a temperature-controlled cryostat with three optical windows. A continuous wave AGE light ($h\nu_{AGE} > E_g$) of $h\nu_{AGE}$ = 4.66 eV (266 nm) yields MQW-PL. By superposing a chopped BGE light ($h\nu_{BGE} < E_g$) on an AGE light at the same point of the sample surface, we measure the MQW-PL intensities with and without the BGE, $I_{AGE+BGE}$ and I_{AGE}, respectively. The normalized PL intensity is defined as $I_N = I_{AGE+BGE}/I_{AGE}$, and its deviation from unity indicates the presence of NRR centers [58,64]. The BGE light sources with energies 0.93 eV (1340 nm wavelength), 1.17 eV (1064 nm), 1.27 eV (980 nm), and 1.46 eV (852 nm) are used in the experiment. The detailed experimental layout and models of NRR centers can be found elsewhere [64,74,93].

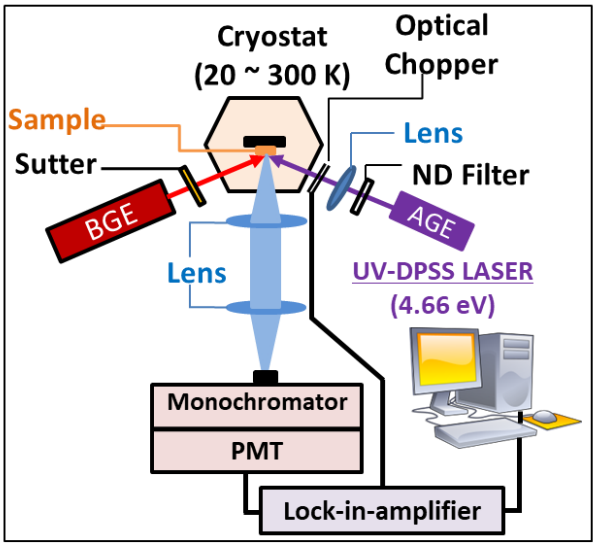

Fig. 4. 2 Experimental setup for TWEPL measurements.

4.3 Results and discussion

4.3.1 PL intensity comparison

Conventional PL spectra were measured for two samples at 20 K with varying excitation (AGE) power. Figure 4.3(a) shows the comparison of the PL spectra between sample A and sample B at a fixed excitation power density of 1.24 mW·mm^{-2} and at 20 K. The PL peak wavelengths of samples A and B at 20 K are 276 nm and 284.5 nm, respectively. The integrated PL intensity was calculated as a function of AGE photon

number density for both samples, as shown in Fig. 4. 3(b). The integrated PL intensity of MQW emission increases almost linearly with increasing AGE photon number density for both samples. The rate of increase for sample B is higher than that of sample A, thus showing a higher emission efficiency of sample B.

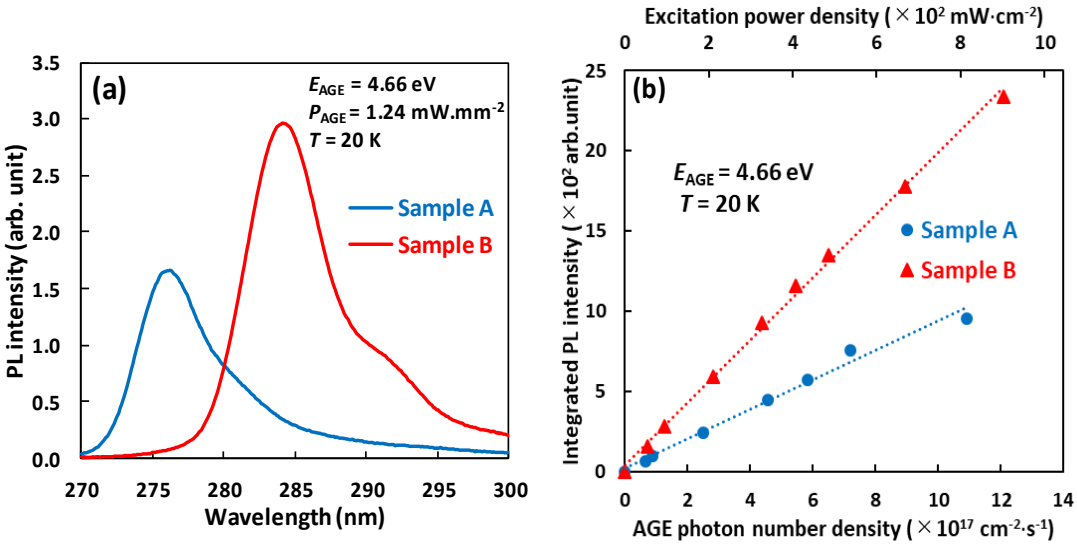

Fig. 4. 3 Comparison of PL intensities between samples A and B. In Fig. (b) the corresponding excitation power density in mW·cm^{-2} is shown in the upper axis. Here, the dotted lines in (b) are only to guide the eyes.

In Fig. 4.4(a), the temperature-dependent integrated PL intensity of samples A and B are shown. At the temperature region below 100 K, the integrated PL intensity of sample B is higher than that of sample A, which is consistent with the results shown in Fig. 4.3. With temperature increasing from 20 K, the integrated PL intensity slightly increases for both samples due to the carrier transportation between different localized states [94,95]. With a further increase in temperature from 30 K, the integrated PL intensity decreases drastically for sample B but monotonically from 50 K for sample A. This implies that sample B has a stronger temperature effect than sample A. The thermal quenching behaviour is determined by the activation of NRR centers and the escape of carriers from QWs [96,97]. The latter mechanism is negligible in this low-excitation condition.

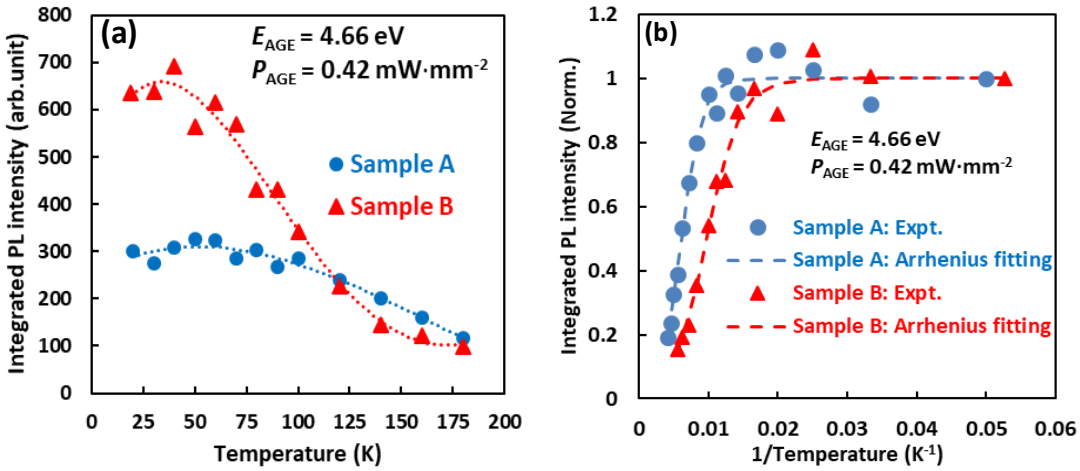

Fig. 4. 4 Comparison of integrated PL intensities as a function of (a) temperature, and (b) inverse temperature between samples A and B. The dotted lines in (a) are only to guide the eyes. The broken lines in (b) are the Arrhenius fittings. Here "Expt." in (b) indicates the experimental results.

The temperature-dependent PL intensity can be well fitted, as shown in Fig. 4.4(b), using the following two-channel Arrhenius formula [96–100]:

$$I(T) = \frac{1}{\left[1 + C_1.\exp\left(\frac{-E_1}{K_B T}\right) + C_2.\exp\left(\frac{-E_2}{K_B T}\right)\right]}, \qquad (4.1)$$

where $I(T)$ represents the normalized integrated PL intensity at temperature T. C_1 and C_2 are the two constants related to the density of NRR centers in the samples. E_1 and E_2 stand for the thermal activation energies at low- and high-temperature ranges corresponding to NRR process, [97,100] and k_B is the Boltzmann's constant. All the values of the parameters in Eq. (4.1) are shown in Table 4.1.

Table 4. 1 The obtained fitting parameters in Eq. (4.1).

Sample	C_1	E_1 (meV)	C_2	E_2 (meV)
A	160	85.7	14.5	44.4
B	43.7	34.1	24.2	51.4

It is observed from Table 4.1 that though the values C_1 and E_1 for samples A are higher than that of sample B at lower temperature region, the sample B contains higher values of C_2 and E_2 at high temperature ranges than that of sample A. Higher activation

energy shows lower temperature effect which is consistent with the results shown in Fig. 4.4 (a).

4.3.2 TWEPL measurement

In order to know the distribution of NRR centers in AlGaN MQW samples, the normalized PL intensity I_N was measured as a function of BGE photon number density for four BGE energies as 0.93 eV, 1.17 eV, 1.27 eV, and 1.46 eV, respectively, as shown in Fig. 4.5. The AGE power density was fixed at 0.42 mW·mm^{-2} and the measurement temperature was between 20 K and 29 K. With the addition of BGE light on the AGE, the value of I_N decreased from unity for all BGE energies.

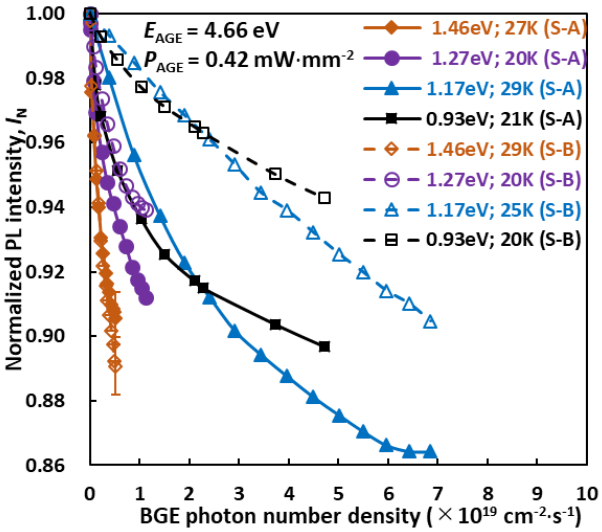

Fig. 4. 5 Variation of I_N values as a function of BGE photon number density for samples A and B. Here "(S-A)" and "(S-B)" indicate sample A and sample B respectively.

It is observed from Fig. 4.5 that the amount of PL quenching becomes pronounced with increasing BGE energy and photon number density. The most dominant quenching occurred by the 1.46 eV BGE energy at the BGE photon number density of around 0.52×1019 cm^{-2}·s^{-1} for both samples; the difference between the two samples is within experimental error. Furthermore, the value of I_N for sample A is lower than that of sample B throughout the experimental BGE photon number density range except at the 1.46 eV BGE energy. The minimum values of I_N, 0.91 and 0.94, were obtained for samples A and B, respectively, at the highest BGE density (1.1×1019 cm^{-2}·s^{-1}) for the 1.27 eV BGE energy. For BGE energies of 1.17 eV (at 6.85×10^{19} cm^{-2}·s^{-1}) and 0.93 eV (at 4.72×10^{19} cm^{-2}·s^{-1}), the minimum I_N values were 0.864 and 0.905, and 0.986 and 0.943, for samples

A and B, respectively. The degree of quenching of I_N from unity represents the density of NRR centers in the samples. Thus, this result implies that the densities of NRR centers corresponding to the 1.46 eV BGE are nearly similar, but those corresponding to other energies are higher in sample A than in sample B. We consider that the presence of higher-density NRR centers corresponding to the 0.93 eV, 1.17 eV, and 1.27 eV BGE energies results in the lower PL intensity of sample A.

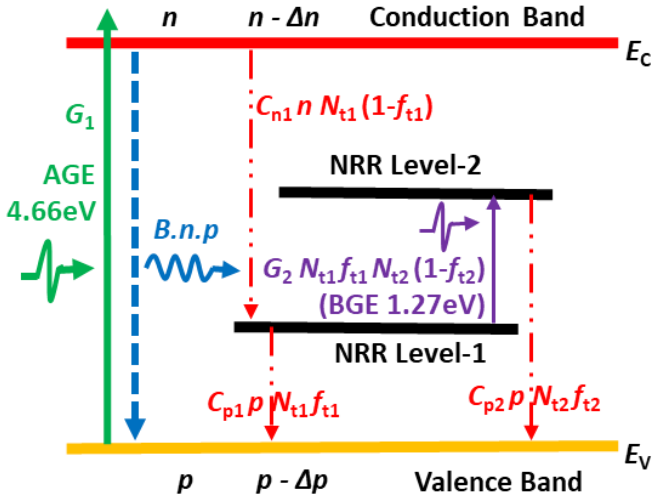

Fig. 4. 6 Two-level recombination model of NRR process, which explains the PL intensity quenching due to the irradiation of BGE.

The diminution of I_N values (Fig. 4.5) can be explained by the two-level recombination model schematically depicted in Fig. 4.6. The figure shows the presence of a pair of NRR centers in the sample whose energy difference corresponds to that of the BGE energies [53,64,73,101]. Here, G_1 ($cm^{-3}\cdot s^{-1}$) is the generation rate of AGE, G_2 ($cm^3\cdot s^{-1}$) is the BGE coefficient from NRR level-1 to NRR level-2, B ($cm^3\cdot s^{-1}$) is the radiative recombination coefficient, C_n and C_p are the electron and hole capture coefficients, respectively, N_t is the density of NRR levels, and f_{t1} and f_{t2} are the electronic occupation functions of NRR level-1 and NRR level-2, respectively. The NRR parameters can be found by fitting experimental results based on Shockley–Read–Hall statistics [64,102].

When the BGE energy matches the energy difference between two coexisting below-gap NRR levels, level-1 and level-2 (Fig. 4.6), electrons in NRR level-1 are excited to NRR level-2, from which they recombine nonradiatively with holes in the valence band of AlGaN. Consequently, a number of electron deficiencies occur in level-1, which allows

an increase in NRR from the conduction band. The combination of both effects reduces the number of electron-hole pairs available for radiative recombination and results in the PL intensity quenching. In the low-BGE photon number density region, the electron occupation function of NRR level-2 remains much lower than unity, and the PL quenching avails with the increase in the BGE photon number density. Moreover, with a further increase in the BGE photon number density, the electron occupation function of NRR level-2 approaches unity and the slope of PL quenching becomes gentle; this is partly shown in Fig. 4.5.

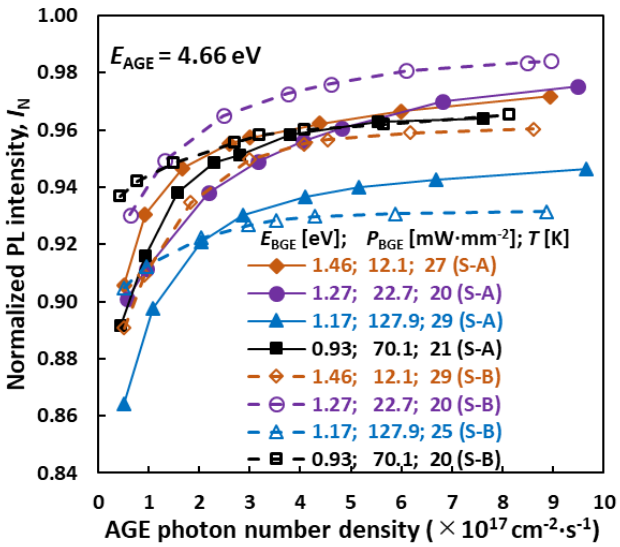

Fig. 4. 7 Variation of I_N as a function of AGE photon number density for samples A and B. Here "(S-A)" and "(S-B)" indicate sample A and sample B respectively.

Figure 4.7 shows the variation of I_N values as a function of AGE photon number density for four BGE energies from 0.93 eV to 1.46 eV. With increasing AGE photon number density, the value of I_N first increases and then approaches unity for both the samples. The excitation of electrons from NRR level-1 to NRR level-2 due to the BGE increases the NRR rate from level-1 and level-2 to the valence band (VB) at a lower AGE photon number density. With increasing AGE photon number density, band-to-band radiative recombination becomes stronger since the rate is proportional to n times p. Consequently, the normalized PL intensity I_N approaches unity with increasing AGE photon number density. A similar tendency was observed in our previous studies of TWEPL [64,71,73,102,103].

4.3.3 Rate equation analysis

In order to consolidate our qualitative interpretation by the two-level model, a semi-quantitative simulation of the TWEPL results was carried out for the most dominant and second-most dominant PL quenching occurred by the 1.46 eV and 1.27 eV BGE energies, respectively. The rate equations for this two-level model (Fig. 4.6) can be written [51,52,64] as

$$\left.\begin{aligned}
\frac{dn}{dt} &= G_1 - Bnp - C_{n1} n N_{t1}(1 - f_{t1}) = 0, \\
\frac{dp}{dt} &= G_1 - Bnp - C_{p1} p N_{t1} f_{t1} - C_{p2} p N_{t2} f_{t2} = 0, \\
\frac{df_{t1}}{dt} &= C_{n1} n(1 - f_{t1}) - C_{p1} p f_{t1} - G_2 f_{t1} N_{t2}(1 - f_{t2}) = 0, \\
\frac{df_{t2}}{dt} &= G_2 N_{t1} f_{t1}(1 - f_{t2}) - C_{p2} p f_{t2} = 0,
\end{aligned}\right\} \qquad (4.2)$$

while considering the charge neutrality condition

$$n + N_{t1} f_{t1} + N_{t2} f_{t2} = n_0 + p, \qquad (4.3)$$

where n_0 is the density of free electrons in the QWs and its value is known (2.0×10^{17} cm^{-3}) from the samples' growers. The generation rate of the AGE (G_1) is calculated experimentally by using the following equation [104,105]:

$$G_1 = P_{laser}(1-R)\alpha \Big/ \left(A_{spot} h\nu\right), \qquad (4.4)$$

where P_{laser} is the excitation power, R (18%) is the Fresnel reflection at the sample surface, A_{spot} is the laser spot size on the sample surface, $h\nu$ (4.66 eV) is the photon energy of the excitation laser, and α (3.1×10^5 cm^{-1}) [106] is the absorption coefficient of AlGaN at 266 nm. It is impossible to evaluate the BGE coefficient (G_2) from the absorption coefficient measurement since there is no fundamental absorption for these sources. Here, we use a constant factor for these conversions from the experimental photon number density of the BGE sources [102]. The system of rate equations can be solved numerically, and the dependencies of n, p, f_{t1}, and f_{t2} on G_2 can be found for the constant parameters of G_1, B, n_0, C_{n1}, C_{p1}, and C_{p2}. Therefore, we postulated the parameters C_{n1}, C_{p1}, and C_{p2} from our previous result of similar growth conditions and changed the actual fitting parameters of G_2, N_{t1}, and N_{t2}. The radiative recombination coefficient B is considered as 1.0×10^{-11} $cm^3\cdot s^{-1}$ for the AlGaN material [102,107–109]. By systematically solving and fitting the

result with experimental data, the NRR parameters are obtained for both samples, and are shown in Table 4.2 (for the 1.46 eV BGE) and Table 4.3 (for the 1.27 eV BGE).

Table 4. 2 Parameters of rate Eqs. (4.2) and (4.3) for BGE 1.46 eV of samples A and B.

Sample	N_{t2} [cm^{-3}]	N_{t1} [cm^{-3}]	G_1 [$cm^{-3}\cdot s^{-1}$]	B [$cm^{-3}\cdot s^{-1}$]	n_0 [cm^{-3}]	C_{n1} [$cm^{-3}\cdot s^{-1}$]	C_{p1} [$cm^{-3}\cdot s^{-1}$]	C_{p2} [$cm^{-3}\cdot s^{-1}$]
A	2.3×10^{16}	3.3×10^{16}	2.1×10^{22}	1.0×10^{-11}	2.0×10^{17}	8.5×10^{-10}	1.0×10^{-8}	6.5×10^{-11}
B	2.5×10^{16}							
*A/B	*0.92							

N.B.: Here '*' indicates the ratio of defect densities N_{t2} for samples A and B.

Table 4. 3 Parameters of rate Eqs. (4.2) and (4.3) for BGE 1.27 eV of samples A and B.

Sample	N_{t2} [cm^{-3}]	N_{t1} [cm^{-3}]	G_1 [$cm^{-3}\cdot s^{-1}$]	B [$cm^{-3}\cdot s^{-1}$]	n_0 [cm^{-3}]	C_{n1} [$cm^{-3}\cdot s^{-1}$]	C_{p1} [$cm^{-3}\cdot s^{-1}$]	C_{p2} [$cm^{-3}\cdot s^{-1}$]
A	2.2×10^{16}	2.2×10^{16}	2.1×10^{22}	1.0×10^{-11}	2.0×10^{17}	8.5×10^{-10}	1.0×10^{-8}	6.5×10^{-11}
B	1.5×10^{16}							
*A/B	*1.5							

N.B.: Here '*' indicates the ratio of defect densities N_{t2} for samples A and B.

It is evident from Table 4.2 that the defect densities observed by the 1.46 eV BGE energy for samples A and B at NRR level-1 are similar. At NRR level-2 they are nearly similar, and the ratio of the defect densities for both samples is around 0.92, which is very near unity considering the experimental accuracy. For the second-most dominant BGE energy of 1.27 eV (Table 4.3), the ratio of defect density at NRR level-1 is also similar across samples; however, at NRR level-2, the defect density for sample A is around 1.5 times higher than that of sample B.

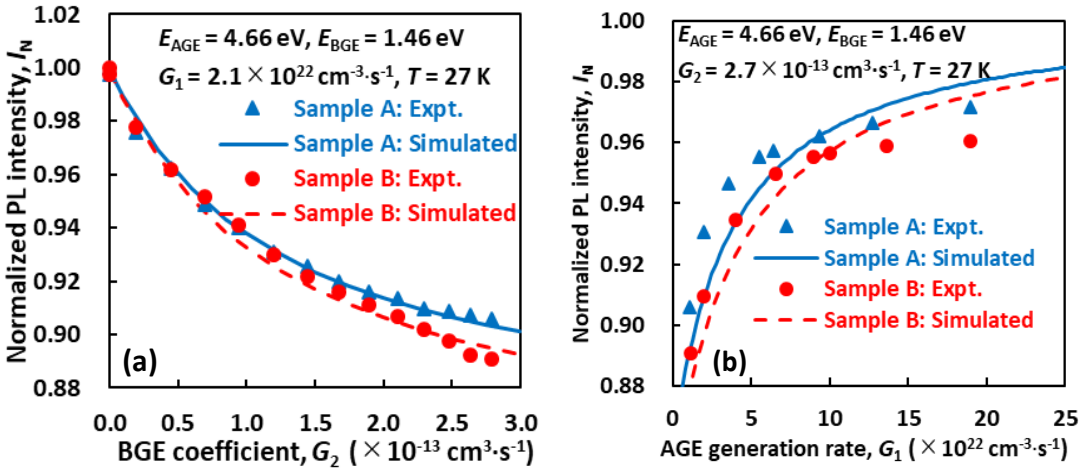

Fig. 4. 8 Variation of I_N as a function of (a) BGE coefficient G_2, and (b) AGE generation rate G_1 for the BGE energy of 1.46 eV at 27 K. The solid (Blue) and broken (Red) lines represent the simulated results of sample A and B, respectively. Here "Expt." indicates the experimental results.

Figure 4.8(a) shows the variation of normalized PL intensity I_N as a function of the BGE coefficient (G_2) of the 1.46 eV BGE at 27 K under a fixed AGE generation rate of 2.1×10^{22} cm^{-3}·s^{-1}. The solid (blue) and broken (red) lines represent the simulated result along with the experimental values for both samples. The simulated I_N values exhibit a reasonable agreement with the experimental data. The influence of normalized PL intensity as a function of the electron–hole generation rate of the AGE (G_1) at 27 K are calculated by setting $G_2 = 2.7\times10^{-13}$ cm^3·s^{-1} for the 1.46 eV BGE and keeping all other parameters as in previous calculations. These results are depicted in Fig. 4.8(b). Here, a set of parameters give behavioural insight into below-gap states acting as NRR centers in samples A and B, and there is a reasonable fitting with experimental data. The effect of I_N values as a function of G_2 and G_1 for the second-most dominant BGE energy of 1.27 eV at 20 K under a fixed AGE generation rate, $G_1 = 2.1\times10^{22}$ cm^{-3}·s^{-1} and BGE coefficient $G_2 = 6\times10^{-13}$ cm^3·s^{-1}, respectively; these are shown in figures 4.9(a) and 4.9(b).

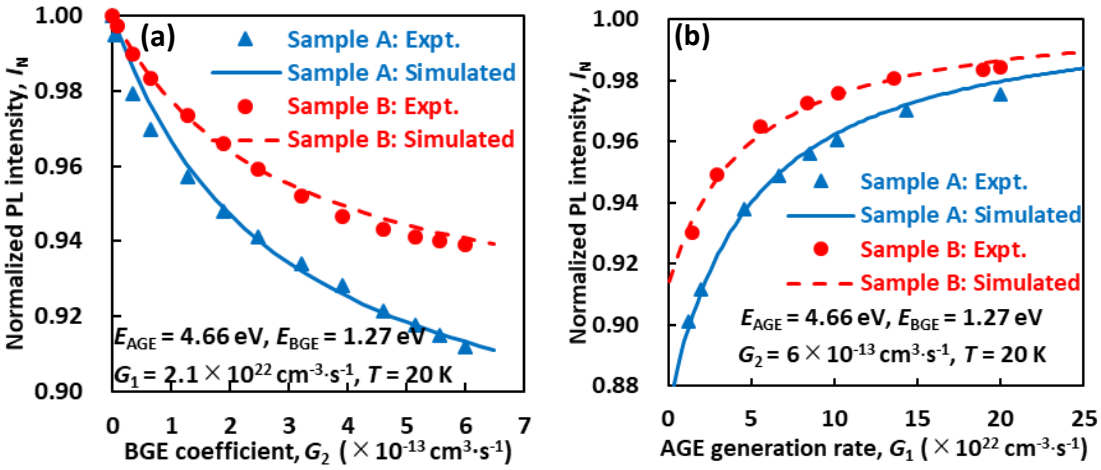

Fig. 4. 9 Effect of I_N values as a function of (a) BGE coefficient G_2, and (b) AGE generation rate G_1 for 1.27 eV BGE at 20 K. The solid (Blue) and broken (Red) lines represent the simulated results of sample A and B, respectively. Here "Expt." indicates the experimental results.

Although this set of parameters shows a reasonable fit with both the AGE and the BGE photon number density dependence, the possibility of another set of parameters should not be ruled out. However, it is clear that the two-level model is valid for interpreting our experimental results. Additionally, the density ratio of 1.5 for the second-most dominant BGE energy of 1.27 eV gives us a reason for the difference in PL intensities between samples A and B. In our case, all the TWEPL measurements were between 20 K and 29 K (Figs. 4.5 and 4.7). As shown in Fig. 4.4(a), the integrated PL intensity of both samples did not vary much in the temperature range of 20 K to 30 K. Therefore, we can assume that the normalized PL intensity I_N values were almost the same in the aforementioned temperature range for each of the BGE energies. Moreover, the average temperature was about 25 K for TWEPL measurements. Our estimated result shows that the densities of NRR centers corresponding to the 0.93 eV, 1.17 eV, and 1.27 eV BGE energies are lower in sample B than in sample A, which determines the PL efficiency of the samples. A different density of NRR centers results directly from only a 40 °C difference in growth temperature and indirectly from a change in Al composition. From all the fitting results, it is concluded that the interpretation based on the two-level model is valid and that the use of a high-temperature growth condition is more effective in reducing the density of NRR centers than a low-temperature growth condition in this case. The TWEPL study of NRR centers guides us to further optimize growth conditions.

4.4 Conclusions

Defect states acting as NRR centers in two AlGaN MQW samples grown at two different temperatures, 1140 °C (sample A) and 1180 °C (sample B), were studied by TWEPL at a temperature of about 25 K. We detected NRR centers by adding BGE light with photon energies between 0.93 eV and 1.46 eV, which helped us determine the energy distribution of the NRR centers. All the BGE energies decreased PL intensity, and the most distinct quenching was observed for the BGE energy of 1.46 eV at the same BGE photon number density. Since the quenching by the 1.46 eV BGE did not show enough of a difference between the two samples, we considered the experimental results of BGE and AGE density dependence with the second-most dominant BGE energy (1.27 eV) in order to interpret the difference in PL efficiency. By a qualitative simulation with a two-level model, the density ratio of the NRR level-2 for samples A and B was 1.5 for the 1.27 eV BGE. We attributed the lower PL intensity of sample A to higher densities of NRR centers corresponding to the BGE energies of 0.93 eV, 1.17 eV, and 1.27 eV. Behavior and distribution of NRR centers depend on detailed growth conditions and the structure of samples. It is essential to quantitatively study defect levels and comprehensively trace their origins.

CHAPTER 05

SUPERLATTICE PERIOD DEPENDENCE ON NONRADIATIVE RECOMBINATION CENTERS OF UV-B AlGaN QW STRUCTURE

5.1 Introduction

Recently, the demand of cheap, environmentally friendly, and smart AlGaN ultraviolet (UV) light emitters in the UV-B spectral range between 280 nm and 320 nm has arisen because of their legionary potential applications [3,10,15–20]. The conventional light sources in the aforesaid spectral ranges are bulky, have limited lifetime, and contain toxic substances [110]. Therefore, UV-B LEDs are promising devices, but their reliability still needs improvement [111]. One of the main reasons for the low efficiency of UV-B LEDs is the non-radiative recombination (NRR) losses [Shockley–Read–Hall (SRH) and Auger-related] [110]. Recent studies have indicated that the reduction in optical power with an increase in the temperature (thermal droop) may also limit the performance of GaN-based LEDs, which results in an emission decrease comparable to the efficiency droop [112,113]. Therefore, a suitable growth condition along with the growth technique is essential in reducing the NRR losses and improving the efficiency of UV-B LED structures.

There is much research in the recent years to improve the external quantum efficiency of the AlGaN-based UV-B light-emitting materials, [3,114] and it is still crucial to find the optimum growth conditions. The lack of lattice-matched, cost-effective, and suitable substrates brings difficulties in reducing the density of defect states, which act as NRR centers in multiple quantum wells (MQWs) [3,23–25]. In order to improve

the efficiency of light-emitting materials, it is indispensable to reduce such NRR centers. Moreover, the use of a superlattice (SL) structure with a suitable number of periods between the AlN buffer layer and the *n*-AlGaN layer is effective to suppress the defect densities [115]. Onuma *et al*. [88] and Nepal *et al*. [89] have used photoluminescence (PL) spectroscopy and cathodoluminescence (CL) spectroscopy to investigate below-gap states in AlGaN, showing only characteristic luminescence peaks and giving relative information about NRR centers. Deep-level transient spectroscopy (DLTS) and deep-level optical spectroscopy (DLOS) have been used by other groups to investigate deep-level defects in AlGaN films, but their applications are confined due to the necessity of preparing suitable samples for the measurement with Schottky contacts or an appropriate p-n junction [90–92].

Our main focus in this chapter is to analyze the role of the number of superlattice periods (SLPs) in the SL structure on *n*-AlGaN layer and QW layer separately and their combined effect of UV-B AlGaN samples grown on c-plane sapphire substrates. Here, we used a two-wavelength excited PL (TWEPL) technique for the detection and characterization of NRR centers optically [58,64]. It is a versatile non-contacting and non-destructive scheme; there is no need for any special kind of sample preparation. The variation of PL intensities with temperature, peak PL intensity changes due to the addition of the below-gap excitation (BGE) light over that of the above-gap excitation (AGE), is also observed as functions of the AGE photon number density and BGE photon number density. By systematically solving the rate equations based on the recombination model and fitting the results with experimental data, the relative contribution of NRR parameters are also evaluated.

5.2 Experimental methods

5.2.1 Sample structure

Figure 5.1 shows the structure of UV-B AlGaN samples, grown on c-plane sapphire substrates by a metalorganic chemical vapor deposition (MOCVD) technique, used in this study. The sample consists of a 4-μm-thick AlN buffer layer, AlN/$Al_{0.4}Ga_{0.6}N$ superlattice (SL) buffer layer with period lengths of 6.5 nm, a 1-μm-thick Si-doped AlGaN layer, followed by a 3-periods MQW consisting of 2.6-nm-thick wells and 9-nm-thick barrier layers, and a 10-nm-thick $Al_{0.4}Ga_{0.6}N$ cap layer. The composition of the well/barrier layer is $Al_{0.15}Ga_{0.85}N/Al_{0.4}Ga_{0.6}N$. The number of SLP ranges from 50 to 200.

Trimethylaluminum (TMA), trimethylgallium (TMG), and ammonia (NH3) were used as precursors for AlGaN growth. Tetraethylsilane (TESi) precursor was used for the *n*-type doping source. The reactor pressure and growth temperature were maintained at 10 kPa and 1150 °C for the entire growth process. Here, we have studied four samples under the same growth conditions, except for the number of SLP. The number of SLP of samples A(SLP-50), B(SLP-100), C(SLP-150), and D(SLP-200) is 50, 100, 150, and 200, respectively.

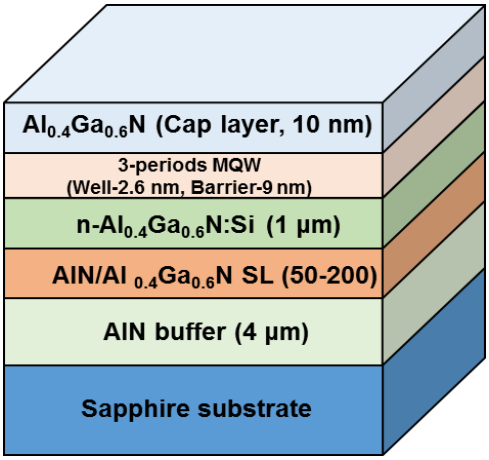

Fig. 5. 1 Samples structure.

Reciprocal lattice mapping, relaxation ratio, and full width at half maximum (FWHM) of samples A(SLP-50), B(SLP-100), C(SLP-150), and D(SLP-200) are shown in Fig. 5.2. The relaxation of *n*-AlGaN lattice is almost same in samples A(SLP-50) and B(SLP-100) [Figs. 5.2(a), 5.2(b), and 5.2(e)], while that in sample D(SLP-200) [Fig. 5.2(d)] is reduced with the increase in the number of SLP. A compositional splitting of x = 0.37 and 0.42 is observed in sample C(SLP-150) [Figs. 5.2(c) and 5.2(e)]. This relaxation behavior affects the formation of NRR centers. As there is a spread of reciprocal lattice points with relaxation in samples with SLP 100 or less [Figs. 5.2(a) and 5.2(b)], it is not a value reflecting dislocation density as it is. Since the relaxation ratios of samples, A(SLP-50) and B(SLP-100) are almost same, it is expected that the dislocation density is lower in sample B(SLP-100) due to its lower FWHM value.

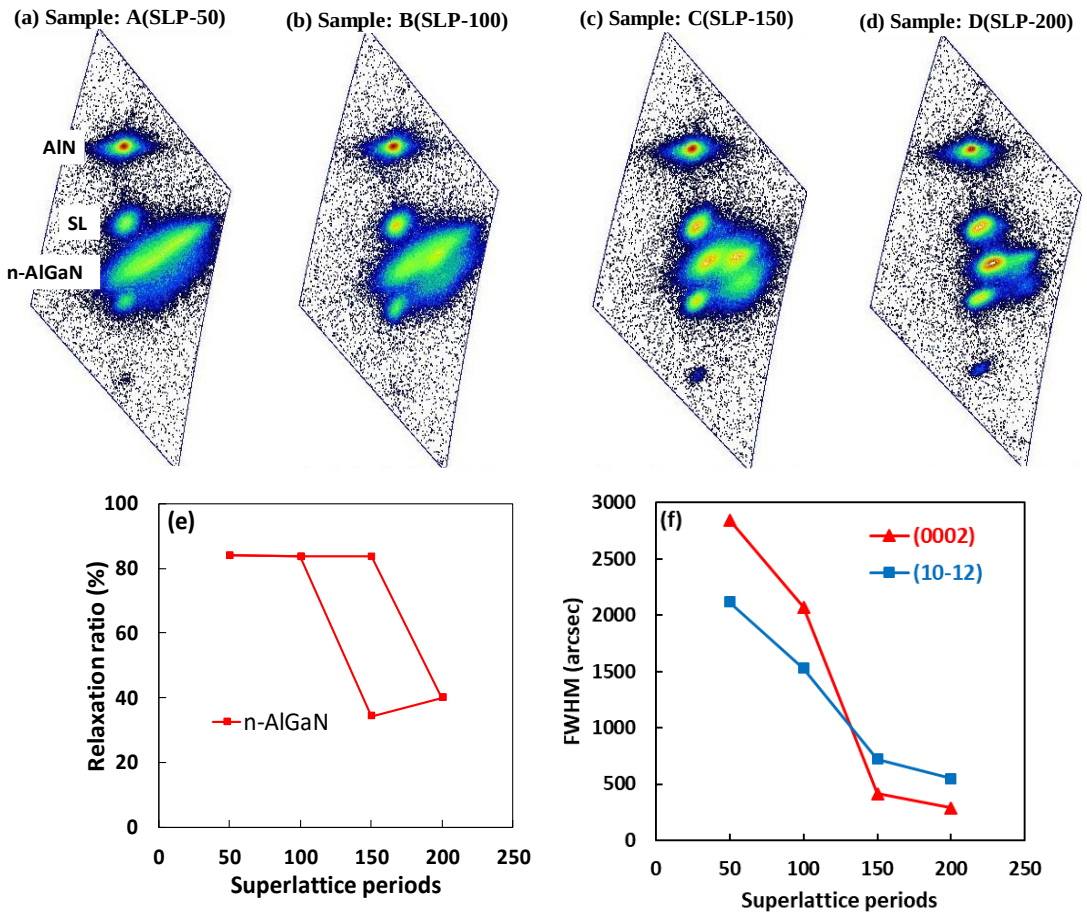

Fig. 5. 2 $(\bar{1}\bar{1}4)$ reciprocal lattice mapping of samples (a) A(SLP-50), (b) B(SLP-100), (c) C(SLP-150), and (d) D(SLP-200). The relaxation ratio and FWHM of these samples as a function of superlattice periods are also shown in (e) and (f), respectively.

5.2.2 Measurement

The experimental setup for characterizing the *n*-AlGaN and QW layers of UV-B AlGaN samples by a two-wavelength excited photoluminescence (TWEPL) method is shown in Fig. 5.3. The sample was mounted on a Cu holder with the sapphire side up inside a temperature-controlled cryostat with three optical windows. A continuous wave (CW) diode pumped solid state laser (model: SDL-266-005T) of wavelength 266 nm ($h\nu_{AGE}$ = 4.66 eV) serves as the above-gap excitation (AGE) light ($h\nu_{AGE} > E_g$), where E_g denotes the energy bandgap of the layer, for the conventional PL measurements. By adding an intermittent below-gap excitation (BGE) light ($h\nu_{BGE} < E_g$) on the AGE light at the same point of the sample surface and observing the intensity change of PL spectra with and without the BGE light, $I_{(AGE+BGE)}$ and $I_{(AGE)}$, respectively, the normalized PL intensity (I_N) is calculated as $I_N = I_{(AGE+BGE)}/I_{(AGE)}$ in the TWEPL measurement. Its

deviation from unity implies the presence of NRR centers in between the energy bandgap of the samples [58,64]. The BGE light sources with energies 0.93 eV (1340 nm wavelength), 1.17 eV (1064 nm), 1.27 eV (980 nm), and 1.46 eV (852 nm) are used in the experiment. The detailed experimental layout and models of NRR centers can be found elsewhere [64,74,93].

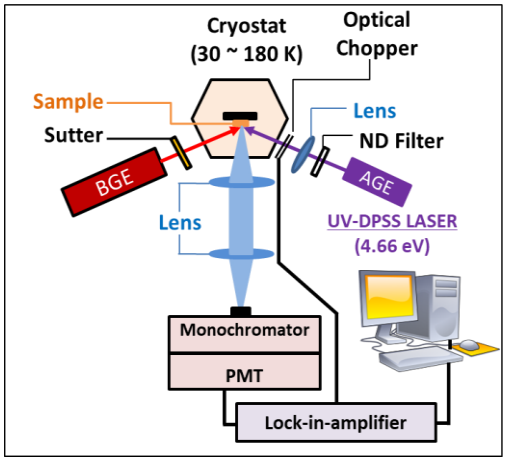

Fig. 5. 3 Experimental setup for TWEPL measurements.

5.3 Results and discussion

5.3.1 Conventional PL measurement

Conventional PL spectra were measured by an excitation source of photon energy 4.66 eV with a fixed excitation power density and temperature 1.03 mW·mm^{-2} and 30 K, respectively for four samples of A(SLP-50), B(SLP-100), C(SLP-150), and D(SLP-200), as shown in Fig. 5.4. Several spectral features can be noticed including three peaks showing the highest PL efficiency by the sample B(SLP-100) in all peaks. The peak observed at around 280 nm, which is estimated from the superlattice (SL) layer, the second and third peaks are observed for the emission from *n*-AlGaN and quantum well (QW) layers, respectively. Complex (multi-band) emission spectra from UV devices have already been reported in the past [82,110,116–118].

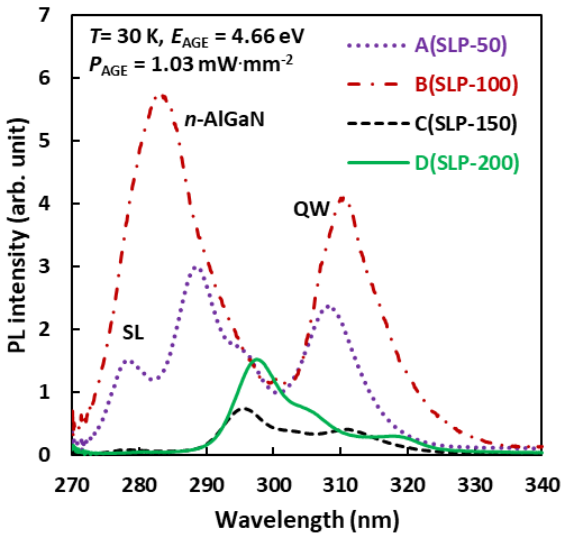

Fig. 5. 4 Comparison of PL intensities among samples A(SLP-50), B(SLP-100), C(SLP-150), and D(SLP-200) at 30 K.

With the increase in temperature from 30 K, the PL intensity decreased and an anomalous temperature-dependent emission behavior of the peak wavelength is observed for all samples as shown in Fig. 5.5.

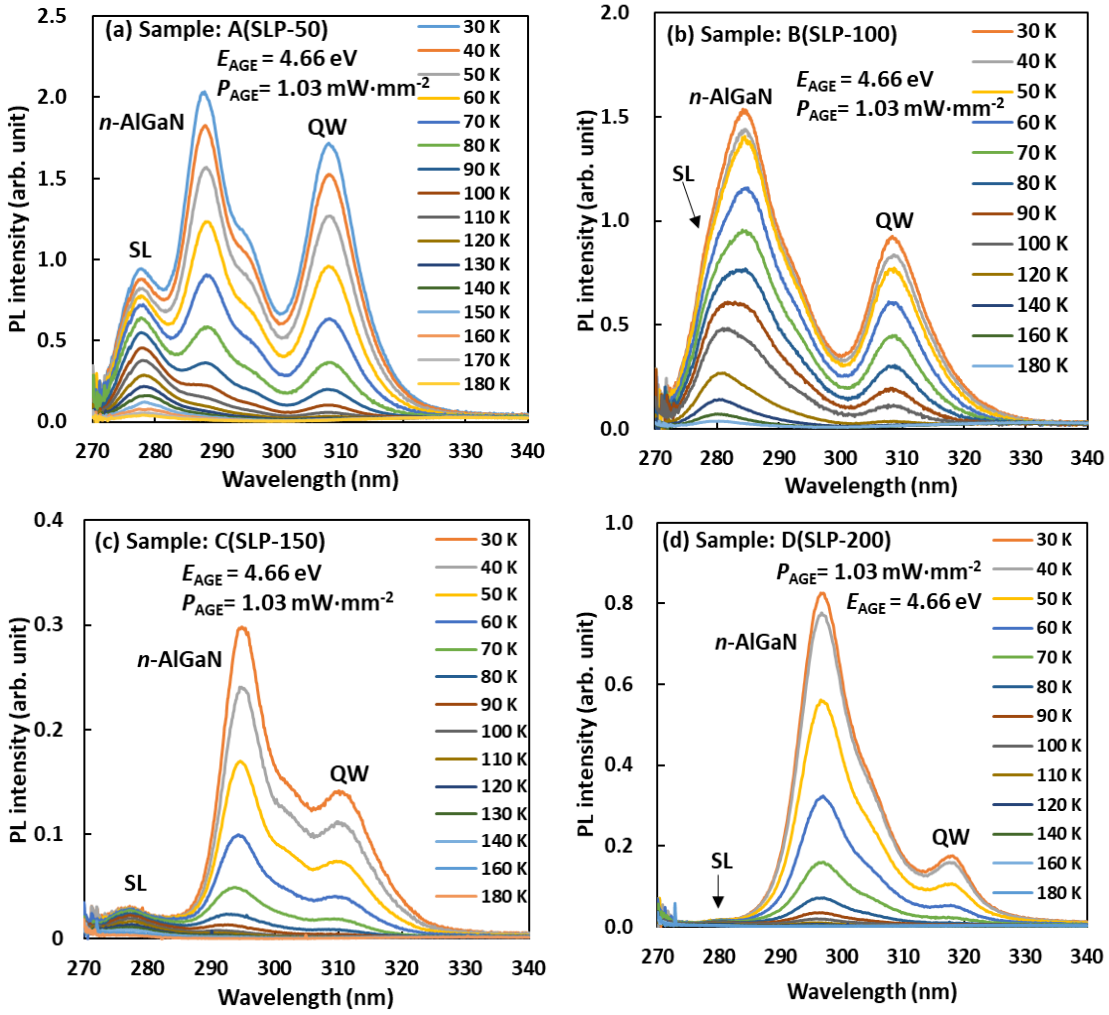

Fig. 5. 5 Temperature dependent PL intensities for samples (a) A(SLP-50), (b) B(SLP-100), (c) C(SLP-150), and (d) D(SLP-200) for a fixed excitation energy of 4.66 eV and an excitation power density of 1.03 mW mm^{-2}.

The temperature-dependent integrated PL intensity (normalized) of UV-B AlGaN samples is shown in Fig. 5.6(a). With temperature increasing from 30 K, the integrated PL intensity decreases drastically for sample D(SLP-200) up to 80 K, for sample C(SLP-150) up to 90 K, for sample A(SLP-50) up to 100 K, and for sample B(SLP-100) up to 120 K. With a further increase in temperature, a monotonically decreasing tendency of integrated PL intensity is observed for all the samples up to 180 K. It is observed, from Fig. 5.6(a), that the normalized integrated PL intensity is higher for sample B(SLP-100) over the entire temperature region, whereas samples C(SLP-150) and D(SLP-200) show higher thermal quenching at low- and high-temperature regions, respectively. The thermal quenching behavior is determined by the activation of NRR centers and the

escape of carriers from QWs [96,97]. The latter mechanism is negligible under this low-excitation condition.

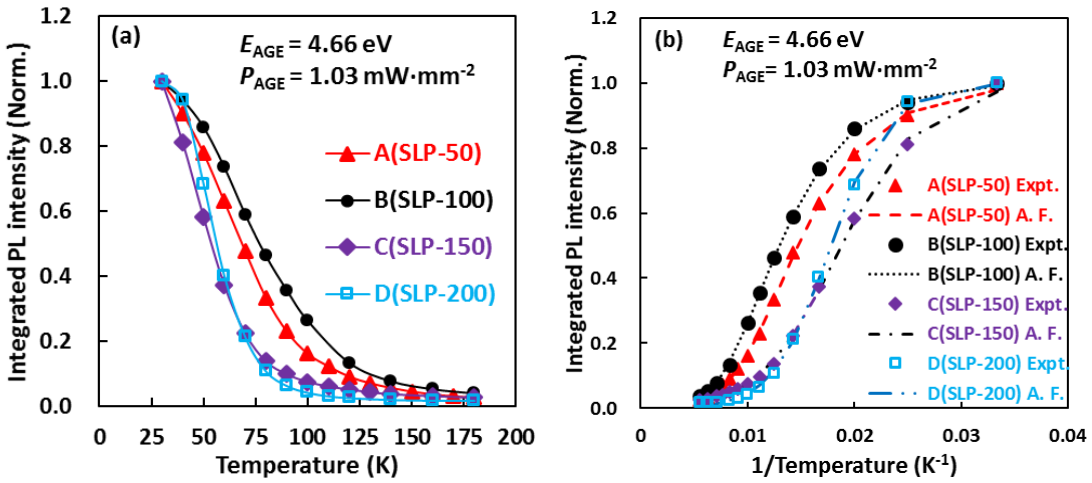

Fig. 5. 6 Comparison of integrated PL intensities (normalized) among samples A(SLP-50), B(SLP-100), C(SLP-150), and D(SLP-200) as a function of (a) temperature and (b) inverse temperature. The solid lines shown in (a) are only to guide the eyes. The corresponding Arrhenius fitting (A. F.) is depicted in (b). Here, "Expt." indicates the experimental results.

To know the thermal activation energies, we calculated the integrated PL intensity as a function of inverse temperature, as shown in Fig. 5.6(b), and fitted well by using the following two-channel Arrhenius formula [96–100]:

$$I(T) = \frac{1}{\left[1 + C_1.\exp\left(\frac{-E_1}{K_B T}\right) + C_2.\exp\left(\frac{-E_2}{K_B T}\right)\right]}, \qquad (5.1)$$

which suggests that more than one nonradiative pathway exists and acts together with the main NRR channel [119], where $I(T)$ is the temperature-dependent normalized integrated PL intensity. C_1 and C_2 are the two constants related to the density of NRR centers in the samples. E_1 and E_2 stand for the thermal activation energies at low- and high-temperature ranges corresponding to the NRR process [97,100] and k_B is Boltzmann's constant. The origin of one of these nonradiative channels could be partially related to the overflow of carriers out of the confining potential [119]. It is expected that by increasing the depth of QW, this nonradiative pathway will become less significant. All the values of the parameters in Eq. (1) are shown in Table 5.1.

Table 5. 1 Fitting parameters obtained from Eq. (1).

Sample	C_1	E_1 (meV)	C_2	E_2 (meV)
A(SLP-50)	11.9	16.5	597.9	44.9
B(SLP-100)	15.6	19.6	985.1	57.5
C(SLP-150)	67.4	20.3	261.1	33.1
D(SLP-200)	494.7	30.7	1014.1	43.2

It is evident from Table 5.1 that the maximum value of E_2 (57.5 meV) is observed for sample B(SLP-100) in a higher temperature region, which implies that sample B(SLP-100) has a lower temperature effect. The lower temperature effect indicates the lower defect density, which is consistent with our expected results shown in Figs. 5.2 and 5.4. The saturation of the NRR centers and the carrier-screening effect lead to a comparatively higher rate constant C_2 under the higher temperature region [96].

5.3.2 TWEPL Measurement

In order to know the distribution of NRR centers in the *n*-AlGaN and QW layers of UV-B AlGaN samples, the normalized PL intensity (I_N) for both the *n*-AlGaN emission and QW emission were measured as a function of the BGE photon number density for four BGE energies as 0.93 eV, 1.17 eV, 1.27 eV, and 1.46 eV, respectively, as shown in Figs. 5.7 and 5.8. The AGE power density and the temperature were fixed at 1.03 mW mm^{-2} and 30 K, respectively. With the addition of BGE light on the AGE, the values of I_N decreased from unity for both *n*-AlGaN and QW emission for all BGE energies. It is observed from Figs. 5.7 and 5.8 that the amount of PL quenching becomes pronounced with increasing BGE photon number density. The most dominant quenching occurred by the 1.27 eV BGE energy at the same BGE photon number density (1.3×10^{19} $cm^{-2}\cdot s^{-1}$) for the *n*-AlGaN emission (Fig. 5.7) for samples A(SLP-50), B(SLP-100), and C(SLP-150). For sample D(SLP-200), the most dominant quenching was observed by the 1.46 eV BGE energy at that BGE photon number density value for the *n*-AlGaN emission. For the QW emission, the most dominant quenching of I_N occurred by the 1.27 eV BGE energy at the same BGE photon number density for all samples (Fig. 5.8).

The degree of quenching of I_N from unity represents the density of NRR centers in that layer of the samples. Thus, this result implies that the densities of NRR centers in the *n*-AlGaN layer corresponding to the 1.27 eV BGE energy, at the same BGE photon

number density, are higher for all the samples except D(SLP-200). In the QW layer, the densities of NRR centers corresponding to the 1.27 eV BGE energy, at the same BGE photon number density, are higher for all the samples.

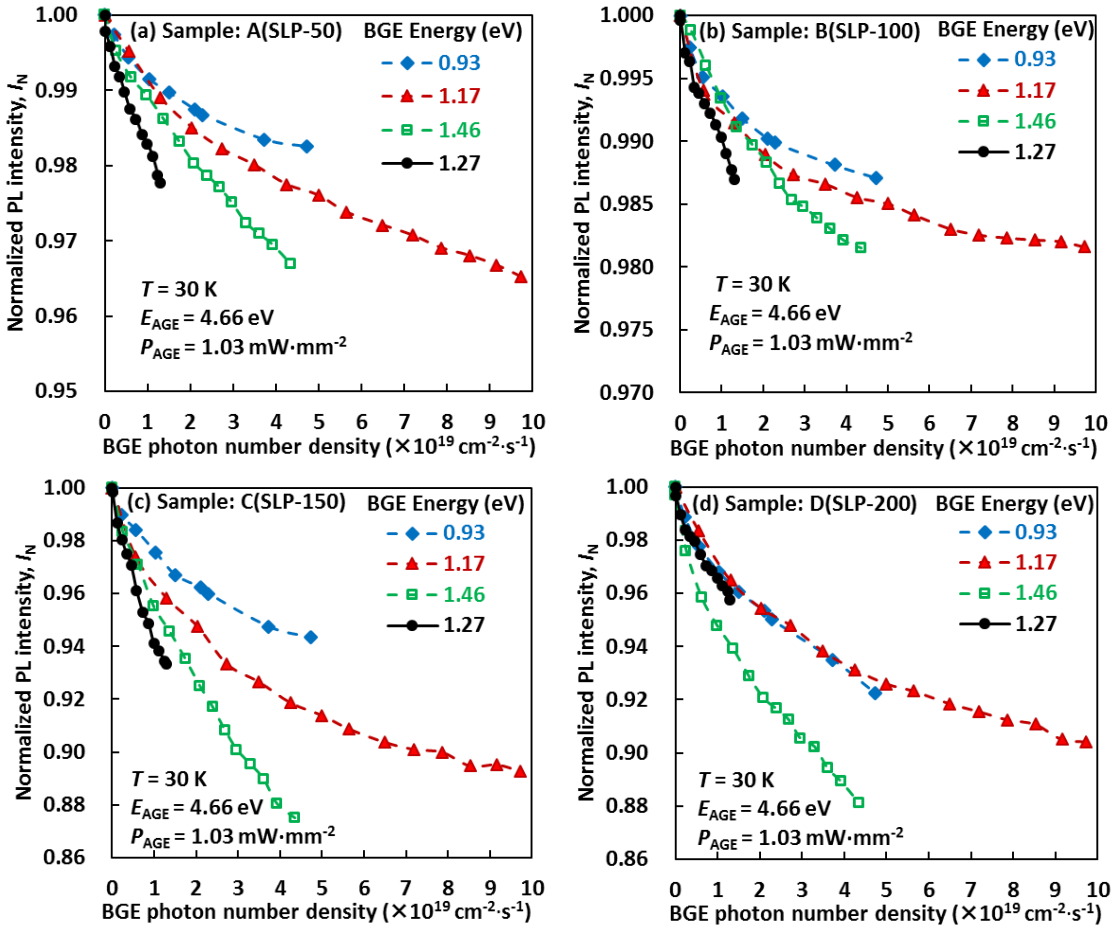

Fig. 5. 7 Variation of I_N values of *n*-AlGaN layer emission as a function of BGE photon number density for samples (a) A(SLP-50), (b) B(SLP-100), (c) C(SLP-150), and (d) D(SLP-200) at 30 K.

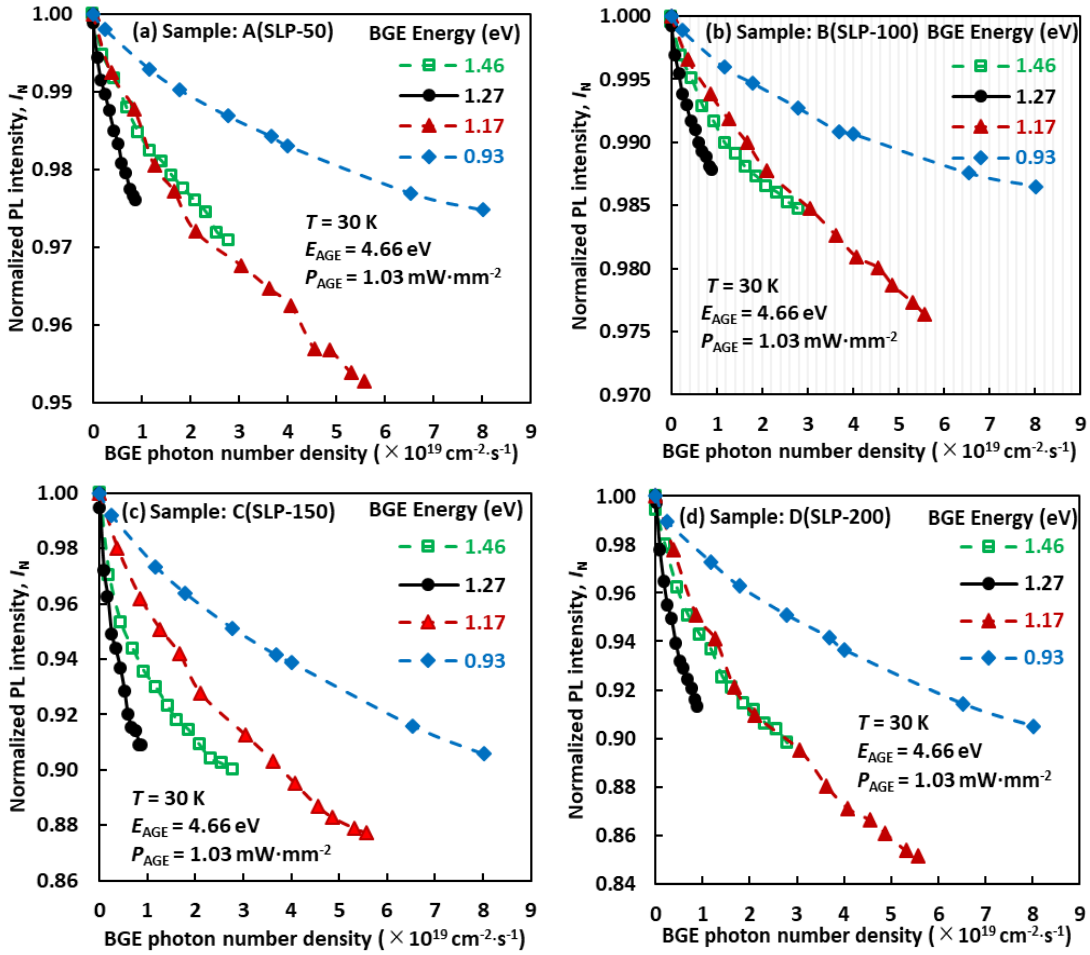

Fig. 5. 8 Variation of I_N values of QW layer emission as a function of BGE photon number density for samples (a) A(SLP-50), (b) B(SLP-100), (c) C(SLP-150), and (d) D(SLP-200) at 30 K.

To compare the decrement of I_N values for the emission from *n*-AlGaN layer and QW layer for all samples, the results of Figs. 5.7 and 5.8 are rearranged in terms of each BGE energy, as shown in Figs. 5.9 and 5.10, respectively.

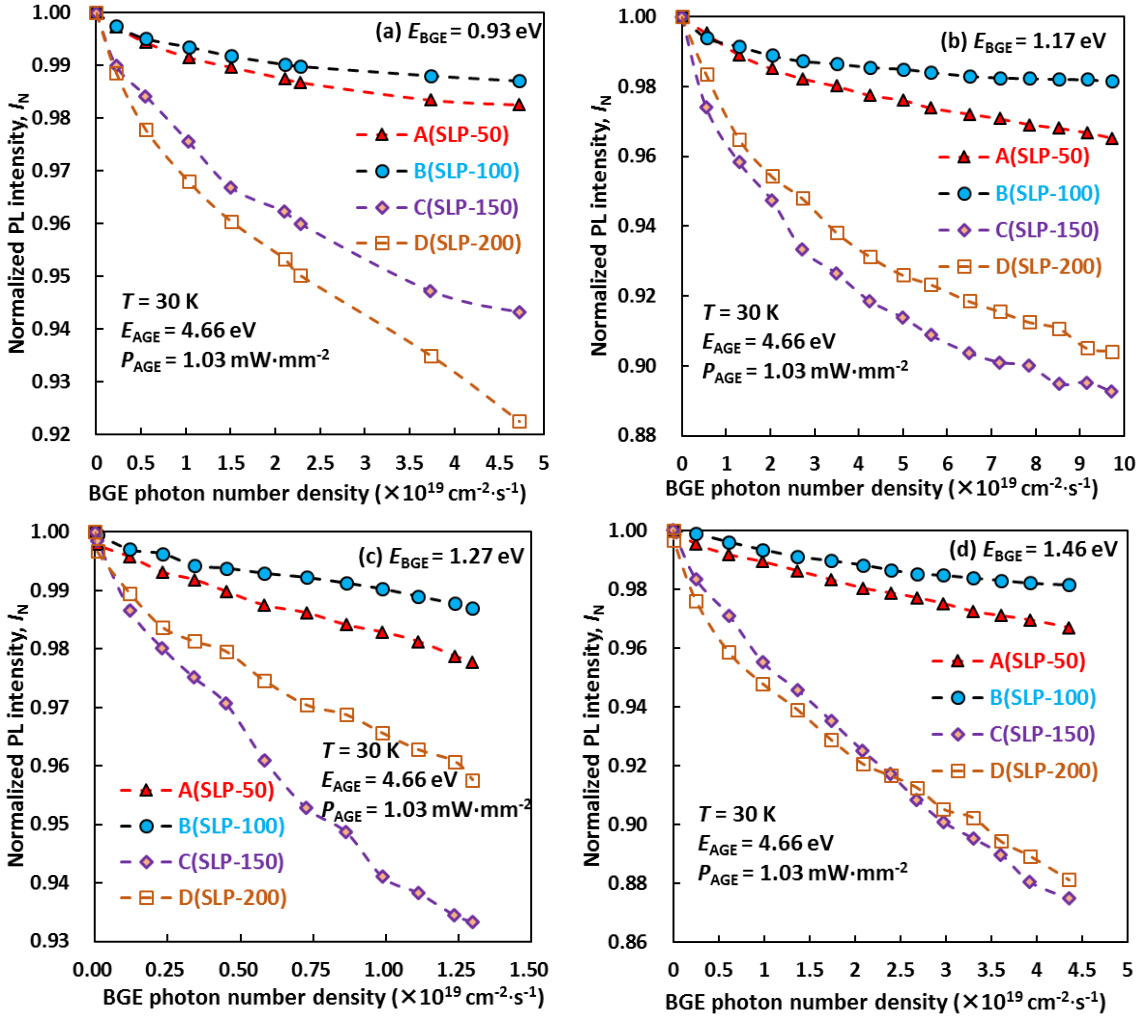

Fig. 5. 9 Variation of I_N values for *n*-AlGaN layer emission as a function of BGE photon number density for the BGE energies of (a) 0.93 eV, (b) 1.17 eV, (c) 1.27 eV, and (d) 1.46 eV for all samples at 30 K.

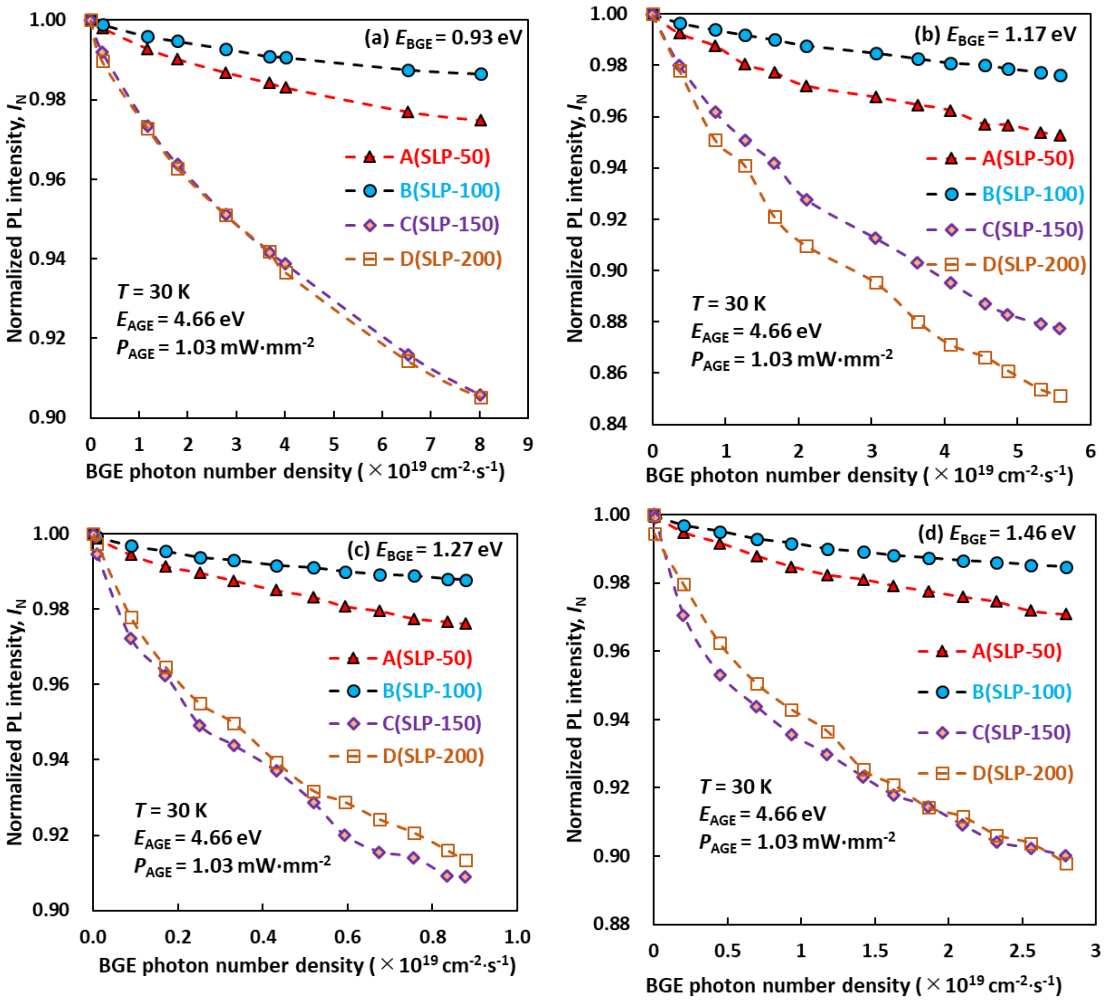

Fig. 5. 10 Variation of I_N values of QW layer emission as a function of BGE photon number density for the BGE energies of (a) 0.93 eV, (b) 1.17 eV, (c) 1.27 eV, and (d) 1.46 eV for all samples at 30 K.

It is obvious from Figs. 5.9 and 5.10 that the sample B(SLP-100) shows the lowest quenching of I_N values, irrespective of all BGE energies and entire BGE photon number density. This implies that the sample B(SLP-100) contains the lowest defect densities in both the layers when compared to other samples. This is consistent with the results shown in Figs. 5.4 and 5.6, and with our expected results shown in Fig. 5.2. In *n*-AlGaN emission for the BGE energies of 1.17 eV [Fig. 5.9(b)] and 1.27 eV [Fig. 5.9(c)], sample C(SLP-150) shows the maximum quenching of I_N values, whereas sample D(SLP-200) exhibits a higher quenching for 0.93 eV BGE energy [Fig. 5.9(a)]. For a BGE energy of 1.46 eV [Fig. 5.9(d)], sample D(SLP-200) presents maximum decrement of I_N values at lower BGE photon number densities; in contrast, for a higher BGE photon number density region, sample C(SLP-150) reproduces the lowest I_N values for *n*-AlGaN emission. In

QW emission for the BGE energies of 1.27 eV [Fig. 5.10(c)] and 1.46 eV [Fig. 5.10(d)], sample C(SLP-150) shows the maximum quenching of I_N values, whereas sample D(SLP-200) exhibits a higher quenching for the BGE energy of 1.17 eV [Fig. 5.10(b)]. For a 0.93 eV BGE energy [Fig. 5.10(a)], samples C(SLP-150) and D(SLP-200) present almost the same decrement of I_N values over the entire BGE photon number density region in QW emission.

The diminution of I_N values at 30 K, shown in Figs. 5.7 to 5.10, is explained by the two-level recombination model schematically depicted in Fig. 5.11. The figure shows the presence of a pair of NRR centers in the layer (*n*-AlGaN or QW) whose energy difference corresponds to that of the BGE energies [53,64,73,101]. Here, G_1 ($cm^{-3}\cdot s^{-1}$) is the generation rate of AGE, G_2 ($cm^3\cdot s^{-1}$) is the BGE coefficient, B ($cm^3\cdot s^{-1}$) is the radiative recombination coefficient, C_n and C_p are the electron and hole capture coefficients, respectively, N_t is the density of NRR levels, and f_{t1} and f_{t2} are the electronic occupation functions of NRR level-1 and NRR level-2, respectively. The NRR parameters can be found by fitting experimental results based on Shockley–Read–Hall statistics [64,102].

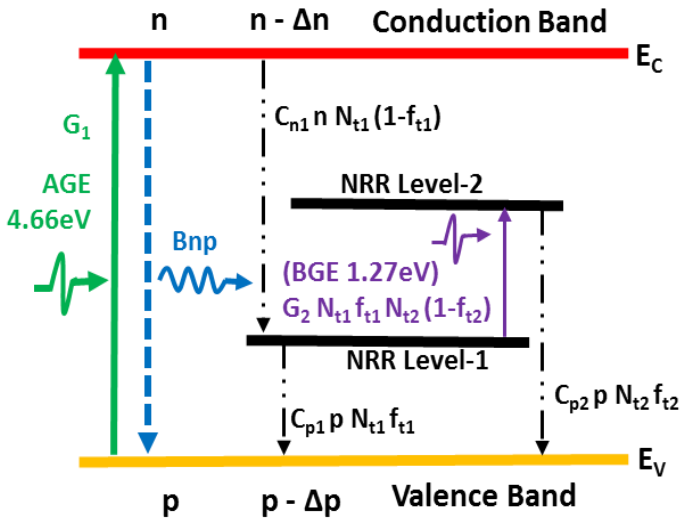

Fig. 5. 11 Two-level model of NRR process, which explains the PL intensity quenching due to the irradiation of BGE.

When the BGE energy matches the energy difference between two coexisting below-gap NRR levels, level-1 and level-2 (Fig. 5.11), electrons in NRR level-1 are excited to NRR level-2, from which they recombine nonradiatively with holes in the valence band of *n*-AlGaN or QW. Consequently, a number of electron deficiencies occur

in level-1, which allows for an increase in NRR from the conduction band. The combination of both effects reduces the number of electron-hole pairs available for radiative recombination and results in the PL intensity quenching. In the low-BGE photon number density region, the electron occupation function of NRR level-2 remains much lower than unity, and the PL quenching avails with the increase in the BGE photon number density. Moreover, with a further increase in the BGE photon number density, the electron occupation function of NRR level-2 approaches unity, and the slope of PL quenching becomes gentle; this is partly shown in Figs. 5.7 to 5.10.

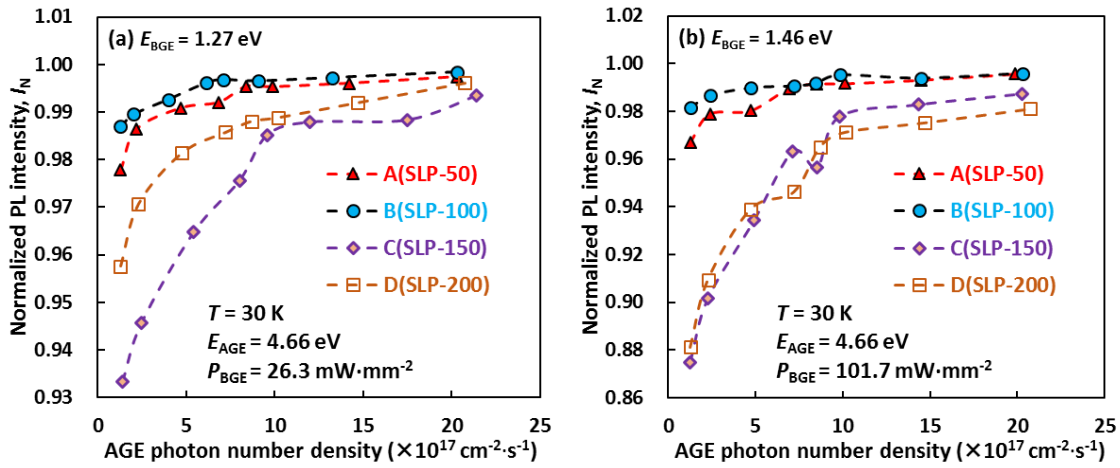

Fig. 5. 12 Effect of I_N values of *n*-AlGaN layer emission as a function of AGE photon number density for the most dominant and second-most dominant BGE energies of (a) 1.27 eV and (b) 1.46 eV for all samples at 30 K.

Figure 5.12 shows the effect of I_N values of *n*-AlGaN emission as a function of AGE photon number density for the most dominant and second-most dominant BGE energy of 1.27 eV [Fig. 5.12(a)] and 1.46 eV [Fig. 5.12(b)] at 30 K. With an increase in the AGE photon number density, the value of I_N first increases and then approaches unity. The excitation of electrons from NRR level-1 to level-2 (Fig. 5.11), due to the BGE, increases the NRR rate from level-1 and level-2 to the valence band at a lower AGE photon number density. With an increase in the AGE photon number density, band-to-band radiative recombination becomes stronger since the rate is proportional to *n* times *p*. Consequently, the normalized PL intensity I_N approaches unity. A similar tendency was observed in our previous studies of TWEPL [73,103,120]. It is observed from Fig. 5.12 that the I_N values is also higher for sample B(SLP-100) over the entire AGE photon number density region

in both energy cases. These results are also consistent with the results shown in Figs. 5.6, 5.7 and 5.9.

5.3.3 Rate Equation Analysis

In order to corroborate our qualitative interpretations, for the results of *n*-AlGaN layer emission shown in Figs. 5.7, 5.9, and 5.12 by the two-level model, a semiquantitative simulation of the TWEPL results was carried out for the most dominant PL quenching occurred by the 1.27 eV BGE energy. The rate equations for the two-level model (Fig. 5.11) can be written [51,52,64] as:

$$\left.\begin{aligned}
\frac{dn}{dt} &= G_1 - Bnp - C_{n1} n N_{t1}(1 - f_{t1}) = 0, \\
\frac{dp}{dt} &= G_1 - Bnp - C_{p1} p N_{t1} f_{t1} - C_{p2} p N_{t2} f_{t2} = 0, \\
\frac{df_{t1}}{dt} &= C_{n1} n(1 - f_{t1}) - C_{p1} p f_{t1} - G_2 f_{t1} N_{t2}(1 - f_{t2}) = 0, \\
\frac{df_{t2}}{dt} &= G_2 N_{t1} f_{t1}(1 - f_{t2}) - C_{p2} p f_{t2} = 0,
\end{aligned}\right\} \qquad (5.2)$$

while considering the charge neutrality condition (CNC)

$$n + N_{t1} f_{t1} + N_{t2} f_{t2} = n_0 + p, \qquad (5.3)$$

where n_0 is the density of free electrons in the *n*-$Al_{0.4}Ga_{0.6}N$ layer and its value is known (1.0×10^{19} cm^{-3}) from the sample growers. The radiative recombination coefficient B is considered as 1.0×10^{-11} $cm^3\cdot s^{-1}$ for the AlGaN material [102,107–109,120]. The generation rate of the AGE ($G_1 = 3.5\times10^{22} cm^{-3}\cdot s^{-1}$) is calculated experimentally by using the following equation [104,105,120]:

$$G_1 = P_{laser}(1-R)\alpha \Big/ \left(A_{spot} h\nu\right), \qquad (5.4)$$

where P_{laser} is the excitation power, R (18%) is the Fresnel reflection at the sample surface, A_{spot} is the laser spot size (1.06×10^{-3} cm^2) on the sample surface, $h\nu$ (E_{AGE} = 4.66 eV) is the photon energy of the excitation laser, and α (3.1×10^5 cm^{-1}) [106] is the absorption coefficient of AlGaN at 266 nm (4.66 eV). It is impossible to evaluate the BGE coefficient (G_2) from the absorption coefficient measurement since there is no fundamental absorption for these sources. Here, we used a constant factor for these conversions from the experimental photon number density of the BGE sources [102,120]. The system of rate equations can be solved numerically and the dependencies of n, p, f_{t1}, and f_{t2} on G_2

can be found for the constant parameters of G_1, B and n_0, and the sample's NRR level-1 dependent parameters of C_{n1}, C_{p1} and N_{t1}, and NRR level-2 dependent parameters of C_{p2}, and N_{t2}. The constant parameters are listed in Table 5.2, for convenience.

Table 5. 2 Fixed parameters of rate Eqs. (5.2) and (5.3)

G_1 ($cm^{-3}\cdot s^{-1}$)	B ($cm^{-3}\cdot s^{-1}$)	n_0 (cm^{-3})
3.5×10^{22}	1.0×10^{-11}	1.0×10^{19}

By systematically solving and fitting the result with experimental data (Fig. 5.13), the NRR parameters are obtained for the dominant BGE energy of 1.27 eV for all the samples and are shown in Table 5.3. To estimate and compare the internal quantum efficiencies (IQE) as a function of G_1 (Fig. 5.14) as well as the trap densities N_{t1} of all samples, the NRR level-2 dependent parameters (C_{p2} and N_{t2}) were kept constant and only by varying the NRR level-1 dependent parameters for a reasonable agreement with the experimental data, whereupon the IQE is fully NRR level-1 parameter dependent.

Table 5. 3 Parameters of rate Eqs. (5.2) and (5.3) for 1.27 eV BGE and estimated IQE.

Sample	Level-1 parameter			Level-2 parameter		Ratio of N_{t1} values	IQE (%)
	C_{n1} ($cm^{-3}\cdot s^{-1}$)	C_{p1} ($cm^{-3}\cdot s^{-1}$)	N_{t1} (cm^{-3})	C_{p2} ($cm^{-3}\cdot s^{-1}$)	N_{t2} (cm^{-3})		
A(SLP-50)	4.0×10^{-8}	1.6×10^{-7}	5.4×10^{15}	8.0×10^{-9}	6.0×10^{16}	1.7	10.3
B(SLP-100)	5.0×10^{-8}	2.0×10^{-7}	3.2×10^{15}			1.0	13.5
C(SLP-150)	8.0×10^{-9}	7.0×10^{-8}	2.1×10^{16}			6.5	6.3
D(SLP-200)	3.0×10^{-8}	9.2×10^{-8}	1.1×10^{16}			3.4	8.9

It is evident from Table 5.3 that by keeping NRR level-2 parameters constant, the defect densities N_{t1} at NRR level-1 observed by the 1.27 eV BGE energy for sample C(SLP-150) is maximum (2.1×10^{16} cm^{-3}) and for sample B(SLP-100) is the lowest (3.2×10^{15} cm^{-3}). The ratio of the defect densities for these four samples A(SLP-50):B(SLP-100):C(SLP-150):D(SLP-200) is around 1.7:1.0:6.5:3.4, respectively.

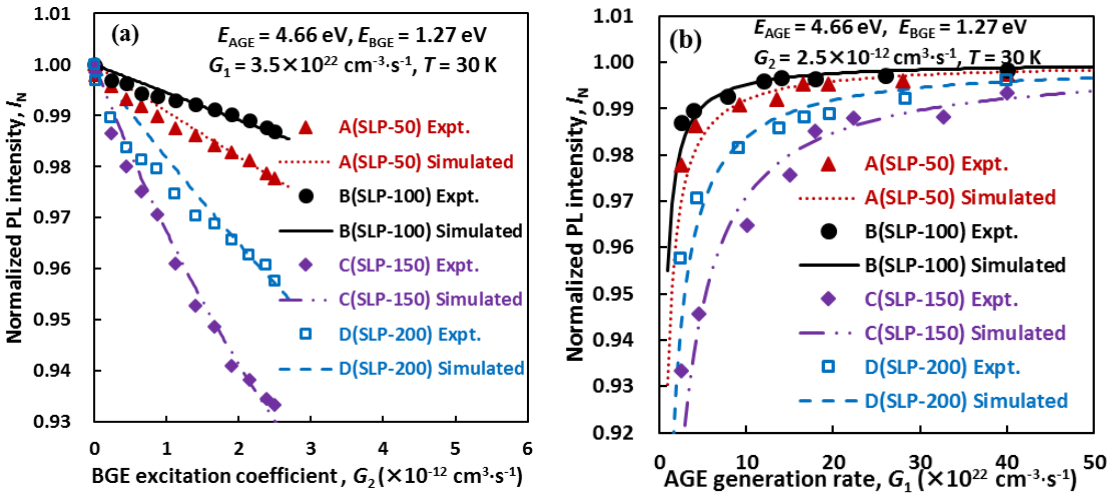

Fig. 5. 13 Variation of I_N values of *n*-AlGaN layer emission as a function of (a) BGE coefficient G_2, and (b) AGE generation rate G_1 for the 1.27 eV BGE for all samples at 30 K. Here "Expt." indicates the experimental results.

Figure 5.13(a) shows the variation of normalized PL intensity I_N as a function of the BGE coefficient (G_2) for the 1.27 eV BGE at 30 K under a fixed AGE generation rate of 3.5×10^{22} cm^{-3}·s^{-1} for all samples. The simulated results exhibit a reasonable agreement with the experimental data. The influence of the normalized PL intensity as a function of the electron–hole generation rate of the AGE (G_1) at 30 K is calculated by setting G_2 = 2.5×10^{-12} cm^3·s^{-1} for the 1.27 eV BGE and keeping all other parameters same as in previous calculations. These results are depicted in Fig. 5.13(b). Here, a set of parameters give the behavioral insight into below-gap states acting as NRR centers in the samples, and there is a reasonable fitting with the experimental data.

The IQE with a set of parameters, shown in Table 5.3, for all samples is calculated by the ratio of radiative and total recombination rates [121] as

$$IQE = \frac{R_r}{R_r + R_{nr}} = \frac{Bnp}{Bnp + C_{n1} n N_{t1}(1 - f_{t1})} = \frac{Bnp}{G_1}, \qquad (5.5)$$

where R_r and R_{nr} are the radiative and nonradiative recombination rates, respectively. The estimated values of IQEs by using Eq. (5.5) for these four samples A(SLP-50), B(SLP-100), C(SLP-150), and D(SLP-200) are shown in Table 5.3, and depicted in Fig. 5.14 as a function of the electron–hole generation rate of the AGE (G_1) at 30 K. It is evident from Fig. 5.14 and Table 5.3 that the estimated IQE value for sample B(SLP-100) is higher and for sample C(SLP-150) is lower throughout the calculation ranges of G_1.

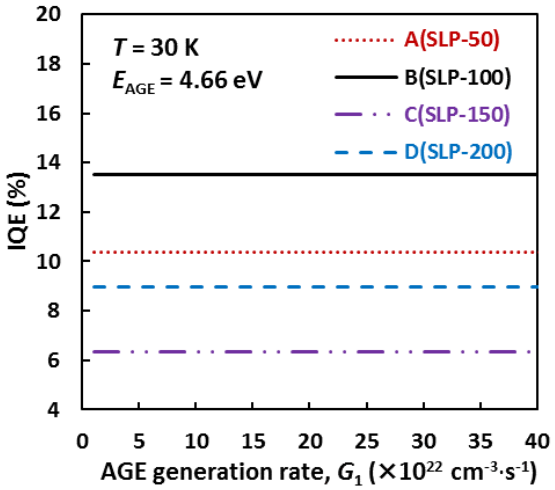

Fig. 5. 14 Estimated IQE values as a function of G_1 for all samples at 30 K.

Combining the above calculation with the structural result of Fig. 5.2, it is shown that the formation of NRR centers in *n*-AlGaN layer and QW layer has a meaningful correlation with lattice relaxation and number of SL periods. Since the *n*-AlGaN layers of samples A(SLP-50) and B(SLP-100) have the same relaxation rate, the FWHM of XRC (0002) and $(10\bar{1}2)$ tells us that threading dislocation density (TDD) is lower in sample B(SLP-100). We consider that the compositional splitting in sample C(SLP-150) increases the density of NRR centers at the boundary. Reduced relaxation of the *n*-AlGaN layer on the relaxed SL with the total thickness of 1.3 μm also increases the density of NRR centers in sample D(SLP-200). Due to the balance between reduction and formation of defects in SL and *n*-AlGaN layers, which depends on the period of SL, sample B(SLP-100) shows the lowest NRR density. It is concluded that the interpretation based on the two-level model is valid and the simulated result is consistent with the relative efficiency and temperature quenching among four samples. The TWEPL study of NRR centers guides us to optimize growth conditions further.

5.4. Conclusions

Defect states acting as NRR centers in *n*-AlGaN and QW layers of UV-B AlGaN samples, grown on the c-plane sapphire substrate by the MOCVD technique at 1150 °C, were studied by TWEPL. We detected NRR centers by adding BGE light with photon energies between 0.93 eV and 1.46 eV, which guided us to determine the energy distribution of the NRR centers. All the BGE energies decreased the PL intensity from *n*-

AlGaN and QW layers at 30 K. The most dominant quenching for *n*-AlGaN layer emission was observed by the BGE energy of 1.27 eV for samples A(SLP-50), B(SLP-100), and C(SLP-150) and by that of 1.46 eV for sample D(SLP-200). For the QW layer emission, the most dominant quenching was observed by the BGE energy of 1.27 eV for all samples. By a qualitative simulation with a two-level model, an estimated defect density ratio in the *n*-AlGaN layer of four samples is 1.7:1.0:6.5:3.4. By combining TWEPL calculation with the structural results, it is concluded that the formation of NRR centers in QW layer has a meaningful correlation with lattice relaxation, number of SL periods (SLP) and the defect densities of the *n*-AlGaN layer. Due to the balance between the reduction and formation of NRR centers in the SL and *n*-AlGaN layers, sample B(SLP-100) shows the lowest NRR density, which is consistent with the relative efficiency and temperature quenching.

CHAPTER 06

TEMPERATURE DEPENDENCE OF NONRADIATIVE RECOMBINATION PROCESSES IN UV-B AlGaN QW

6.1 Introduction

Ultraviolet (UV) light emitters in the UV-B spectral range between 280 nm and 320 nm are of great interest for applications such as phototherapy [15,122], gas sensing, plant growth lighting [123,124], and UV curing [16]. The conventional light sources in the spectral ranges from 280 nm to 320 nm are bulky, have limited lifetime, and contain toxic substances [110]. Therefore, UV-B LEDs are promising candidates, but their reliability still needs improvements [111]. The external quantum efficiency (EQE) in the aforesaid spectral ranges are still low compared to that of UV-A and UV-C [3]. One of the main reasons for the low efficiency of UV-B LEDs is the nonradiative recombination (NRR) losses [Shockley–Read– Hall (SRH) and Auger-related] [110]. Recent studies indicated that the reduction in optical power with increasing temperature (thermal droop) may also limit the performance of GaN-based LEDs, which results in an emission decrease comparable to the efficiency droop [112,113]. Therefore, understanding the mechanisms of NRR is essential in improving the efficiency of UV-B LED structures.

Many researchers are doing their research in recent years to improve the external quantum efficiency in the AlGaN-based UV-B light emitting materials [3,114]. However, it is still crucial to find the optimum growth condition since lack of lattice-matched, cost-effective and suitable substrates bring difficulties in reducing the density of defect states, which act as NRR centers in multiple quantum well (MQW) [3,23–25]. In order to improve the efficiency of light-emitting materials, it is indispensable to reduce such NRR centers. T. Onuma et al. [88] and N. Nepal et al. [89] have been used photoluminescence

(PL) and cathodoluminescence (CL) spectroscopy to investigate below-gap states in AlGaN, showing only characteristic luminescence peaks and giving relative information about NRR centers. Deep-level transient spectroscopy (DLTS) and deep-level optical spectroscopy (DLOS) have been used by other groups to investigate deep-level defects in AlGaN films, but their applications are confined due to the necessity of preparing suitable samples for the measurement with Schottky contacts or an appropriate *p–n* junction [90–92].

Our main focus in this study is the detection and characterization of NRR centers optically and to study their temperature effects in UV-B AlGaN MQW structure grown on sapphire substrates by two-wavelength excited PL (TWEPL) technique [58,64]. It is a versatile non-contacting and non-destructive scheme; there is no need for any special kind of sample preparation. In the present study, we proposed a new approach of recombination model for describing the TWEPL temperature effect with the combined analysis of both spectral and temperature-dependent data. We studied the variation of PL intensity and peak energy (E_{PL}) with temperature. The PL intensity change due to the addition of the below-gap excitation (BGE) light over that of the above-gap excitation (AGE) is also observed as functions of AGE and BGE photon number density. By systematically solving the rate equations based on the recombination model and fitting the results with experimental data, the NRR parameters are also evaluated.

6.2 Experimental methods

6.2.1 Sample structure

Figure 6.1 shows the structure of UV-B AlGaN MQW sample grown on (0001) sapphire substrate by metal-organic chemical vapor deposition (MOCVD) technique at 1155 °C. The sample comprises a 4-μm-thick AlN buffer, a 1.5-μm thick Si-doped n-AlGaN layer, three periods of MQW with 2.4-nm-thick well and 8.5-nm-thick barrier, a multi-quantum barrier (MQB), and finally a 60-nm-thick Mg doped p-AlGaN contact layer. The Al composition (x) in the barrier, well, and final barrier layers of $Al_xGa_{1-x}N$ sample were 0.64, 0.51, and 0.71, respectively. The PL peak wavelength of UV-B LED sample at 25 K is 291 nm (4.26 eV). Trimethylaluminum (TMA), trimetylgallium (TMG) and ammonia (NH_3) were used as precursors for AlGaN growth. Tetraethylsilane (TESi) precursor was used for *n*-type doping source. The reactor pressure was maintained at 10 kPa for the entire growth process.

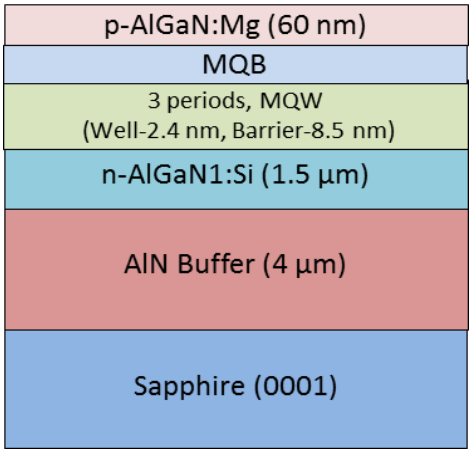

Fig. 6. 1 Sample structure.

6.2.2 Measurement

The experimental setup for characterizing the UV-B AlGaN MQW sample by TWEPL method is shown in Fig. 6.2. The sample was mounted on a Cu holder with the sapphire side up inside a temperature-controlled cryostat with three optical windows. A continuous wave (CW) diode pumped solid state laser (Model: SDL-266-005T) of wavelength 266 nm ($h\nu_{AGE}$ = 4.66 eV) serves as the AGE light ($h\nu_{AGE} > E_g$) where E_g denotes the bandgap of $Al_xGa_{1-x}N$ well layers. By adding an intermittent BGE light ($h\nu_{BGE} < E_g$) on the AGE light at the same point of the sample surface and observing the peak intensity change of PL with and without the BGE light, $I_{AGE+BGE}$ and I_{AGE}, respectively, the normalized PL intensity (I_N) is calculated as $I_N = I_{AGE+BGE}/I_{AGE}$ in the TWEPL measurement. Its deviation from unity implies the presence of NRR centers in between the energy bandgap of the sample [58,64,120]. The BGE light sources with energies 0.93 eV (1340 nm wavelength), 1.17 eV (1064 nm), 1.27 eV (980 nm), and 1.46 eV (850 nm) are used in the experiment. The detailed experimental layout and models of NRR centers can be found elsewhere [64,74,93,120].

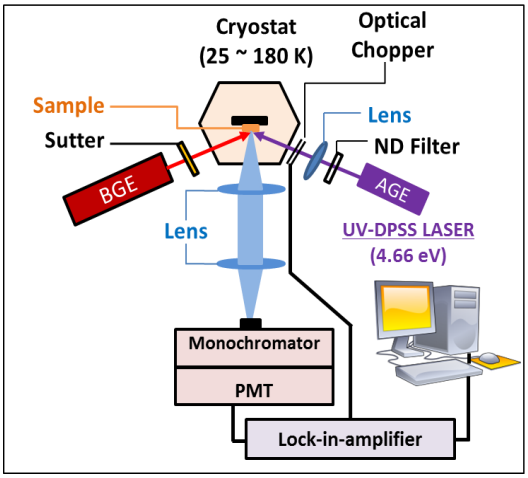

Fig. 6. 2 Experimental setup for TWEPL measurements.

6.3 Results and discussion

6.3.1 PL measurement

Photoluminescence spectra were measured as a function of excitation power density at 25 K as shown in Fig. 6.3(a) with photon energy in the horizontal axis. With increasing excitation power density, the PL intensity increases, and no peak shifting is observed. The integrated PL intensity of MQW emission increases almost linearly with increasing excitation power density at 25 K shown in the inset of Fig. 6.3(a). We performed temperature-dependent PL measurements at a fixed excitation power density (P_{AGE} = 1.04 mW·mm^{-2}) over a temperature range of 25 K to 180 K of the sample using the same excitation laser as shown in Fig. 6.3(b). The PL intensity decreased with the increase in temperature and an *S*-shaped change in the PL peak energy (E_P) is observed due to the variation of temperature.

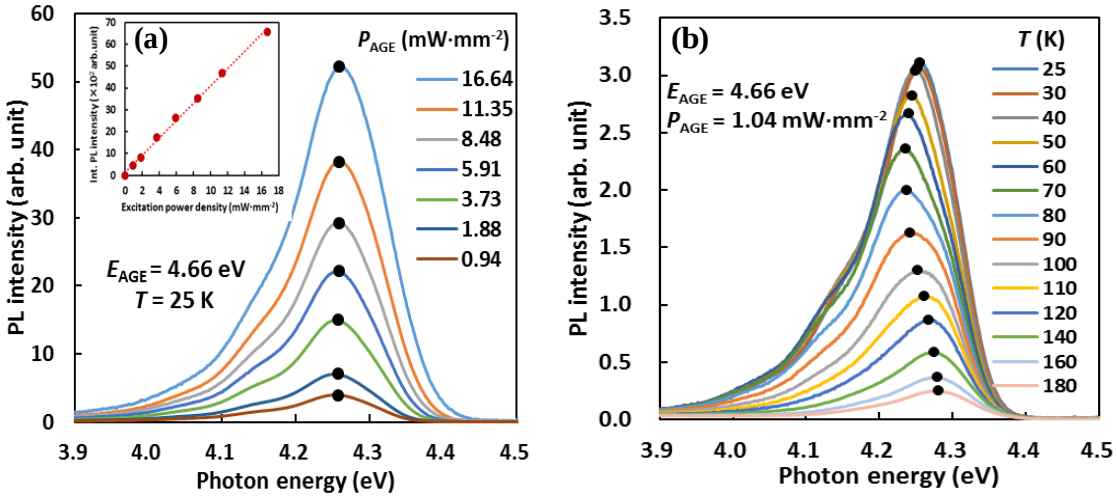

Fig. 6. 3 PL spectra of 291 nm (4.26 eV) UV-B LED structure (a) at various excitation power at 25 K and (b) at various temperature. The black solid circles of both figures mark the PL peak position arising from the QW. The inset of (a) shows the integrated PL intensity as a function of excitation power density at 25 K.

Comparing the E_P at various temperature, shown in Fig. 6.4, we can see that E_P decreases from 25 K up to 70 K. In contrast, for temperatures between 70 K and 120 K, E_P increases. With a further increase in temperature from 120 K, the E_P monotonically increases up to 160 K, after that a nearly saturated condition is observed up to 180 K. It is predicted that a decrease in the E_P may observed for temperatures higher than 180 K. Due to the low PL intensity with the same excitation condition [Fig. 6.3(b)], we could not measure E_P precisely for temperatures higher than 180 K.

Similar behavior has been observed for InGaN multiple QWs [125,126], AlGaN ternary alloys [119,127,128], GaInAs/GaAs MQWs [129], and ordered (Al)GaInP [130]. Inhomogeneity due to compositional fluctuation and carrier localization are thought to be responsible for the complex temperature dependent behavior in these cases [119,125,131]. At the temperature of 25 K, carriers are randomly distributed among the potential minima. As the temperature increases from 25 K up to 70 K, weakly localized carriers are thermally activated and relax down into other strongly localized states and reach a saturated redistribution, which results in the initial redshift of the peak energy as large as 20 meV. After 70 K, increasing temperature enable carriers to achieve the thermal equilibrium with the lattice and to occupy higher-energy levels of the localized states, thus results in the blueshift of the peak energy as large as 45 meV toward the free-exciton ground state up to 180 K (Fig. 6.4) [132].

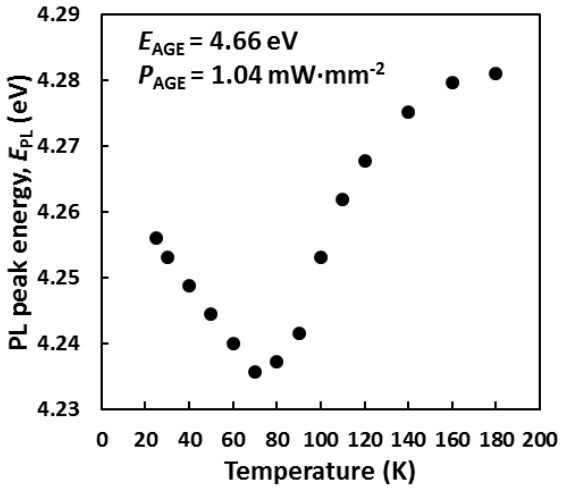

Fig. 6. 4 PL peak energy position as a function of temperature showing the *S*-shaped behavior.

The integrated PL intensity of UV-B AlGaN MQW sample as a function of temperature is shown in Fig. 6.5(a). With increasing temperature from 25 K up to 40 K, the integrated PL intensity slightly increases due to the carrier transportation between different localized states [94,120,133]. With a further increase in temperature from 40 K, the integrated PL intensity decreases drastically up to 120 K and monotonically from 120 K to 180 K. The thermal quenching behavior is determined by the activation of NRR centers and the escape of carriers from QWs [96,97]. The latter mechanism is negligible in this low-excitation condition.

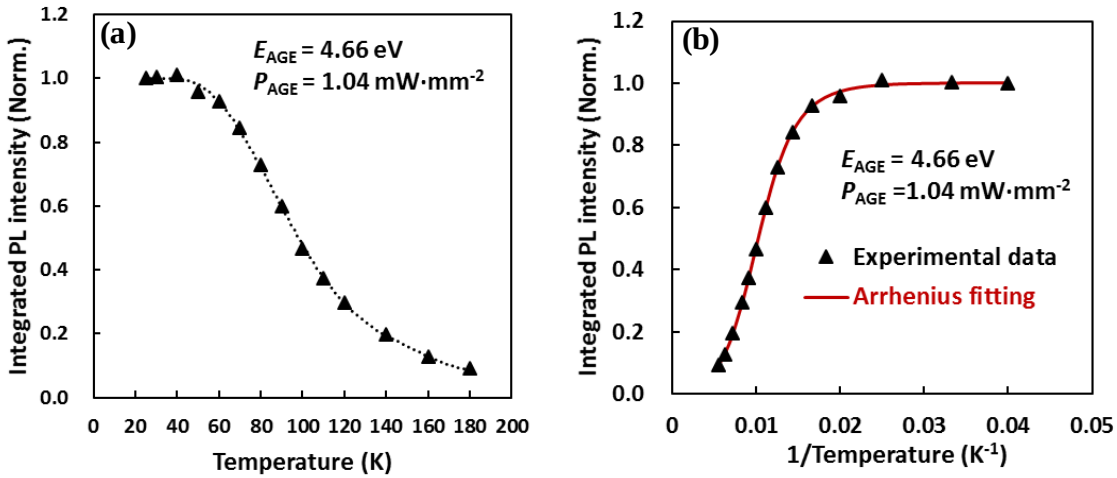

Fig. 6. 5 Integrated PL intensity as a function of (a) temperature and (b) inverse temperature. The dotted line shown in (a) for only to guide the eyes. The red solid line in (b) indicates the Arrhenius fitting.

To estimate the thermal activation energies, we calculated the integrated PL intensity as a function of inverse temperature, as shown in Fig. 6.5(b), and fitted well by using the following two-channel Arrhenius formula [96–100]:

$$I(T) = \frac{1}{\left[1 + C_1.\exp\left(\frac{-E_1}{K_B T}\right) + C_2.\exp\left(\frac{-E_2}{K_B T}\right)\right]}, \qquad (6.1)$$

Equation (6.1) indicates that more than one nonradiative pathway exists and acts together with the main NRR channel [119], where $I(T)$ is the temperature-dependent normalized integrated PL intensity. C_1 and C_2 are the two constants related to the density of NRR centers in the sample. E_1 and E_2 stand for the thermal activation energies at low- and high-temperature ranges corresponding to NRR process [97,100], and k_B (0.08617 meV/K) is the Boltzmann's constant. The origin of one of these nonradiative channels could be partially related to overflow of carriers out of the confining potential [119]. It is expected that by increasing the depth of QW, this nonradiative pathway will become less significant. All the values of the parameters in Eq. (6.1) are shown in Table 6.1.

Table 6. 1 Fitting parameters obtained from Eq. (6.1).

C_1	E_1 (meV)	C_2	E_2 (meV)
5.5	23.3	168.6	46.8

It is observed, from Table 6.1, that the value of E_2 (46.8 meV) is almost twice times than that of E_1 (23.3 meV).

6.3.2 TWEPL measurement

In order to know the distribution of NRR centers in QW layer of UV-B AlGaN sample, the normalized PL intensity I_N was measured as a function of BGE photon number density for four BGE energies as 0.93 eV, 1.17 eV, 1.27 eV, and 1.46 eV, respectively, as shown in Fig. 6.6(a). The AGE power density and the temperature were fixed at 1.04 mW·mm^{-2} and 25 K, respectively. With the addition of BGE light on the AGE, the I_N values decreased from unity for all BGE energies. It is evident from Fig. 6.6(a) that the amount of PL quenching becomes pronounced with increasing BGE photon number density. The most dominant quenching occurred by the 1.27 eV BGE energy at

the same BGE photon number density of around 1.3×10^{19} $cm^{-2}\cdot s^{-1}$ (vertical dashed line position of Fig. 6.6(a)). Figure 6.6(b) shows the variation of I_N values as a function of BGE energy at a fixed BGE photon number density of 1.3×10^{19} $cm^{-2}\cdot s^{-1}$. For BGE energies of 0.93 eV, 1.17 eV, 1.27 eV, and 1.46 eV, the I_N values were 0.958, 0.965, 0.950 and 0.974, respectively. The degree of quenching of I_N values from unity represents the presence of NRR centers in the sample. Thus, this result implies that the densities of NRR centers corresponding to the 1.27 eV BGE energy, at the same BGE photon number density, are higher in comparison to those of other BGE energies.

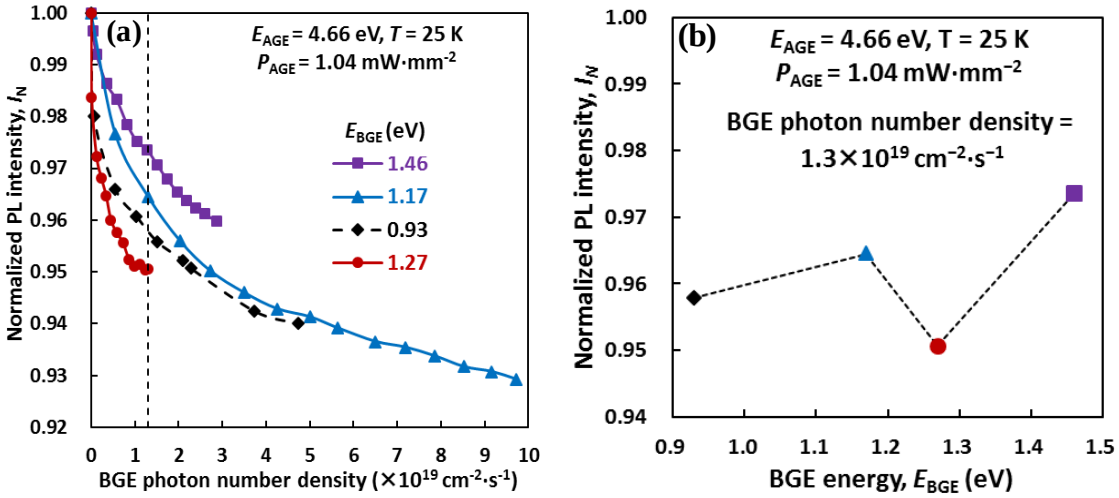

Fig. 6. 6 Variation of I_N as a function of (a) BGE photon number density, and (b) BGE energy at 25 K. The vertical dashed line in (a) indicates the same BGE photon number density position of 1.3×10^{19} $cm^{-2}\cdot s^{-1}$ for all BGE energies. The dashed line shown in (b) for only to guide the eyes.

The diminution of I_N values due to the irradiation of BGE, in UV-B MQW sample of 291 nm (4.26 eV) PL spectra at 25 K, shown in Fig. 6.6(a) is explained by the two-level recombination model schematically depicted in Fig. 6.7.

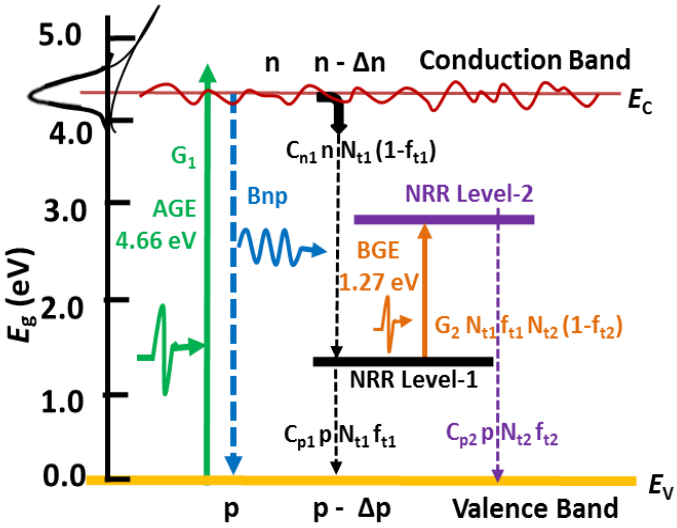

Fig. 6. 7 Two-level model of NRR process, which explains the PL intensity quenching due to the irradiation of BGE.

The figure shows the presence of a pair of NRR centers in the sample whose energy difference corresponds to that of the BGE energies [53,64,73,101]. Here, G_1 ($cm^{-3}\cdot s^{-1}$) is the generation rates of AGE, G_2 ($cm^3\cdot s^{-1}$) is the BGE excitation coefficient, B ($cm^3\cdot s^{-1}$) is the radiative recombination coefficient, C_n and C_p are the electron and hole capture coefficients, respectively, N_t is the density of NRR levels, and f_{t1} and f_{t2} are the electronic occupation functions of NRR level-1 and NRR level-2, respectively. The NRR parameters can be found by fitting experimental results based on Shockley–Read–Hall statistics [64,102].

When the BGE energy matches the energy difference between two coexisting below-gap NRR levels, level-1 and level-2 (Fig. 6.7), electrons in NRR level-1 are excited to NRR level-2, from which they recombine nonradiatively with holes in the valence band (VB) of AlGaN. Consequently, a number of electron deficiencies occur in level-1, which allows an increase in NRR from the conduction band (CB). The combination of both effects reduces the number of electron-hole pairs available for radiative recombination and results in the PL intensity quenching. In the low-BGE photon number density region, the electron occupation function of NRR level-2 remains much lower than unity, and the PL quenching avails with the increase in the BGE photon number density. Moreover, with a further increase in the BGE photon number density, the electron occupation function of NRR level-2 approaches unity and the slope of PL quenching becomes gentle; this is partly shown in Fig. 6.7(a).

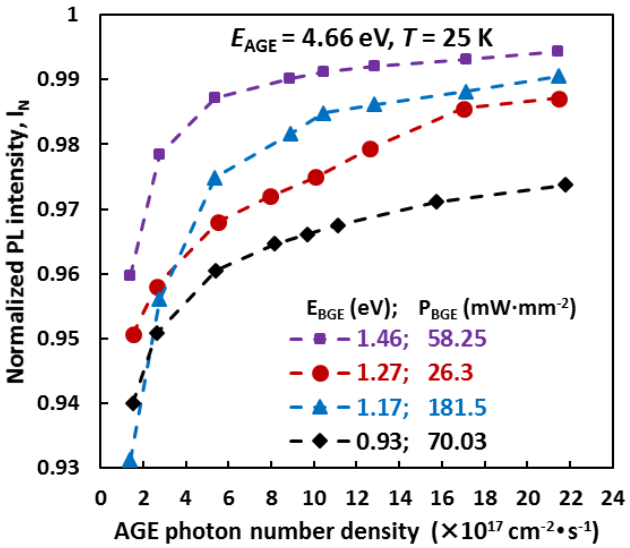

Fig. 6. 8 Variation of I_N as a function of AGE photon number density at 25 K.

The variation of I_N values as a function of AGE photon number density for four BGE energies of 0.93 eV, 1.17 eV, 1.27 eV, and 1.46 eV are shown in Fig.6. 8. With increasing AGE photon number density, the value of I_N first increases and then approaches unity. The excitation of electrons from NRR level-1 to level-2, due to the BGE, increases the NRR rate from level-1 and level-2 to the valence band at a lower AGE photon number density. With increasing AGE photon number density, band-to-band radiative recombination becomes stronger since the rate is proportional to n times p. Consequently, the normalized PL intensity I_N approaches unity with increasing AGE photon number density. A similar tendency was observed in our previous studies of TWEPL [73,103,120].

The effect of I_N values on temperature for the most-dominant BGE energy of 1.27 eV is depicted in Fig. 6.9. With increase in temperature from 25 K up to 70 K, the I_N value sharply increases and reaches at maximum one (1.02 at 70 K). With a further increasing in temperature from 70 K to 140 K, the I_N value again decreases. Further increase in temperature enables the I_N value increases and approaches to around unity at 180 K.

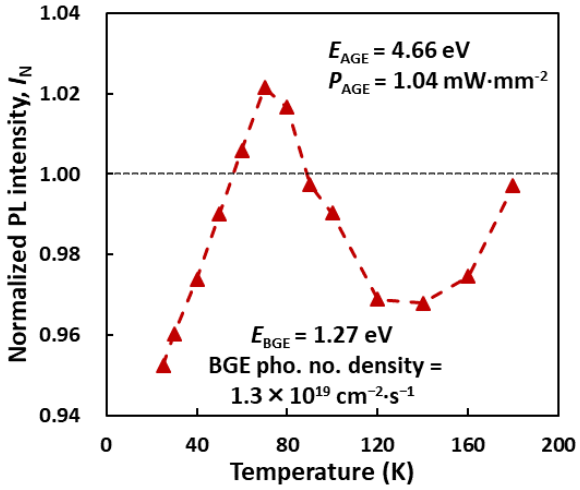

Fig. 6. 9 I_N values as a function of temperature. The horizontal dashed line through unity (I_N = 1) is the reference line, where $I_{(AGE)} = I_{(AGE+BGE)}$.

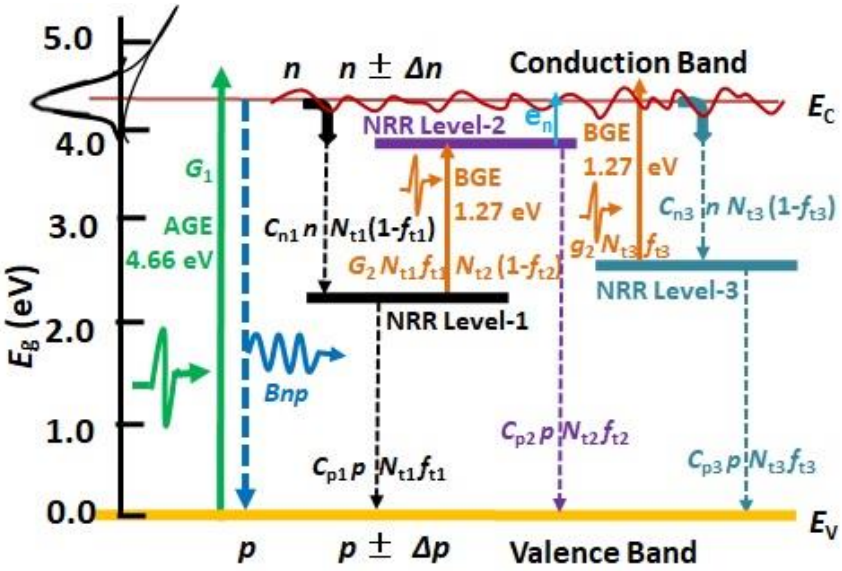

Fig. 6. 10 Energy levels diagram for the competition of one-level and two-level models of NRR process, which explains the I_N value changes with the irradiation of BGE due to variation of temperature.

The results of Fig. 6.9 can be explained by the proposed energy levels diagram shown in Fig. 6.10. Here, G_1 (cm^{-3}·s^{-1}) is the generation rates of AGE, G_2 (cm^3·s^{-1}) and g_2 (s^{-1}) are the BGE coefficients from NRR level-1 to NRR level-2 (for two-level model) and from NRR level-3 to conduction band (CB) (for one-level model), respectively. B (cm^3·s^{-1}) is the radiative recombination coefficient, C_n and C_p are the electron and hole capture coefficients, respectively, N_t and f_t are the density and the electronic occupation

functions of NRR levels, respectively, e_n is the thermal emission rate of electrons from NRR level-2 to CB. The NRR parameters can be found by fitting experimental results based on Shockley–Read–Hall statistics [64,102].

The explanation is as follows:

(i) At temperature of 25 K, carriers are randomly distributed among the potential minima. When the BGE is added with the AGE at 25 K and its energy (1.27 eV) matches with the energy difference between two coexisting below-gap NRR level-1 and level-2 (two-level model), then electrons in NRR level-1 are excited to NRR level-2, from which they recombine nonradiatively with holes in the valence band (VB) of AlGaN. Consequently, a number of electron deficiencies occur in level-1, which allows an increase in NRR from the CB. The combination of both effects reduces the number of electron-hole pairs available for radiative recombination and results in the PL intensity quenching (Figs. 6.6(a), 6.9 and 6.10).

(ii) At temperatures from 25 K -70 K: With the increase in temperature from 25 K up to 70 K, weakly localized carriers are thermally activated and relax down into other strongly localized states [132] which are very close to NRR level-3. This is consistent with the results shown in Figs. 6.3(b) and 6.4. When BGE (1.27 eV) is added and its energy matches with the energy difference between NRR level-3 and CB, then electrons are excited from NRR level-3 to CB as shown in Fig. 6.10. As a consequence, the electron concentration (n) in the CB increases and PL intensity enhances due to its directly proportional relationship with the product of *n* times *p*. This is just one level model explained in our previous results [64,74,134]. Simultaneously, process (i) also occurs with (ii) and the resultant I_N values is determined by the competition between processes (i) and (ii). At temperature around 58 K, the results of both effects are almost same for which I_N =1. At all temperatures below 58 K, the process (i) is dominating whereas temperatures above 58 K up to 70 K, process (ii) prevails.

(iii) At temperatures from 70 K - 140 K: After 70 K, increasing temperature enable carriers to achieve the thermal equilibrium with the lattice and to occupy higher-energy levels of the localized states, thus results in the blueshift of the peak energy (Figs. 6.3(b) and 6.4) [132] and the relative contribution of process (i) increases. At temperature around 88 K, the result of both effects is again same (I_N =1). At temperatures between 70 K - 88 K, the process (ii) is dominating whereas

temperatures above 88 K, process (i) prevails.

(iv) At temperature above 140 K, electrons are excited (e_n) from NRR level-2 to CB due to thermal activation energy (E_2 = 46.8 meV), which increases the PL intensity with increasing temperature. At the same time electron occupation function (f_{t2}) of NRR level-2 decreases, which enhances the excitation of electrons from NRR level-1 to NRR level-2 but reduces the NRR rate from level-2 to VB. These two opposite effects decrease the contribution of the two-level model as a whole and increase the overall PL intensity by an excitation of electrons from NRR level-3 to CB due to BGE with increasing temperature. At a temperature around 180 K, the performance of both processes, (i) and (ii), is again approaching same amount.

To justify the above explanation, based on the combined effect of two-level and one-level models, shown in Fig. 6.10, we perform the conventional PL measurements without and with the 1.27 eV BGE as shown in Fig. 6.11, at four distinct temperatures of 25 K, 70 K, 140 K, and 180 K. It is evident from Fig. 6.11 that the PL intensity quenches with the addition of BGE in both the cases at 25 K and 140 K, which is consistent with the results shown in Figs. 6.6(a) and 6.9. With the addition of BGE light, the PL intensity increases and almost unchanged for the temperatures of 70 K and 180 K, respectively. This is also consistent with the results shown in Fig. 6.9.

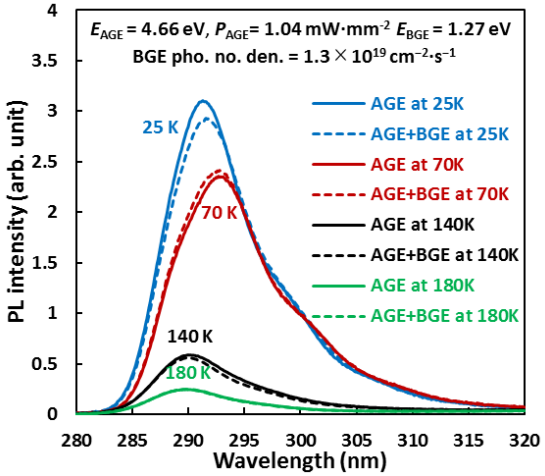

Fig. 6. 11 Effect of 1.27 eV BGE on 4.66 eV AGE at different temperatures. The solid and dashed lines indicate the PL intensities without and with the BGE, respectively.

Figure 6.12(a) shows the variation of I_N as a function of BGE photon number density at 70 K for 1.27 eV BGE. The AGE power density was fixed at 1.04 mW·mm^{-2}. With increasing BGE photon number density at 70 K, the value of I_N first increases and

then approaches saturation condition. In the low-BGE photon number density region at 70 K, the generation rate of electrons from NRR level-3 to CB is low. Therefore, the number of electron-hole pairs available for radiative recombination is lower and thus results the I_N values lower. In addition, the electron occupation function of NRR level-3 (Fig. 6.10) remains much lower than unity, in the low-BGE photon number density region at 70 K, and the PL enhancement avails with the increase in the BGE photon number density. Moreover, with a further increase in the BGE photon number density, the electron occupation function of level-3 approaches unity and the slope of PL enhancement becomes gentle [Fig. 6.12(a)].

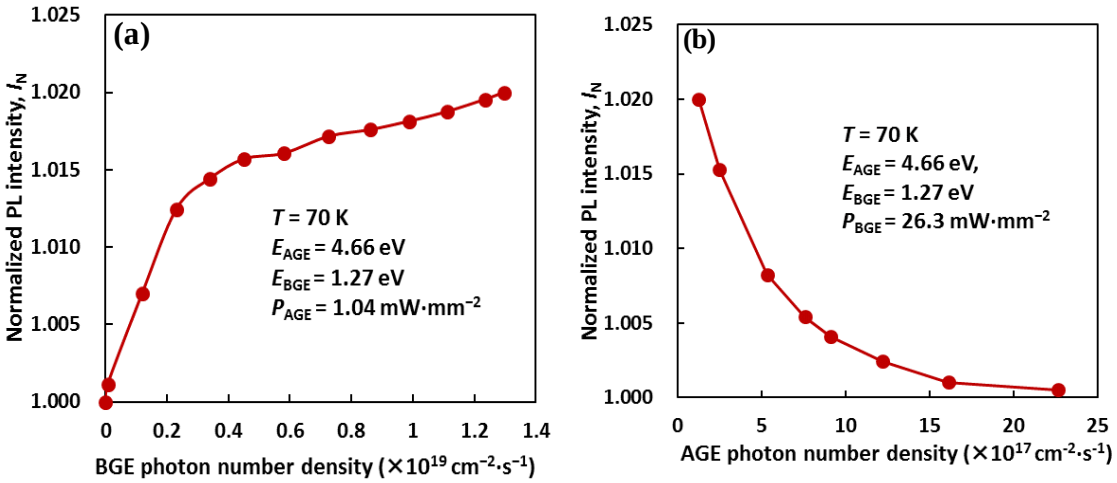

Fig. 6. 12 Variation of I_N as a function of (a) BGE 1.27 eV photon number density and (b) AGE 4.66 eV photon number density at 70 K.

The variation of I_N at 70 K, as a function of AGE photon number density for 1.27 eV BGE is shown in Fig. 6.11(b). With increasing AGE photon number density, the values of I_N first decrease drastically and then approaches unity. At a lower AGE photon number density, electron concentration (n) increases in the bands due to the addition of BGE and the PL intensity increases. Consequently, I_N values are higher. With increasing AGE photon number density, band-to-band radiative recombination becomes stronger since the rate is proportional to n times p. The normalized PL intensity I_N first decreases (as $I_N = I_{AGE+BGE}/I_{AGE}$) and then approaches unity.

6.3.3 Rate equation analysis

In order to corroborate our qualitative interpretations, for the results of Fig. 6.6(a) at 25 K by the two-level model, and for the results of Fig. 6.11(a) at 70 K by one-level

model, a semi-quantitative simulation of the TWEPL results was carried out for the most dominant PL quenching occurred by the 1.27 eV BGE energy. The rate equations for theses two-level and one-level models (Fig. 6.10) can be written [51,52,64] as:

for two-level model (at 25 K):

$$\left.\begin{aligned}
&\frac{dn}{dt} = G_1 - Bnp - C_{n1} n N_{t1}(1 - f_{t1}) = 0, \\
&\frac{dp}{dt} = G_1 - Bnp - C_{p1} p N_{t1} f_{t1} - C_{p2} p N_{t2} f_{t2} = 0, \\
&\frac{df_{t1}}{dt} = C_{n1} n(1 - f_{t1}) - C_{p1} p f_{t1} - G_2 f_{t1} N_{t2}(1 - f_{t2}) = 0, \\
&\frac{df_{t2}}{dt} = G_2 N_{t1} f_{t1}(1 - f_{t2}) - C_{p2} p f_{t2} = 0,
\end{aligned}\right\} \qquad (6.2)$$

while considering the charge neutrality condition (CNC)

$$n + N_{t1} f_{t1} + N_{t2} f_{t2} = n_0 + p, \qquad (6.3)$$

and

for one-level model (at 70K):

$$\left.\begin{aligned}
&\frac{dn}{dt} = G_1 - Bnp - C_{n3} n N_{t3}(1 - f_{t3}) + g_2 N_{t3} f_{t3} = 0, \\
&\frac{dp}{dt} = G_1 - Bnp - C_{p3} p N_{t3} f_{t3} = 0, \\
&\frac{df_{t3}}{dt} = C_{n3} n(1 - f_{t3}) - C_{p3} p f_{t3} - g_2 f_{t3} = 0,
\end{aligned}\right\} \qquad (6.4)$$

with considering CNC

$$n + N_{t3} f_{t3} = n_0 + p, \qquad (6.5)$$

where n_0 is the density of free electrons in the QW and its value is known (2.0×10^{17} cm^{-3}) from the samples' growers. The radiative recombination coefficient B is considered as 1.0×10^{-11} $cm^3 \cdot s^{-1}$ for the AlGaN material [102,107–109,120]. The generation rate of the AGE ($G_1 = 3.5\times10^{22} cm^{-3} \cdot s^{-1}$) is calculated experimentally by using the following equation [104,105,120]:

$$G_1 = P_{laser}(1 - R)\alpha \Big/ \left(A_{spot} h\nu\right), \qquad (6.6)$$

where P_{laser} is the excitation power, R (18%) is the Fresnel reflection at the sample surface, A_{spot} is the laser spot size (1.06×10^{-3} cm^2) on the sample surface, $h\nu$ (E_{AGE} = 4.66 eV) is

the photon energy of the excitation laser, and α (3.1×10^5 cm^{-1}) [106] is the absorption coefficient of AlGaN at 266 nm (4.66 eV). It is impossible to evaluate the BGE coefficients (G_2 and g_2) from the absorption coefficient measurement since there is no fundamental absorption for this source. Here, we use a constant factor for these conversions from the experimental photon number density of the BGE sources [102,120]. The system of rate equations can be solved numerically and the dependencies of n, p, f_{t1}, and f_{t2} on G_2 can be found for the constant parameters of G_1, B and n_0, and the sample's NRR level-1 and level-2 dependent parameters of C_{n1}, C_{p1}, $N_{t1,}$ C_{p2} and N_{t1} for two levels model (at 25 K). The emission rate of electrons from NRR level-2, e_n, in Fig. 6.7 is omitted in Eq. (6.2) as we consider the temperature region below 70 K. The dependencies of n, p, and f_{t3} on g_2 can be found for the same constant parameters and the sample's NRR level-3 dependent parameters of C_{n3}, C_{p3} and N_{t3} for one level model (at 70 K). The constant parameters are listed in Table 6.2, for convenience.

Table 6. 2 Constant parameters of rate Eqs. (6.2) to (6.5)

G_1 ($cm^{-3}\cdot s^{-1}$)	B ($cm^{-3}\cdot s^{-1}$)	n_0 (cm^{-3})
3.5×10^{22}	1.0×10^{-11}	2.0×10^{17}

By systematically solving and fitting the result with experimental data (Fig. 6.13), the NRR parameters are obtained for the most-dominant BGE energy of 1.27 eV for the sample and are shown in Table 6.3.

Table 6. 3 Parameters of rate Eqs. (6.2) to (6.5) based on Fig. 6.10 for 1.27 eV BGE.

For NRR level-1			For NRR level-2		For NRR level-3		
C_{n1} ($cm^{-3}\cdot s^{-1}$)	C_{p1} ($cm^{-3}\cdot s^{-1}$)	N_{t1} (cm^{-3})	C_{p2} ($cm^{-3}\cdot s^{-1}$)	N_{t2} (cm^{-3})	C_{n3} ($cm^{-3}\cdot s^{-1}$)	C_{p3} ($cm^{-3}\cdot s^{-1}$)	N_{t3} (cm^{-3})
1.2×10^{-9}	1.0×10^{-9}	2.8×10^{16}	8.5×10^{-12}	1.0×10^{16}	8.0×10^{-11}	2.0×10^{-11}	2.7×10^{15}

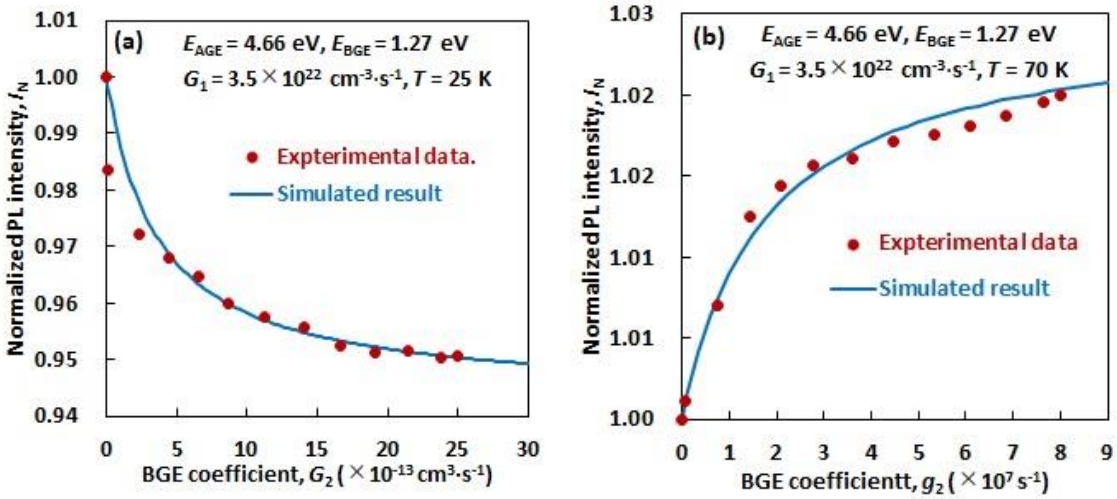

Fig. 6. 13 Effect of I_N values as a function of BGE coefficient (a) G_2 at 25 K by two-level model, and (b) g_2 at 70 K by one-level model for the 1.27 eV BGE.

Figure 6.13 shows the effect of normalized PL intensity I_N as a function of the BGE coefficient G_2 and g_2 by two-level model at 25 K and by one-level model at 70 K, respectively, for the most-dominant BGE energy of 1.27 eV under a fixed electron-hole generation rate of the AGE (G_1 = 3.5×10^{22} cm^{-3}·s^{-1}) for the sample. Here, a set of parameters give the behavioral insight into below-gap states acting as NRR centers in the sample, and there is a reasonable agreement with the experimental data.

The internal quantum efficiency (IQE) value of the sample at 25 K is calculated with a set of parameters, shown in Table 6.3, by the ratio of radiative and total recombination rates [121] as:

$$IQE = \frac{R_r}{R_r + R_{nr}} = \frac{Bnp}{Bnp + C_{n1} n N_{t1}(1 - f_{t1})} = \frac{Bnp}{G_1}, \qquad (6.7)$$

where R_r and R_{nr} are the radiative and nonradiative recombination rates, respectively. The estimated IQE value by using Eq. 6.7, for the sample is depicted in Fig. 6.14 as a function of the electron-hole generation rate of the AGE (G_1). It is evident from Fig. 6.14 that for a reasonable agreement of our simulated results with the experimental data [Fig. 13(a)], the estimated IQE value at 25 K for the sample increases only slightly with increasing G_1 value since the whole range of G_1 remains within weak excitation condition.

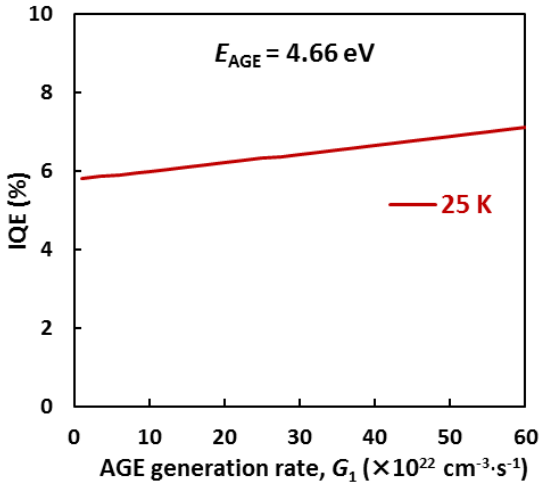

Fig. 6. 14 Estimated IQE values as a function of G_1 at 25 K.

6.4 Conclusion

Temperature dependence of NRR centers in UV-B AlGaN MQW sample grown on c-plane sapphire substrate by MOCVD technique were studied by TWEPL. We detected NRR centers by adding BGE light with photon energies of 0.93, 1.17, 1.27, and 1.46 eV, which helped us to determine the energy distribution of the NRR centers. All the BGE energies decreased PL intensity at 25 K, and the most distinct quenching was observed by the 1.27 eV BGE at the same BGE photon number density of 1.3×10^{19} cm^{-2}·s^{-1}. The temperature dependent I_N results for the most-dominant BGE energy of 1.27 eV shows that the one-level model dominates over that of two-level model in the temperature range 58 K < T < 88 K. In other cases of temperature region, the two-level model prevailes. The combination of one-level and two-level model is consistent with the temperature dependence of PL peak energy. The simulated results of the NRR processes matched well with the experimental results of BGE and AGE density dependence. We consider that NRR level-3 accepts electrons from localized states in CB tail, and increases I_N values up to 70 K. Distribution and behavior of NRR centers depend on detailed growth conditions and the structure of samples and give us a guideway to optimization.

CHAPTER 07

SUMMARY AND FUTURE DIRECTIONS

This chapter gives an overall conclusion based on the studied samples and some suggestions for future work. Three different samples series viz; UV-C (deep UV) AlGaN MQW samples grown at different temperatures, UV-B AlGaN MQW samples grown at 1150 ^{o}C with different superlattice periods, UV-B AlGaN MQW sample grown at 1155 ^{o}C have been characterized by photoluminescence (PL) and two-wavelength excited photoluminescence (TWEPL). All these samples were grown on sapphire substrates by MOCVD technique. Based on the experimental results, the following summaries are drawn:

7.1 Summary

Defect states acting as NRR centers in two AlGaN MQW samples grown at two different temperatures, 1140 °C and 1180 °C on c-plane sapphire substrate by MOCVD technique, have been studied by TWEPL method at a temperature of about 25 K. The defect states have been detected and the energy distribution of NRR centers for both samples have been determined by adding BGE light with photon energies of 0.93 eV, 1.17 eV, 1.27 eV, and 1.46 eV. All the BGE energies decreased PL intensity, and the most distinct quenching was observed for the BGE energy of 1.46 eV at the same BGE photon number density. The PL intensity quenching by the 1.46 eV BGE did not show enough of a difference between the two samples which mean that the defect densities between two samples at this energy level are almost similar. It is observed that the PL quenching corresponding to the 0.93 eV, 1.17 eV, and 1.27 eV BGE energies are lower in higher growth temperature sample (1180 °C) than that of lower growth temperature sample (1140 °C). By a qualitative simulation with a two-level model for the second-most dominant BGE BGE energy of 1.27 eV, it was found that the density of NRR level-2 for the sample grown at 1140 °C was 1.5 times higher than that of the sample grown at

1180 °C, which determines the PL efficiency of the samples. It is concluded that a different density of NRR centers results directly from only a 40 °C difference in growth temperature and indirectly from a change in Al composition. The use of a high-temperature growth condition is more effective in reducing the density of NRR centers than a low-temperature growth condition in this case. The TWEPL study of NRR centers guides us to further optimize growth conditions.

Four UV-B AlGaN MQW samples with varying number of superlattice periods from 50 to 200 in the superlattice structure, grown on c-plane sapphire substrate by MOCVD technique at 1150 °C, have been characterized by TWEPL at 30 K. The NRR centers have been detected and their energy distribution has been determined by adding BGE light with photon energies between 0.93 eV and 1.46 eV. All the BGE energies decreased PL intensity from *n*-AlGaN and QW layers at 30 K. By a qualitative simulation for the most dominant BGE energy of 1.27 eV with a two-level model, an estimated defect density ratio in the *n*-AlGaN layer of four samples is 1.7 : 1.0 : 6.5 : 3.4. The formation of NRR centers in QW layer has a meaningful correlation with lattice relaxation, number of SLP and the defect densities of the *n*-AlGaN layer. Due to the balance between the reduction and formation of NRR centers in the superlattice and *n*-AlGaN layers, the sample with 100 superlattice periods shows the lowest NRR density.

Temperature dependence of NRR centers in UV-B AlGaN MQW sample grown on c-plane sapphire substrate by MOCVD technique have been studied by TWEPL. The NRR centers have been detected by adding BGE light with photon energies of 0.93 eV, 1.17 eV, 1.27 eV, and 1.46 eV, which helped us to determine the energy distribution of the NRR centers. All the BGE energies decreased PL intensity at 25 K, and the most distinct quenching was observed by the 1.27 eV BGE at the same BGE photon number density of 1.3×10^{19} $cm^{-2}\cdot s^{-1}$. The temperature dependent I_N results for the most-dominant BGE energy of 1.27 eV shows that the one-level model dominates over that of two-level model in the temperature range 58 K < T < 88 K. In other cases of temperature region, the two-level model prevails. The combination of one-level and two-level model is consistent with the temperature dependence of PL peak energy. The simulated results of the NRR processes matched well with the experimental results of BGE and AGE density dependence. It is considered that NRR level-3 accepts electrons from localized states in conduction band tail and increases the normalized PL intensity (I_N) up to 70 K.

Distribution and behavior of NRR centers depend on detailed growth conditions and the structure of samples and give us a guideway to optimization.

7.2 Future directions

Although significant research work has been done for various samples by two-wavelength excited photoluminescence (TWEPL) technique, there are many defect related features are still now unresolved and require further investigation. The following research work can be done to obtain more defect related information from these promising AlGaN MQW materials.

(i) We have studied series of AlGaN MQW samples grown by MOCVD technique with different growth conditions. The study of a series of samples with the same growth conditions but different growth technique can give more important information about the spatial distribution and the origin of the defect levels.

(ii) A combination of our optical characterization by TWEPL with other defect characterization techniques like deep-level transient spectroscopy (DLTS), deep level optical spectroscopy (DLOS) etc. can provide more significant information about the origin and the distribution of defects.

(iii) By systematically solving rate equations and fitting the results with experimental data, we have evaluated the NRR parameters for a specific BGE energy. There are several assumptions to solve these equations. By utilizing time-resolved Photoluminescence (TRPL) spectroscopy on these materials, the lifetime and capture coefficient of carriers can be obtained. The combination of both TWEPL and TRPL measurements can be helpful for the quantitative analysis of these materials.

(iv) The investigation of the energy distribution of NRR centers can be done by using a tunable and/or different BGE energy sources. This may provide intensive information about the NRR properties of AlGaN materials.

APPENDIX

A.1 Calibration of output power of different BGE sources

Four different light sources of photon energies 1.46 eV (850 nm wavelength), 1.27 eV (980 nm), 1.17 eV (1064 nm) and 0.93 eV (1340 nm) have been used as below-gap excitation (BGE) light in the experiment of two-wavelength excited photoluminescence (TWEPL) measurement. The output power of the laser 0.93 eV (1340 nm) was controlled only by using neutral density (ND) filters in front of the laser. However, the calibration of the other BGE sources is presented in the following Figures:

BGE: 1.46 eV (850 nm)

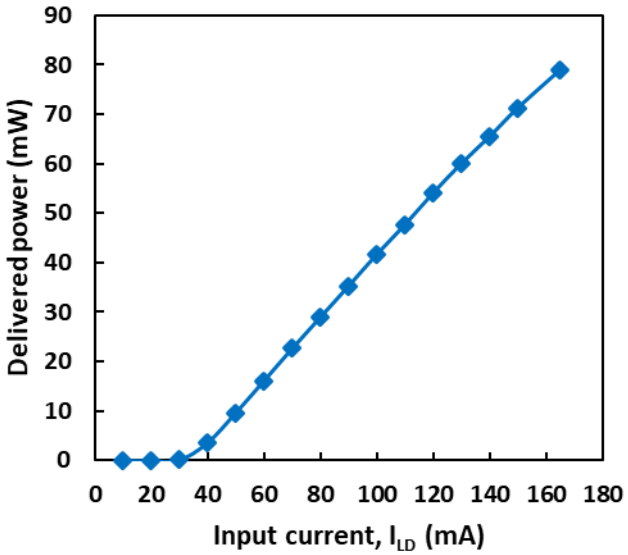

Fig. A. 1 Calibration of the 1.46 eV (850 nm) laser.

BGE: 1.27 eV (980 nm)

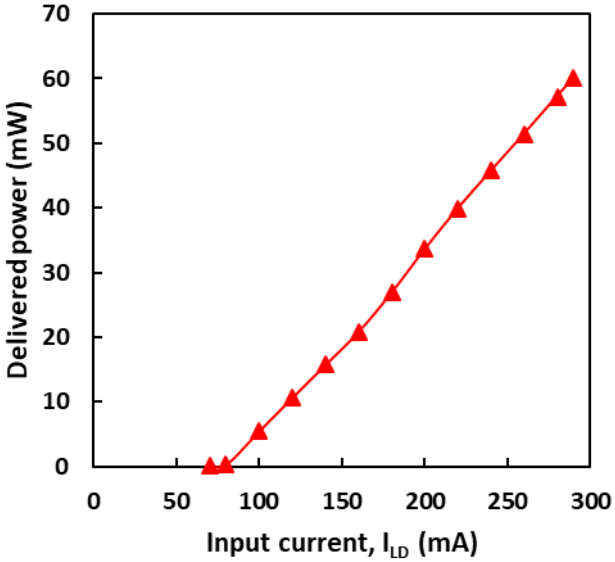

Fig. A. 2 Calibration of the 1.27 eV (980 nm) laser.

BGE: 1.17 eV (1064 nm)

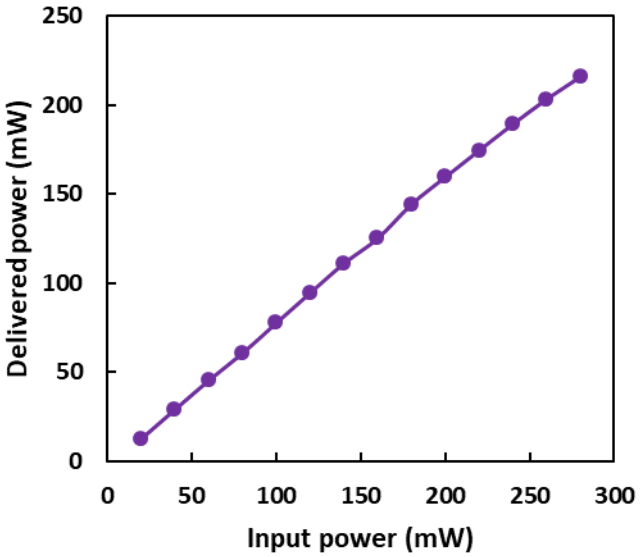

Fig. A. 3 Calibration of the 1.17 eV (1064 nm) laser.

A.2 Beam parameters of different laser sources

Beam diameter of different lasers was measured by using knife-edge method. The beam parameters are summarized as below:

Table A. 1 Beam parameters of different laser sources

Sources	Laser	Beam Diameter (mm)	Beam Cross-section (mm^2)
AGE	4.66 eV (266 nm)	0.37	0.106
BGE	1.46 eV (850 nm)	1.31	1.35
	1.27 eV (980 nm)	1.7	2.28
	1.17 eV (1064 nm)	1.23	1.18
	0.93 eV (1340 nm)	1.2	1.14

REFERENCES

[1] S. Nakamura, M.R. Krames, History of gallium-nitride-based light-emitting diodes for illumination, Proc. IEEE. 101 (2013) 2211–2220. https://doi.org/10.1109/JPROC.2013.2274929.

[2] V. Liuolia, Localization effects in ternary nitride semiconductors, KTH, 2012.

[3] M. Kneissl, J. Rass, III-Nitride Ultraviolet Emitters, Springer, Berlin, 2016. https://doi.org/10.1007/978-3-319-24100-5.

[4] H.P. Maruska, J.J. Tietjen, The preparation and properties of vapor-deposited single-crystal-line GaN, Appl. Phys. Lett. 15 (1969) 327–329. https://doi.org/10.1063/1.1652845.

[5] H. Amano, N. Sawaki, I. Akasaki, Y. Toyoda, Metalorganic vapor phase epitaxial growth of a high quality GaN film using an AlN buffer layer, Appl. Phys. Lett. 48 (1986) 353–355. https://doi.org/10.1063/1.96549.

[6] H. Amano, M. Kito, K. Hiramatsu, I. Akasaki, P-type conduction in Mg-doped GaN treated with low-energy electron beam irradiation (LEEBI), Jpn. J. Appl. Phys. 28 (1989) L2112–L2114. https://doi.org/10.1143/JJAP.28.L2112.

[7] S. Nakamura, M. Senoh, N. Iwasa, S.I. Nagahama, High-brightness InGaN blue, green and yellow light-emitting diodes with quantum well structures, Jpn. J. Appl. Phys. 34 (1995) L797–L799. https://doi.org/10.1143/JJAP.34.L797.

[8] S. Nakamura, M. Senoh, S. Nagahama, N. Iwasa, T. Yamada, T. Matsushita, H. Kiyoku, Y. Sugimoto, InGaN-Based Multi-Quantum-Well-Structure Laser Diodes, Jpn. J. Appl. Phys. 35 (1996) L74–L76.

[9] S. Nakamura, The roles of structural imperfections in InGaN-based blue light-emitting diodes and laser diodes, Science (80-.). 281 (1998) 956–961. https://doi.org/10.1126/science.281.5379.956.

[10] H. Hirayama, N. Maeda, S. Fujikawa, S. Toyoda, N. Kamata, Recent progress and future prospects of AlGaN- based high-efficiency deep-ultraviolet light-emitting diodes, Jpn. J. Appl. Phys. 53 (2014) 100209. https://doi.org/10.7567/JJAP.53.100209.

[11] J. Han, M.H. Crawford, R.J. Shul, J.J. Figiel, M. Banas, L. Zhang, Y.K. Song, H. Zhou, A. V. Nurmikko, AlGaN/GaN quantum well ultraviolet light emitting diodes, Appl. Phys. Lett. 73 (1998) 1688.

[12] A. Kinoshita, H. Hirayama, M. Ainoya, Y. Aoyagi, A. Hirata, Room-temperature operation at 333 nm of Al0.03Ga0.97N/Al0.25Ga0.75N quantum-well light-emitting diodes with Mg-doped superlattice layers, Appl. Phys. Lett. 77 (2000) 175–177. https://doi.org/10.1063/1.126915.

[13] T. Nishida, H. Saito, N. Kobayashi, Efficient and high-power AlGaN-based ultraviolet light-emitting diode grown on bulk GaN, Appl. Phys. Lett. 79 (2001) 711–712. https://doi.org/10.1063/1.1390485.

[14] M. Ippommatsu, Optronics, Optronics. 2 (2014) 71.

[15] H. Hönigsmann, History of phototherapy in dermatology, Photochem. Photobiol. Sci. 12 (2013) 16–21. https://doi.org/10.1039/c2pp25120e.

[16] A. Endruweit, M.S. Johnson, A.C. Long, Curing of composite components by ultraviolet radiation: A review, Polym. Compos. 27 (2006) 119–128. https://doi.org/10.1002/pc.20166.

[17] J.S. Hill, M. D. Daniell, A HISTORY OF PHOTODYNAMIC THERAPY, Aust. N. Z. J. Surg. 61 (1991) 340–348.

[18] J.A. Parrish, K.F. Jaenicke, Action spectrum for phototherapy of psoriasis, J. Invest. Dermatol. 76 (1981) 359–362. https://doi.org/10.1111/1523-1747.ep12520022.

[19] P.J. Hargis, Jr., T.J. Sobering, G.C. Tisone, J.S. Wagner, S.A. Young, R.J. Radloff, Ultraviolet fluorescence identification of protein, DNA, and bacteria, in: Opt. Instrum. Gas Emiss. Monit. Atmos. Meas., SPIE, 1995: p. 147. https://doi.org/10.1117/12.205554.

[20] M. Schreiner, J. Martínez-Abaigar, J. Glaab, M. Jansen, UV-B Induced Secondary Plant Metabolites, Opt. Photonik. 9 (2014) 34–37. https://doi.org/10.1002/opph.201400048.

[21] J.S. Speck, S.J. Rosner, The Role of threading dislocations in the physical properties of GaN and its alloys, Phys. B Condens. Matter. 273–274 (1999) 24–32. https://doi.org/10.1016/S0921-4526(99)00399-3.

[22] A.M. Armstrong, M.H. Crawford, D.D. Koleske, Contribution of deep-level defects to decreasing radiative efficiency of InGaN/GaN quantum wells with increasing emission wavelength, Appl. Phys. Express. 7 (2014) 032101. https://doi.org/10.7567/APEX.7.032101.

[23] S.P. DenBaars, S. Keller, Semiconductors and Semimetals, Academic, Newwork, Vol. 50, P.11, 1998.

[24] H. Hirayama, S. Fujikawa, N. Kamata, Recent progress in AlGaN-based deep-UV LEDs, Electron. Commun. Japan. 98 (2015) 1–8. https://doi.org/10.1002/ecj.11667.

[25] W. Götz, N.M. Johnson, Semiconductors and Semimetals, Academic, New York, Vol. 57, p. 185, 1999.

[26] Y. Tokuda, Y. Matsuoka, H. Ueda, O. Ishiguro, N. Soejima, T. Kachi, DLTS study of n-type GaN grown by MOCVD on GaN substrates, Superlattices Microstruct. 40 (2006) 268–273. https://doi.org/10.1016/j.spmi.2006.07.025.

[27] J.W. Kim, G.H. Song, J.W. Lee, Observation of minority-carrier traps in InGaN/GaN multiple-quantum-well light-emitting diodes during deep-level transient spectroscopy measurements, Appl. Phys. Lett. 88 (2006) 182103. https://doi.org/10.1063/1.2200392.

[28] Z.Q. Fang, B. Claflin, D.C. Look, D.S. Green, R. Vetury, Deep traps in AlGaN/GaN heterostructures studied by deep level transient spectroscopy: Effect of carbon concentration in GaN buffer layers, J. Appl. Phys. 108 (2010) 063706. https://doi.org/10.1063/1.3488610.

[29] T.T. Duc, G. Pozina, E. Janzén, C. Hemmingsson, Investigation of deep levels in bulk GaN material grown by halide vapor phase epitaxy, J. Appl. Phys. 114 (2013) 153702. https://doi.org/10.1063/1.4825052.

[30] A. Armstrong, C. Poblenz, U.K. Mishra, J.S. Speck, S.A. Ringel, Comparison of deep level spectra in p-type and n-type GaN grown by molecular beam epitaxy, Phys. Status Solidi Basic Res. 244 (2007) 1867–1871. https://doi.org/10.1002/pssb.200674831.

[31] E.K. Kim, J.S. Kim, S.Y. Kwon, H.J. Kim, E. Yoon, Electrical study on indium-rich InGaN/GaN multi-quantum-well system, J. Korean Phys. Soc. 49 (2006)

2132–2135.

[32] M.M. Sobolev, N.M. Shmidt, Deep-level transient spectroscopy studies of light-emitting diodes based on multiple-quantum-well InGaN/GaN structure, Phys. B Condens. Matter. 404 (2009) 4907–4910. https://doi.org/10.1016/j.physb.2009.08.268.

[33] C. Rivera, J.L. Pau, E. Muñoz, T. Ive, O. Brandt, Photocapacitance characteristics of (In,Ga)N/GaN MQW structures, Phys. Status Solidi Curr. Top. Solid State Phys. 3 (2006) 1978–1982. https://doi.org/10.1002/pssc.200565224.

[34] G. Parish, Growth and characterization of aluminium gallium nitride / gallium nitride ultraviolet detectors, Electr. Comput. Eng. Univ. Calif. (2001).

[35] F. Yun, M.A. Reshchikov, L. He, T. King, H. Morkoç, S.W. Novak, L. Wei, Energy band bowing parameter in Al xGa 1-xN alloys, J. Appl. Phys. 92 (2002) 4837–4839. https://doi.org/10.1063/1.1508420.

[36] M. Androulidaki, N.T. Pelekanos, K. Tsagaraki, E. Dimakis, E. Iliopoulos, A. Adikimenakis, E. Bellet-Amalric, D. Jalabert, A. Georgakilas, Energy gaps and bowing parameters of InAlGaN ternary and quaternary alloys, Phys. Status Solidi Curr. Top. Solid State Phys. 3 (2006) 1866–1869. https://doi.org/10.1002/pssc.200565280.

[37] M. JULKARNAIN, Characterization of GaN Based Light Emitting Semiconductors by Two-wavelength Excited Photoluminescence, Graduate School of Science and Engineering, Saitama University, 2016.

[38] S.R. Lee, A.F. Wright, M.H. Crawford, G.A. Peterson, J. Han, R.M. Biefeld, The band-gap bowing of AlxGa1-xN alloys, Appl. Phys. Lett. 74 (1999) 3344–3346.

[39] M.D. McCluskey, C.G. Van De Walle, C.P. Master, L.T. Romano, N.M. Johnson, Large band gap bowing of InxGa1-xN alloys, Appl. Phys. Lett. 72 (1998) 2725–2726. https://doi.org/10.1063/1.121072.

[40] J. Wu, W. Walukiewicz, K.M. Yu, J.W. Ager, E.E. Haller, H. Lu, W.J. Schaff, Small band gap bowing in In1-xGaxN alloys, Appl. Phys. Lett. 80 (2002) 4741–4743. https://doi.org/10.1063/1.1489481.

[41] D.O. Demchenko, I.C. Diallo, M.A. Reshchikov, Yellow luminescence of gallium nitride generated by carbon defect complexes, Phys. Rev. Lett. 110 (2013) 087404.

https://doi.org/10.1103/PhysRevLett.110.087404.

[42] D. Johnstone, Summary of deep level defect characteristics in GaN and AlGaN, in: H. Morkoc, C.W. Litton (Eds.), SPIE, 2007: pp. 64730L-64730L–11. https://doi.org/10.1117/12.709709.

[43] A. Armstrong, A.R. Arehart, D. Green, U.K. Mishra, J.S. Speck, S.A. Ringel, Impact of deep levels on the electrical conductivity and luminescence of gallium nitride codoped with carbon and silicon, J. Appl. Phys. 98 (2005) 053704. https://doi.org/10.1063/1.2005379.

[44] C.H. Seager, A.F. Wright, J. Yu, W. Götz, Role of carbon in GaN, J. Appl. Phys. 92 (2002) 6553–6560. https://doi.org/10.1063/1.1518794.

[45] M.A. Reshchikov, D.O. Demchenko, A. Usikov, H. Helava, Y. Makarov, Carbon defects as sources of the green and yellow luminescence bands in undoped GaN, Phys. Rev. B - Condens. Matter Mater. Phys. 90 (2014) 235203. https://doi.org/10.1103/PhysRevB.90.235203.

[46] R. Gillen, J. Robertson, A hybrid density functional view of native vacancies in gallium nitride, J. Phys. Condens. Matter. 25 (2013) 405501. https://doi.org/10.1088/0953-8984/25/40/405501.

[47] J. Neugebauer, C.G. Van de Walle, Gallium vacancies and the yellow luminescence in GaN, Appl. Phys. Lett. 69 (1996) 503–505. https://doi.org/10.1063/1.117767.

[48] J.L. Lyons, A. Janotti, C.G. Van De Walle, Carbon impurities and the yellow luminescence in GaN, Appl. Phys. Lett. 97 (2010) 152108. https://doi.org/10.1063/1.3492841.

[49] A. Hierro, A.R. Arehart, B. Heying, M. Hansen, U.K. Mishra, S.P. Denbaars, J.S. Speck, S.A. Ringel, Impact of Ga/N flux ratio on trap states in n-GaN grown by plasma-assisted molecular-beam epitaxy, Appl. Phys. Lett. 80 (2002) 805–807. https://doi.org/10.1063/1.1445274.

[50] S.M. Sze, K.K. Ng, Physics and Properties of Semiconductors—A Review, in: Phys. Semicond. Devices, Third, Wiley Interscience, 2006: pp. 5–75.

[51] W. Shockley, W.T. Read, Statistics of the recombinations of holes and electrons, Phys. Rev. 87 (1952) 835–842. https://doi.org/10.1103/PhysRev.87.835.

[52] R.N. Hall, Electron-Hole Recombination in Germanium, Phys. Rev. 87 (1952) 387.

[53] H.G. Grimmeiss, B. Monemar, Some optical properties of Cu in GaP, Phys. Status Solidi (A). 19 (1973) 505–511.

[54] B. Monemar, L. Samuelson, Optical transitions via the leep O donor in Gap. I. Phonon interaction in low-temperature spectra, Phys. Rev. B. 18 (1978) 809–829. https://doi.org/https://doi.org/10.1103/PhysRevB.18.809.

[55] M. Tajima, 13th International Conference on Defects in Semiconductors, in: Coronado, California: The Metallurgical Society of AIME, 1984.

[56] N. Kamata, E. Kanoh, T. Ohsaki, K. Yamada, Multi-Level Dynamics between Below-Gap States in Heavily Doped Quantum Wells by Time-Resolved and Selectively-Excited Photoluminescence, Mater. Sci. Forum. 117–118 (1993) 345–350. https://doi.org/10.4028/www.scientific.net/msf.117-118.345.

[57] D. Dagnelund, Y.Q. Huang, C.W. Tu, H. Yonezu, I.A. Buyanova, W.M. Chen, Dual-wavelength excited photoluminescence spectroscopy of deep-level hole traps in Ga(In)NP, J. Appl. Phys. 117 (2015) 015701. https://doi.org/10.1063/1.4905274.

[58] E. Kanoh, K. Hoshino, N. Kamata, K. Yamada, M. Nishioka, Y. Arakawa, Saturation of photoluminescence quenching under below-gap excitation in a GaAs/AlGaAs quantum well, J. Lumin. 63 (1995) 235–240. https://doi.org/10.1016/0022-2313(94)00084-P.

[59] K. Hoshino, H. Kimura, T. Uchida, N. Kamata, K. Yamada, M. Nishioka, Y. Arakawa, Distribution of below-gap states in undoped GaAs/AlGaAs quantum wells revealed by two-wavelength excited photoluminescence, J. Lumin. 79 (1998) 39–46. https://doi.org/10.1016/S0022-2313(98)00017-9.

[60] J.M. Zanardi Ocampo, N. Kamata, K. Hoshino, M. Hirasawa, K. Yamada, M. Nishioka, Y. Arakawa, Spectroscopic discrimination of non-radiative centers in quantum wells by two wavelength excited photoluminescence, J. Cryst. Growth. 210 (2000) 238–241. https://doi.org/10.1016/S0022-0248(99)00687-9.

[61] N. Kamata, K. Hoshino, H. Kimura, T. Uchida, K. Yamada, M. Nishioka, Y. Arakawa, Sensitive detection of below-gap states by two-wavelength excitation spectroscopy in single-photon-counting region, J. Lumin. 72–74 (1997) 797–798. https://doi.org/https://doi.org/10.1016/S0022-2313(97)00075-6.

[62] N. Kamata, K. Hoshino, T. Uchida, K. Yamada, M. Nishioka, Y. Arakawa, Up-conversion luminescence via a below-gap state in GaAs/AlGaAs quantum wells, Superlattices Microstruct. 22 (1997) 521–528. https://doi.org/10.1006/spmi.1996.0293.

[63] K. Hoshino, T. Uchida, N. Kamata, K. Yamada, M. Nishioka, Y. Arakawa, Below-gap spectroscopy of undoped GaAs/AlGaAs quantum wells by two-wavelength excited photoluminescence, Japanese J. Appl. Physics, Part 1 Regul. Pap. Short Notes Rev. Pap. 37 (1998) 3210–3213. https://doi.org/10.1143/jjap.37.3210.

[64] N. Kamata, J.M.Z. Ocampo, K. Hoshino, K. Yamada, M. Nishioka, T. Someya, Y. Arakawa, Below-gap spectroscopy of semiconductor quantum wells by two-wavelength excited photoluminescence (TRPL), Recent Res. Dev. Quantum Electron. 1 (1999) 123–135.

[65] K. Hoshino, J.M.Z. Ocampo, N. Kamata, K. Yamada, M. Nishioka, Y. Arakawa, Absence of nonradiative recombination centers in modulation-doped quantum wells revealed by two-wavelength excited photoluminescence, Phys. E Low-Dimensional Syst. Nanostructures. 7 (2000) 563–566. https://doi.org/10.1016/S1386-9477(99)00384-7.

[66] J.M. Zanardi Ocampo, N. Kamata, K. Hoshino, K. Endoh, K. Yamada, M. Nishioka, T. Someya, Y. Arakawa, Spectroscopy of non-radiative recombination centers in quantum wells by two-wavelength excited photoluminescence, J. Lumin. 87–89 (2000) 363–365. https://doi.org/https://doi.org/10.1016/S0022-2313(99)00394-4.

[67] I.J. Chen, T.T. Chen, Y.F. Chen, T.Y. Lin, Nonradiative traps in InGaN/GaN multiple quantum wells revealed by two wavelength excitation, Appl. Phys. Lett. 89 (2006) 142113. https://doi.org/10.1063/1.2360221.

[68] J.M. Zanardi Ocampo, N. Kamata, W. Okamoto, K. Yamada, K. Hoshino, T. Someya, Y. Arakawa, Extremely slow relaxation process of a yellow-luminescence-related state in GaN revealed by two-wavelength excited photoluminescence, Phys. Status Solidi Basic Res. 228 (2001) 433–436. https://doi.org/10.1002/1521-3951(200111)228:2<433::AID-PSSB433>3.0.CO;2-U.

[69] N. Kamata, J.M. Zanardi Ocampo, W. Okamoto, K. Hoshino, T. Someya, Y.

Arakawa, K. Yamada, Below-gap recombination dynamics in GaN revealed by time-resolved and two-wavelength excited photoluminescence, Mater. Sci. Eng. B Solid-State Mater. Adv. Technol. 91–92 (2002) 290–293. https://doi.org/10.1016/S0921-5107(01)01032-7.

[70] N. Kamata et al., Temperature dependence of photoluminescence intensity change due to below-gap excitation in GaN, in: Y. Arakawa et al. (Ed.), 28th Int. Symp. Compd. Semicond., Institute of Physics: Tokyo, 2001: pp. 843–848.

[71] J.M. Zanardi Ocampo, H. Klausing, O. Semchinova, J. Stemmer, M. Hirasawa, N. Kamata, K. Yamada, Study of MBE-grown GaN/AlGaN quantum well structures by two wavelength excited photoluminescence, Phys. Status Solidi Appl. Res. 183 (2001) 189–195. https://doi.org/10.1002/1521-396X(200101)183:1<189::AID-PSSA189>3.0.CO;2-5.

[72] H. Klausing, N. Kamata, F. Takahashi, F. Fedler, D. Mistele, J. Aderhold, O.K. Semchinova, J. Graul, T. Someya, Y. Arakawa, Improved quality of plasma assisted MBE-grown GaN/AlGaN quantum wells revealed by two-wavelength excited photoluminescence, Phys. Status Solidi Curr. Top. Solid State Phys. 0 (2003) 2658–2661. https://doi.org/10.1002/pssc.200303473.

[73] A.Z.M. Touhidul Islam, N. Murakoshi, T. Fukuda, H. Hirayama, N. Kamata, Optical detection of nonradiative recombination centers in AlGaN quantum wells for deep UV region, Phys. Status Solidi Curr. Top. Solid State Phys. 11 (2014) 832–835. https://doi.org/10.1002/pssc.201300405.

[74] N. Kamata, A.Z.M. Touhidul Islam, M. Julkarnain, N. Murakoshi, T. Fukuda, H. Hirayama, Nonradiative centers in deep-UV AlGaN-based quantum wells revealed by two-wavelength excited photoluminescence, Phys. Status Solidi Basic Res. 252 (2015) 936–939. https://doi.org/10.1002/pssb.201451582.

[75] A.Z.M.T. Islam, T. Hanaoka, K. Onabe, S. Yagi, N. Kamata, H. Yaguchi, Direct evidence of carrier excitation from intermediate band states in GaPN by two-wavelength excited photoluminescence, Appl. Phys. Express. 6 (2013) 092401. https://doi.org/10.7567/APEX.6.092401.

[76] T. Li, Y. Kotuska, T. Fukuda, T. Kurushima, N. Kamata, Nonradiative centers in Ba3Si6O12N2:Eu2+ phosphors observed by the below-gap excitation method, Mater. Lett. 145 (2015) 158–161. https://doi.org/10.1016/j.matlet.2015.01.054.

[77] T. Li, N. Kamata, Y. Kotsuka, T. Fukuda, Z. Honda, T. Kurushima, Trap and nonradiative centers in Ba_3Si_6O_12N_2:Eu^2+ phosphors observed by thermoluminescence and two-wavelength excited photoluminescence methods, Opt. Express. 23 (2015) 16511–16516. https://doi.org/10.1364/oe.23.016511.

[78] A. Zukauskas, M.S. Shue, R. Gaska, Introduction to Solid-state Lighting, Wiley, New York, 2002.

[79] H. Hirayama, Quaternary InAlGaN-based high-efficiency ultraviolet light-emitting diodes, J. Appl. Phys. 97 (2005) 091101. https://doi.org/10.1063/1.1899760.

[80] H. Hirayama, T. Yatabe, N. Noguchi, T. Ohashi, N. Kamata, 231-261 nm AlGaN deep-ultraviolet light-emitting diodes fabricated on AlN multilayer buffers grown by ammonia pulse-flow method on sapphire, Appl. Phys. Lett. 91 (2007) 071901. https://doi.org/10.1063/1.2770662.

[81] H. Hirayama, N. Noguchi, T. Yatabe, N. Kamata, 227 nm AlGaN light-emitting diode with 0.15 mW output power realized using a thin quantum well and AIN buffer with reduced threading dislocation density, Appl. Phys. Express. 1 (2008) 051101. https://doi.org/10.1143/APEX.1.051101.

[82] M.A. Khan, M. Shatalov, H.P. Maruska, H.M. Wang, E. Kuokstis, III-nitride UV devices, Japanese J. Appl. Physics, Part 1 Regul. Pap. Short Notes Rev. Pap. 44 (2005) 7191–7206. https://doi.org/10.1143/JJAP.44.7191.

[83] H. Hirayama, Y. Tsukada, T. Maeda, N. Kamata, Marked enhancement in the efficiency of deep-ultraviolet AlGaN light-emitting diodes by using a multiquantum-barrier electron blocking layer, Appl. Phys. Express. 3 (2010) 031002. https://doi.org/10.1143/APEX.3.031002.

[84] S. Fujikawa, H. Hirayama, N. Maeda, High-efficiency AlGaN deep-UV LEDs fabricated on a- and m-axis oriented c-plane sapphire substrates, Phys. Status Solidi Curr. Top. Solid State Phys. 9 (2012) 790–793. https://doi.org/10.1002/pssc.201100453.

[85] T. Mino, H. Hirayama, T. Takano, K. Tsubaki, M. Sugiyama, Realization of 256-278nm AlGaN-based deep-ultraviolet light-emitting diodes on si substrates using epitaxial lateral overgrowth AlN templates, Appl. Phys. Express. 4 (2011) 092104.

https://doi.org/10.1143/APEX.4.092104.

[86] M. Shatalov, W. Sun, A. Lunev, X. Hu, A. Dobrinsky, Y. Bilenko, J. Yang, M. Shur, R. Gaska, C. Moe, G. Garrett, M. Wraback, AlGaN deep-ultraviolet light-emitting diodes with external quantum efficiency above 10%, Appl. Phys. Express. 5 (2012) 082101. https://doi.org/10.1143/APEX.5.082101.

[87] H. Murotani, D. Akase, K. Anai, Y. Yamada, H. Miyake, K. Hiramatsu, Dependence of internal quantum efficiency on doping region and Si concentration in Al-rich AlGaN quantum wells, Appl. Phys. Lett. 101 (2012) 042110. https://doi.org/10.1063/1.4739431.

[88] T. Onuma, S.F. Chichibu, A. Uedono, T. Sota, P. Cantu, T.M. Katona, J.F. Keading, S. Keller, U.K. Mishra, S. Nakamura, S.P. DenBaars, Radiative and nonradiative processes in strain-free AlxGa 1-xN films studied by time-resolved photoluminescence and positron annihilation techniques, J. Appl. Phys. 95 (2004) 2495–2504. https://doi.org/10.1063/1.1644041.

[89] N. Nepal, M.L. Nakarmi, J. Lin, H.X. Jiang, Photoluminescence studies of impurity transitions in AlGaN alloys, Appl. Phys. Lett. 89 (2006) 092107. https://doi.org/10.1063/1.2337856.

[90] T.A. Henry, A. Armstrong, A.A. Allerman, M.H. Crawford, The influence of Al composition on point defect incorporation in AlGaN, Appl. Phys. Lett. 100 (2012) 043509. https://doi.org/10.1063/1.3679681.

[91] A.R. Arehart, A.A. Allerman, S.A. Ringel, Electrical characterization of n-type Al0.30Ga0.70N Schottky diodes, J. Appl. Phys. 109 (2011) 114506. https://doi.org/10.1063/1.3592284.

[92] A. Armstrong, A.A. Allerman, T.A. Henry, M.H. Crawford, Influence of growth temperature on AlGaN multiquantum well point defect incorporation and photoluminescence efficiency, Appl. Phys. Lett. 98 (2011) 162110. https://doi.org/10.1063/1.3583448.

[93] N. Kamata, S. Saravanan, J.M. Zanardi Ocampo, P.O. Vaccaro, Y. Arakawa, Nonradiative centers in InAs quantum dots revealed by two-wavelength excited photoluminescence, Phys. B Condens. Matter. 376–377 (2006) 849–852. https://doi.org/10.1016/j.physb.2005.12.211.

[94] A. Polimeni, A. Patanè, M. Henini, L. Eaves, P.C. Main, Temperature dependence of the optical properties of (formula presented) self-organized quantum dots, Phys. Rev. B - Condens. Matter Mater. Phys. 59 (1999) 5064–5068. https://doi.org/10.1103/PhysRevB.59.5064.

[95] J. Ma, X. Ji, G. Wang, X. Wei, H. Lu, X. Yi, R. Duan, J. Wang, Y. Zeng, J. Li, F. Yang, C. Wang, G. Zou, Anomalous temperature dependence of photoluminescence in self-assembled InGaN quantum dots, Appl. Phys. Lett. 101 (2012) 131101. https://doi.org/10.1063/1.4754533.

[96] T. Lu, Z. Ma, C. Du, Y. Fang, H. Wu, Y. Jiang, L. Wang, L. Dai, H. Jia, W. Liu, H. Chen, Temperature-dependent photoluminescence in light-emitting diodes, Sci. Rep. 4 (2014) 6131. https://doi.org/10.1038/srep06131.

[97] X.H. Zheng, H. Chen, Z.B. Yan, D.S. Li, H.B. Yu, Q. Huang, J.M. Zhou, Influence of the deposition time of barrier layers on optical and structural properties of high-efficiency green-light-emitting InGaN/GaN multiple quantum wells, J. Appl. Phys. 96 (2004) 1899–1903. https://doi.org/10.1063/1.1769099.

[98] D. Bimberg, M. Sondergeld, E. Grobe, Thermal dissociation of excitons bounds to neutral acceptors in high-purity GaAs, Phys. Rev. B. 4 (1971) 3451–3455. https://doi.org/10.1103/PhysRevB.4.3451.

[99] M. Hao, J. Zhang, X.H. Zhang, S. Chua, Photoluminescence studies on InGaN/GaN multiple quantum wells with different degree of localization, Appl. Phys. Lett. 81 (2002) 5129–5131. https://doi.org/10.1063/1.1531837.

[100] Z. Deng, Y. Jiang, Z. Ma, W. Wang, H. Jia, J. Zhou, H. Chen, A novel wavelength-adjusting method in InGaN-based light-emitting diodes, Sci. Rep. 3 (2013) 3389. https://doi.org/10.1038/srep03389.

[101] M. Tajima, Fatigue and Recovery Effects of the 0.65-eV Emission Band in GaAs, Jpn. J. Appl. Phys. 23 (1984) L690–L693. https://doi.org/10.1143/JJAP.23.L690.

[102] M. Julkarnain, T. Fukuda, N. Kamata, Y. Arakawa, A direct evidence of allocating yellow luminescence band in undoped GaN by two-wavelength excited photoluminescence, Appl. Phys. Lett. 107 (2015) 212102. https://doi.org/10.1063/1.4936243.

[103] M.D. Haque, M. Julkarnain, A.Z.M.T. Islam, N. Kamata, Study of Nonradiative

Recombination Centers in n-GaN Grown on LT-GaN and AlN Buffer Layer by Below-Gap Excitation, Adv. Mater. Phys. Chem. 08 (2018) 143–155. https://doi.org/10.4236/ampc.2018.83010.

[104] Q. Dai, M.F. Schubert, M.H. Kim, J.K. Kim, E.F. Schubert, D.D. Koleske, M.H. Crawford, S.R. Lee, A.J. Fischer, G. Thaler, M.A. Banas, Internal quantum efficiency and nonradiative recombination coefficient of GaInN/GaN multiple quantum wells with different dislocation densities, Appl. Phys. Lett. 94 (2009) 111109. https://doi.org/10.1063/1.3100773.

[105] Y.-S. Yoo, T.-M. Roh, J.-H. Na, S.J. Son, Y.-H. Cho, Simple analysis method for determining internal quantum efficiency and relative recombination ratios in light emitting diodes, Appl. Phys. Lett. 102 (2013) 211107. https://doi.org/10.1063/1.4807485.

[106] X. Li, S. Sundaram, P. Disseix, G. Le Gac, S. Bouchoule, G. Patriarche, F. Réveret, J. Leymarie, Y. El Gmili, T. Moudakir, F. Genty, J.-P. Salvestrini, R.D. Dupuis, P.L. Voss, A. Ougazzaden, AlGaN-based MQWs grown on a thick relaxed AlGaN buffer on AlN templates emitting at 285 nm, Opt. Mater. Express. 5 (2015) 380. https://doi.org/10.1364/ome.5.000380.

[107] J. Piprek, Efficiency droop in nitride-based light-emitting diodes, Phys. Status Solidi Appl. Mater. Sci. 207 (2010) 2217–2225. https://doi.org/10.1002/pssa.201026149.

[108] M. Meneghini, N. Trivellin, G. Meneghesso, E. Zanoni, U. Zehnder, B. Hahn, A combined electro-optical method for the determination of the recombination parameters in InGaN-based light-emitting diodes, J. Appl. Phys. 106 (2009) 114508. https://doi.org/10.1063/1.3266014.

[109] Y.C. Shen, G.O. Mueller, S. Watanabe, N.F. Gardner, A. Munkholm, M.R. Krames, Auger recombination in InGaN measured by photoluminescence, Appl. Phys. Lett. 91 (2007) 141101. https://doi.org/10.1063/1.2785135.

[110] C. De Santi, M. Meneghini, D. Monti, J. Glaab, M. Guttmann, J. Rass, S. Einfeldt, F. Mehnke, J. Enslin, T. Wernicke, M. Kneissl, G. Meneghesso, E. Zanoni, Recombination mechanisms and thermal droop in AlGaN-based UV-B LEDs, Photonics Res. 5 (2017) A44. https://doi.org/10.1364/prj.5.000a44.

[111] J. Glaab, C. Ploch, R. Kelz, C. Stölmacker, M. Lapeyrade, N.L. Ploch, J. Rass, T. Kolbe, S. Einfeldt, F. Mehnke, C. Kuhn, T. Wernicke, M. Weyers, M. Kneissl, Degradation of (InAlGa)N-based UV-B light emitting diodes stressed by current and temperature, J. Appl. Phys. 118 (2015) 094504. https://doi.org/10.1063/1.4929656.

[112] C. De Santi, M. Meneghini, M. La Grassa, B. Galler, R. Zeisel, M. Goano, S. Dominici, M. Mandurrino, F. Bertazzi, D. Robidas, G. Meneghesso, E. Zanoni, Role of defects in the thermal droop of InGaN-based light emitting diodes, J. Appl. Phys. 119 (2016) 094501. https://doi.org/10.1063/1.4942438.

[113] N.L. Ploch, S. Einfeldt, M. Frentrup, J. Rass, T. Wernicke, A. Knauer, V. Kueller, M. Weyers, M. Kneissl, Investigation of the temperature dependent efficiency droop in UV LEDs, Semicond. Sci. Technol. 28 (2013) 125021. https://doi.org/10.1088/0268-1242/28/12/125021.

[114] M.A. Khan, N. Maeda, M. Jo, Y. Akamatsu, R. Tanabe, Y. Yamada, H. Hirayama, 13 mW operation of a 295-310 nm AlGaN UV-B LED with a p-AlGaN transparent contact layer for real world applications, J. Mater. Chem. C. 7 (2019) 143–152. https://doi.org/10.1039/C8TC03825B.

[115] T. Matsumoto, M. Ajmal Khan, N. Maeda, S. Fujikawa, N. Kamata, H. Hirayama, Milliwatt power UV-A LEDs developed by using n-AlGaN superlattice buffer layers grown on AlN templates, J. Phys. D. Appl. Phys. 52 (2019) 115102. https://doi.org/10.1088/1361-6463/aaf60a.

[116] A. Pinos, S. Marcinkevičius, J. Yang, Y. Bilenko, M. Shatalov, R. Gaska, M.S. Shur, Aging of AlGaN quantum well light emitting diode studied by scanning near-field optical spectroscopy, Appl. Phys. Lett. 95 (2009) 181914. https://doi.org/10.1063/1.3262964.

[117] A. Pinos, S. Marcinkevičius, J. Yang, R. Gaska, M. Shatalov, M.S. Shur, Optical studies of degradation of AlGaN quantum well based deep ultraviolet light emitting diodes, J. Appl. Phys. 108 (2010) 093113. https://doi.org/10.1063/1.3506697.

[118] A. Pinos, S. Marcinkevičius, M.S. Shur, High current-induced degradation of AlGaN ultraviolet light emitting diodes, in: J. Appl. Phys., 2011: p. 103108. https://doi.org/10.1063/1.3590149.

[119] A. Yasan, R. McClintock, K. Mayes, D.H. Kim, P. Kung, M. Razeghi, Photoluminescence study of AlGaN-based 280 nm ultraviolet light-emitting diodes, Appl. Phys. Lett. 83 (2003) 4083–4085. https://doi.org/10.1063/1.1626808.

[120] M.I. Hossain, Y. Itokazu, S. Kuwaba, N. Kamata, N. Maeda, H. Hirayama, Nonradiative recombination centers in deep uv-wavelength algan quantum wells detected by below-gap excitation light, Jpn. J. Appl. Phys. 58 (2019) SCCB37. https://doi.org/10.7567/1347-4065/ab1069.

[121] S.M. Sze, K.K. Ng, Physics of Semiconductor Devices, Third Edit, Wiley Interscience, 2006.

[122] H. Lui, R.R. Anderson, Radiation Sources and Interaction with Skin, in: Photodermatology, 2007: pp. 29–40.

[123] E. Becatti, K. Petroni, D. Giuntini, A. Castagna, V. Calvenzani, G. Serra, A. Mensuali-Sodi, C. Tonelli, A. Ranieri, Solar UV-B radiation influences carotenoid accumulation of tomato fruit through both ethylene-dependent and independent mechanisms, J. Agric. Food Chem. 57 (2009) 10979–10989. https://doi.org/10.1021/jf902555x.

[124] S. Neugart, M. Zietz, M. Schreiner, S. Rohn, L.W. Kroh, A. Krumbein, Structurally different flavonol glycosides and hydroxycinnamic acid derivatives respond differently to moderate UV-B radiation exposure, Physiol. Plant. 145 (2012) 582–593. https://doi.org/10.1111/j.1399-3054.2012.01567.x.

[125] Y.H. Cho, G.H. Gainer, A.J. Fischer, J.J. Song, S. Keller, U.K. Mishra, S.P. DenBaars, "S-shaped" temperature-dependent emission shift and carrier dynamics in InGaN/GaN multiple quantum wells, Appl. Phys. Lett. 73 (1998) 1370–1372. https://doi.org/10.1063/1.122164.

[126] H.P.D. Schenk, P. De Mierry, F. Omnès, P. Gibart, Spectroscopic studies of InGaN ternary alloys, Phys. Status Solidi Appl. Res. 176 (1999) 307–311. https://doi.org/10.1002/(SICI)1521-396X(199911)176:1<307::AID-PSSA307>3.0.CO;2-U.

[127] J. Li, K.B. Nam, J.Y. Lin, H.X. Jiang, Optical and electrical properties of Al-rich AlGaN alloys, Appl. Phys. Lett. 79 (2001) 3245–3247. https://doi.org/10.1063/1.1418255.

[128] Y.H. Cho, G. Gainer, J. Lam, J. Song, W. Yang, Dynamics of anomalous optical transitions in alloys, Phys. Rev. B - Condens. Matter Mater. Phys. 61 (2000) 7203–7206. https://doi.org/10.1103/PhysRevB.61.7203.

[129] A. Kaschner, T. Lüttgert, H. Born, A. Hoffmann, A.Y. Egorov, H. Riechert, Recombination mechanisms in GaInNAs/GaAs multiple quantum wells, Appl. Phys. Lett. 78 (2001) 1391–1393. https://doi.org/10.1063/1.1355014.

[130] K. Yamashita, T. Kita, H. Nakayama, T. Nishino, Photoluminescence from metastable states in long-range ordered (Al0.5Ga0.5)0.51In0.49P Kenichi, Phys. Rev. B. 55 (1997) 4411–4416.

[131] Y.-H. Cho, B.D. Little, G.H. Gaine, J.J. Song, S. Keller, U.K. Mishra, S.P. DenBaars, CARRIER DYNAMICS OF ABNORMAL TEMPERATURE-DEPENDENT EMISSION SHIFT IN MOCVD-GROWN InGaN EPILAYERS AND InGaN/GaN QUANTUM WELLS, MRS Internet J. Nitride Semicond. Res. 4S1 (1999) G2.4. https://doi.org/10.1017/CBO9781107415324.004.

[132] H. Wang, Z. Ji, S. Qu, G. Wang, Y. Jiang, B. Liu, X. Xu, H. Mino, Influence of excitation power and temperature on photoluminescence in InGaN/GaN multiple quantum wells, Opt. Express. 20 (2012) 3932–3940. https://doi.org/10.1088/1674-1056/24/2/024219.

[133] J. Ma, X. Ji, G. Wang, X. Wei, H. Lu, X. Yi, R. Duan, J. Wang, Y. Zeng, J. Li, F. Yang, C. Wang, G. Zou, Anomalous temperature dependence of photoluminescence in self-assembled InGaN quantum dots, Appl. Phys. Lett. 101 (2012) 131101. https://doi.org/10.1063/1.4754533.

[134] M. Julkarnain, N. Murakoshi, A.Z.M.T. Islam, T. Fukuda, N. Kamata, Y. Arakawa, Dominant nonradiative centers in InGaN single quantum well by time-resolved and two-wavelength excited photoluminescence, Phys. Status Solidi Basic Res. 252 (2015) 952–955. https://doi.org/10.1002/pssb.201451499.

---------- o ----------